# Concertos of planet-disk interactions: thermal and kinematic fingerprints

## Kan Chen

A dissertation submitted in partial fulfillment of the requirements for the degree of

**Doctor of Philosophy** 

of

**University College London.** 

Department of Physics and Astronomy
University College London

July 31, 2025

I, Kan Chen, confirm that the work presented in this thesis is my own. Where information has been derived from other sources, I confirm that this has been indicated in the work.

# **Abstract**

Planets form in protoplanetary disks, where interactions with their natal environments shape disk evolution and leave observable signatures. High-resolution observations over the past decade have revealed substructures such as gaps, rings, and non-Keplerian motions, often linked to forming planets. My research explores planet-disk interactions and thermal and kinematic imprints on disks.

We develop a novel iterative modeling framework combining 2D hydrodynamical and 3D radiative transfer simulations to study how gap-opening by giant planets alters disk thermal structures. Our results show that such planets carve deep gaps and significantly heat the surrounding regions by several tens of Kelvin. This temperature rise shifts volatile ice lines outward and can create multiple ice lines for a single species, influencing disk chemistry (e.g., the C/O ratio) and subsequent planet composition.

Incorporating multiple dust species into our iterative models, we find temperature deviations similar to the gas-only cases. Dust rings created by pressure bumps can cool by several Kelvin, forming localized freeze-out zones, although overall ice distributions remain largely unchanged. We also explore how varying the  $\alpha$  viscosity affects ice line locations and find no simple one-to-one relationship in structured disks.

While recent observations have detected non-Keplerian gas motions, their origins remain debated. We study planet-induced kinematic signatures using 3D simulations and synthetic channel maps. Our results show that hydrodynamical simulations need to run for  $\sim 1000$  orbits to reach steady state and that high resolution ( $\geq 14$  cells per scale height) is necessary to capture spiral features accurately, a

Abstract 4

requirement that most previous Smoothed-particle hydrodynamics (SPH) or grid-based simulations do not satisfy.

Our studies offer new insights into how planets shape disk structure, composition, and kinematics, enhancing our understanding of planet formation. These results also inform future observations with ALMA, NgVLA, JWST, and Ariel.

# **Impact Statement**

My research during my PhD focuses on using hydrodynamic and radiative transfer simulations to study protoplanetary disks and planet-disk interactions. The goal of my work is to investigate where and how planets form, as well as how they influence the evolution of protoplanetary disks and exoplanetary atmospheres. My research contribution during my PhD leads to 3 first-author papers.

#### **Research Declaration**

This thesis contains chapters which are based on the following publications:

- 1. Chapter 2 is based on the published paper **Chen, K.**, Kama, M., Pinilla, P., & Keyte, L. (2024). 'Planet Gap-opening Feedback on Disk Thermal Structure and Composition'. Monthly Notices of the Royal Astronomical Society, 527, 2049. A digital copy of the published article is available at https://academic.oup.com/mnras/article/527/2/2049/7330168. K.Chen ran simulations, analysed results and wrote the manuscript. M.K. contributed to the Section 2.4.1. P.P contributed to the Section 2.4.2. L.K. contributed to the Section 2.4.4. All co-authors contributed feedback on the manuscript.
- 2. Chapter 3 is based on the paper Chen, K., Pinilla, P., & Kama, M. (2025). 'Planet-induced Gas and Dust Substructure Feedbacks on Disk Thermal Structure'. Monthly Notices of the Royal Astronomical Society, 541, 2830. A digital copy of the published article is available at https://academic.oup.com/mnras/article/541/4/2830/8199927. K.Chen ran simulation, analysed results and wrote the manuscript. M.K. contributed to the Section 3.4.3. All co-authors contributed feedback on the manuscript.
- 3. Chapter 4 is based on the paper **Chen, K.**, & Dong, R. (2024). 'Mind the kinematics simulation of planet-disk interactions: time evolution and numerical resolution'. The Astrophysical Journal, 976, 49. A digital copy of the published article is available at https://iopscience.iop.org/article/10.3847/1538-4357/ad83d0. K.Chen ran simulations, analysed results and wrote the manuscript. R.D. contributed feedback on the manuscript.

# Acknowledgements

I would like to express my deepest gratitude to my supervisors, Mihkel Kama and Paola Pinilla, for their invaluable guidance, encouragement, and support throughout my PhD. Paola's clear thinking and deep curiosity always challenged me to improve, and her careful, critical feedback helped sharpen my ideas. Mihkel's positivity, encouragement, and strong intuition gave me both confidence and direction in my research. Their mentorship shaped not only this thesis but also the way I approach problems, think about science, and work as part of a research community. I feel truly fortunate to have learned from both of them.

I'm deeply thankful to Ruobing Dong, a fantastic collaborator who made the projects we worked on smoother, more insightful, and more enjoyable. His timely feedback and generous support were crucial during key stages of my research. I also want to thank Min-Kai Lin, my undergraduate summer project supervisor at ASIAA, who introduced me to the field of protoplanetary disks. His guidance and trust gave me the foundation and motivation to pursue astrophysical research seriously.

Thanks to Luke for his invaluable suggestions about both life and academics. I have met him even more often than my supervisors throughout this journey. I also want to thank other colleagues, Anibal, Jeremy, Michael, and Dirk, for their insightful scientific discussions and generous help with postdoc applications. Finally, thanks to other students in the group, including Anna, Jason, Juanita, and Lilian, for science discussions throughout the PhD journey.

Special thanks to Qianqian and Jocelyn for their companionship and encouragement through the ups and downs of my PhD journey. And to Duoduo, a gentle,

versatile little dog whose presence brought me quiet emotional support during the early years of my PhD. He lives on in spirit and even in name in one of the Python modules I developed. I hope he is happy and healthy, wherever he is.

To my parents, who may not understand physics, coding, or astronomy but saw that I was doing something I love, thank them for their quiet support. When I first told them I wanted to study astronomy, they were worried I might spend my life on some mountaintop staring at stars. But in the end, they let me follow my passion even though the path was unfamiliar. I'm deeply grateful for their trust and encouragement.

Finally, I want to thank myself for never forgetting what I love and always striving toward my dream. Back in the final year of secondary school, listening to Beethoven's Piano Concerto No. 5 "Emperor" before major exams became a sacred ritual that gave me strength. That memory didn't just inspire me at the time, it stayed with me and ultimately became the creative spark for this thesis, Concertos of Planet-Disk Interactions: Thermal and Kinematic Fingerprints.

# **Contents**

	Impa	act State	ement	5
	Rese	earch De	eclaration	6
1	Intr	oductio	n	26
	1.1	Histor	y of concertos: protoplanetary disk formation	27
	1.2	Disk o	bservations	29
		1.2.1	Optical and near-infrared observations	29
		1.2.2	Dust continuum and gas observation	30
		1.2.3	Observation of Substructures	32
		1.2.4	Substructure formation without planets	35
	1.3	The O	rchestra: structure of disks	36
		1.3.1	Governing equations	36
		1.3.2	Disk density	40
		1.3.3	Disk velocity	42
		1.3.4	Disk temperature	43
		1.3.5	Iceline and disk composition	45
	1.4	Disk e	volution	45
		1.4.1	Disk viscosity	47
		1.4.2	MHD winds	49
		1.4.3	Disk size and mass	49
	1.5	The Co	oncertos: Planet-disk interactions	51
		1.5.1	Gap opening by planets	51
		1.5.2	Spirals excited by planets	
		1.5.3	Kinematic planetary signatures	54
			1 , 0	

10
ĺ

	1.6	The so	ploist and conductor: Protoplanets and stars	57
		1.6.1	Protoplanets	57
		1.6.2	Star-disk interactions	59
	1.7	Outlin	e of this thesis	59
2	Plan	iet Gap	-opening Feedback on Disk Thermal Structure and Compo-	
	sitio	n		62
	2.1	Introd	uction	64
	2.2	Metho	ods	66
		2.2.1	Hydrodynamical simulations	67
		2.2.2	Radiative transfer simulations	68
		2.2.3	Workflow	70
	2.3	Result	S	72
		2.3.1	Gas surface density	72
		2.3.2	Midplane temperature	75
		2.3.3	Eccentricity	78
		2.3.4	Dust trap	80
		2.3.5	Distribution of ice species	83
	2.4	Discus	ssion	86
		2.4.1	The C/O ratio as a planet formation tracer	86
		2.4.2	Ice lines and dust rings	89
		2.4.3	Inner rim midplane temperature drops	90
		2.4.4	Assumptions and limitations	91
	2.5	Conclu	usions	93
	2.6	Appen	ndix	95
		2.6.1	Tests of iteration steps	95
		2.6.2	Comparisons between midplane temperature and density-	
			weighted vertical averaged temperature	96
		2.6.3	Gas density of planets at 10au and 30au	96
		2.6.4	Temperature of planets at 10au and 30au	98

Contents 11

3	Plar	net-indu	iced Gas and Dust Substructure Feedbacks on Disk Therma	al
	Stru	cture		99
	3.1	Introd	uction	. 101
	3.2	Metho	ods	. 103
		3.2.1	Hydrodynamical setups	. 104
		3.2.2	Monte Carlo Radiative Transfer setup	. 106
		3.2.3	Post possessing between radiative transfer and hydro	. 106
	3.3	Result	·s	. 107
		3.3.1	Effects of dust	. 108
		3.3.2	Effects of different viscosity	. 115
	3.4	Discus	ssion	. 119
		3.4.1	Rings/gaps in hydro simulations vs molecule line observation	ns 119
		3.4.2	Observability of planet impact on disk temperature and ice-	
			lines	. 120
		3.4.3	"Flickering" icelines	. 121
		3.4.4	Limits of our model	. 122
	3.5	Conclu	usions	. 123
4	Min	d the ki	inematics simulation of planet-disk interactions: time evolu	<b>u</b> -
	tion	and nu	merical resolution	125
	4.1	Introd	uction	. 127
	4.2	Hydro	dynamic simulation setup	. 128
	4.3	Planet	-induced perturbations in velocities	. 129
		4.3.1	Temporal variations in planet-induced velocity perturbations	s 130
		4.3.2	Numerical convergence tests	. 136
	4.4	Signat	cures in synthetic CO observations	. 138
		4.4.1	Synthetic observation generation	. 139
		4.4.2	Effect of simulation time	. 143
		4.4.3	Effects of numerical resolution	
	4.5	conclu	usions	. 143
	4.6		ndix	

Bi	bliography		152
5	Conclusions		150
	4.6.4	Channel maps	148
	4.6.3	Azimuthal average background versus Keplerian background	147
	4.6.2	Local variabilities in $V_{\phi}-V_{\mathrm{Kep}}$ and $V_{\theta}$ on orbital timescale .	146
	4.6.1	$\tau=1$ surface	146

# **List of Figures**

1.1	Schematic diagram illustrating the evolutionary sequence from a	
	prestellar core to the formation of a planetary system, shown in	
	panels (a)–(d). The spectral energy distribution (SED) features cor-	
	responding to Class 0, I, II, and III sources are depicted in the lower	
	panels. The figure is adapted from Pineda et al. (2023); Keyte (2024).	28
1.2	Scattered light images of protoplanetary disks. From left to right:	
	the Orion proplyd observed by the Hubble Space Telescope (HST),	
	HH 30 by the James Webb Space Telescope (JWST), and IM Lup	
	by VLT/SPHERE. Image credits: (a) Mark McCaughrean (Max	
	Planck Institute for Astronomy), C. Robert O'Dell (Rice Univer-	
	sity), and NASA/ESA; (b) ESA/Webb, NASA & CSA, Tazaki et	
	al.; (c) ESO/H. Avenhaus et al., DARTT-S collaboration	30
1.3	Gallery of DSHARP and MAPS disk images. Five disks that are	
	included in both the DSHARP and MAPS samples are shown to	
	illustrate how dust continuum and chemical substructures (CO and	
	<sup>13</sup> CO), such as gaps and rings, differ in the same disks	31
1.4	Illustration of rings, crescents, and spirals in disks. The grey color	
	represents dust continuum emission, while the red color indicates	
	near-infrared (NIR) emission. The figure is adapted from Bae et al.	
	(2022)	33

1.5	Panel (a) shows the channel maps of gas molecular line observations.  Panel (a) shows the channel maps of the CO line in a disk. Panel (b) shows the line profiles at three given spatial positions. Panel (c) shows a channel map of the CO line at a given velocity channel.  Panel (d) shows the spatially integrated line profile. Panel (e) shows the moment 1 map, which is the velocity map. Panel (f) shows the zeroth moment map, which is the integrated intensity map. The	25
	figure is adapted from Pinte et al. (2022)	37
1.6	Schematic diagram of the structure of a protoplanetary disk. The figure is adapted from Miotello et al. (2022)	38
1.7	Illustration of the radial and vertical coordinates of a disk with the star's gravity.	40
1.8	Schematic diagram of icelines in disks (upper) and the corresponding Carbon to Oxygen (C/O) ratio (lower). The figure is adapted from Cleeves et al. (2020).	46
1.9	Panel (a) shows a schematic diagram of two disk evolution models: the viscous disk model (lower) and the magnetic winds model (upper). Panels (b) and (c) show the time evolution of the disk gas surface density in the viscous disk model and the MHD wind model, respectively. The figure is adapted from Trapman et al. (2021); Manara et al. (2022)	46

1.10	Schematic diagram of velocity kinks. Panel (a) shows how the emis-	
	sion feature (white dotted lines) deviates from the Keplerian isove-	
	locity contours (white dashed line). Panel (b) displays the velocity	
	kink in a channel map at a channel velocity of 6.8 km/s. The green	
	circle highlights the kink. In panel (c), at another velocity channel,	
	no kink is detected. In both panel (b) and (c), the orange dot marks	
	the location of the planet in the midplane. The white dashed line	
	represents the planet's orbit in the midplane, while the white dotted	
	line indicates the projected orbit on the emission surface. Panel (a)	
	is a close-up of panel (b). The figure is adapted from Pinte et al.	
	(2018, 2022)	55
1.11	Diagram of planet mass and semi-major axis of confirmed exoplan-	
	ets and embedded protoplanets. The properties of protoplanets are	
	inferred from gaps, spirals, or kinematic planetary signatures (KPS)	
	or confirmed by direct imaging. This diagram is from Bae et al.	
	(2022)	60
2.1	The workflow of the iteration method. The green, blue, and yel-	
	low boxes represent the steps of FARGO3D, RADMC3D, and post-	
	processing between RADMC3D and FARGO3D, respectively. The	
	iteration step is 100 planet orbits	67
2.2	2D gas density map of planets at fixed radius of 4 au over 2000	
	orbits of iteration method (upper panels) and non-iteration method	
	(lower panels). From left to right columns, gaps are opened by	
	planets of $3M_{\rm J}$ , $1M_{\rm J}$ , $100M_{\oplus}$ , and $10M_{\oplus}$ , respectively	73
2.3	Normalized gap widths $\Delta_{\rm gap}/r_{\rm p}$ (green) and depths $\Sigma_{\rm gap}/\Sigma_0$ (blue)	
	and their uncertainties (error bars) as a function of $M_p$ at $r_p$ =	
	4 (panel (a)), 10 (panel (b)), and 30 au (panel (c)), respectively.	
	Dashed and solid lines represent the iteration and non-iteration re-	
	sults	74

2.4	Midplane temperature $T_{mid}$ as a function of disk radius from	
	RADMC3D simulations of planets at 4 au over 2000 orbits of	
	iteration method (upper panels) and non-iteration method (lower	
	panels). The cyan solid lines represent the azimuthal averaged $T_{mid}$ ,	
	while the shading areas represent the deviation of the profiles along	
	different azimuthal angles. From left to right, there are results	
	of $3M_{\rm J}$ , $1M_{\rm J}$ , $100M_{\oplus}$ , and $10M_{\oplus}$ , respectively. The blue, green,	
	and red dash-dotted lines near the horizontal direction represent	
	the pressure-dependent sublimation temperature $T_{evap,H_2O}$ $T_{evap,CO_2}$ ,	
	and $T_{evap,CO}$ , respectively. $T_{evap,CO}$ is shading with a light red re-	
	gion to highlight the wide range of possible values calculated from	
	different binding energies given by KIDA. As a comparison, con-	
	stant $T_{\text{sub}}$ in Öberg et al. (2011) are marked with short arrows in	
	these three colors on the right edge of each panel. The vertical cyan	
	dashed lines and grey dotted lines mark the location of the planets	
	and pressure maximum/dust trapping	76
2.5	Similar to Figure 2.4 (a) but $T_{\text{sub}}$ is calculated by using molecule	
	binding energy in Öberg et al. (2011)	78
2.6	Disk eccentricity calculated from Equation 2.2 for an example of	
2.0	$3M_{\rm J}$ at 4au of iteration method. Planet location is marked with a	
	vertical blue dashed line. The gap inner and outer edges are marked	
	by red dashed lines	79
	by fed dustice files.	1)
2.7	Normalized dust trapping location as a function of planet mass $M_p$ .	
	The iteration and non-iteration are marked with dashed and solid	
	lines and different $r_p = 4$ , 10, and 30 au are in red, green, and blue,	
	respectively	82

2.8	Ice distribution in disks with different $M_p$ and $r_p$ . The iteration and	
	non-iteration results are shown in the left and right panels, respec-	
	tively. High to low $M_p$ are listed from top to bottom panels. In each	
	panel, for instance, $3M_{\rm J}$ of iteration method, there are three groups	
	of data representing the cases of planets at 4 (bottom), 10 (middle),	
	and 30 au (top), respectively. The location of H <sub>2</sub> O, CO <sub>2</sub> , and CO	
	ice is in blue, green, and red bars. Vertical cyan dashed lines mark	
	$r_{\rm p}$ and grey dashed lines display the corresponding dust-trap loca-	
	tion. Note that in some cases there is no grey-dashed line because	
	there is not dust trapping.	85
2.9	C/O ratio as a function of location in a disk, for different masses of	
	a gap-opening planet at 4 au. From the upper middle to lower right	
	panels, we show a planet mass of $3M_{\rm J}$ , $1M_{\rm J}$ , $100M_{\oplus}$ , and $10M_{\oplus}$ at	
	4au using the iteration method, and a disk without planets (upper	
	left panel) for comparison. The blue and red solid lines show gas-	
	and solid-phase C/O ratios, whereas the solar C/O ratio is marked	
	by a green dashed line. The gap regions are shaded. The planet	
	location and dust trap location are marked as vertical cyan and grey	
	lines	87
2.10	Comparison of midplane temperature over 2000 orbits by using dif-	
	ferent iteration steps. The y-axes $\Delta T/T_{\rm it100}$ show the normalized	
	temperature difference between two iteration steps. $T_{\rm it50}$ , $T_{\rm it100}$ , or	
	$T_{\rm it500}$ is the temperature by adopting iteration steps of 50, 100, or	
	500 orbits, respectively	95
2.11	Comparison of midplane temperature and the density-weighted ver-	
	tical averaged temperature from RADMC3D simulations of $3M_{\rm J}$ at	
	4au over 100 orbits	96
2.12	Similar to Figure 2.2 bur for planets at 10 au	97
2.13	Similar to Figure 2.2 bur for planets at 30 au	97
2.14	Similar to Figure 2.4 but for planets at 10 au	98

shaded radius regions correspond to the mm dust ring regions in the

3.6	Miplane (solid) and sublimation (dashed) temperature profiles of
	different $M_p$ at $r_p = 30$ au of Model D
3.7	Comparions of radial ice distribution of H <sub>2</sub> O, CO <sub>2</sub> and CO obtained
	from Model G (left) and Model D (right). We show different $M_p$ ,
	$3M_{\rm J}$ , $100M_{\oplus}$ and $10M_{\oplus}$ from top to bottom. In each panel, from top
	to bottom, $r_p$ is 4, 10, and 30 au, respectively. Each bar represents
	ice existance regions in the midplane. Vertical cyan dashed lines
	represent the planet location
3.8	Radial midplane temperature (solid lines) and sublimation tem-
	perature (dashed lines) of Model D in non-planet disks with $\alpha =$
	$10^{-2}$ , $10^{-3}$ and $10^{-4}$ , respectively
3.9	Similar to Fig. 3.4, but for a planet-free disk setup with different
	viscosities in Model D. From upper left to bottom right, $\alpha = 10^{-2}$ ,
	$10^{-3}$ and $10^{-4}$
3.10	Ice plot with no planets in disks with different viscosities
3.11	The surface density of gas, 0.1 $\mu m$ and 1mm dust (left to right) as
	a function of disk radius of $100M_{\oplus}$ at 10au at different viscosities.
	The surface density is normalized by the initial value
3.12	Iceline locations obtained from models with $M_p=100M_\oplus$ and vis-
	cosity of $\alpha=10^{-2}$ (bottom), $10^{-3}$ (middle) and $\alpha=10^{-4}$ (top).
	The vertical cyan lines mark $r_p$
4.1	Surface density at 100 (upper) and 1,000 orbits (middle), and
	the corresponding azimuthal average (excluding azimuth within
	$\arcsin(3R_{\rm H}/r_{\rm p})$ to the planet) surface density profiles (lower).
	Cyan lines mark gap edges of $r_{\rm p} \pm 2R_{\rm H}$ ( $r_{\rm p} = 100$ au and $R_{\rm H} \sim 9.4$
	au) in all panels. The surface density peak along the primary inner
	and outer spirals is traced out by green open circles

4.2	$v_r$ at $2n$ from the initipliane in a simulation with a planet mass
	of $5M_{\rm th}$ and a numerical resolution of CPH= 20 at 100 (left) and
	100.35 (middle) planetary orbits. The right panel shows the mid-
	plane density. The planet location is marked with a cyan dot in the
	first two panels. The dashed circle marks a region in between pri-
	mary and secondary spiral arms in the inner disk. Colorbars are in
	units of m/s and planetary Keplerian velocity $V_{\rm p,Kep}$ . See §4.3.1.1
	and §4.3.1.2 for discussions
4.3	Short term variations in $V_r$ within 5 orbits at 5 locations at $2h$ above
	the midplane from point a to e in the disk and at $t_0 = 100$ , 300, and
	1,000 orbits. The locations of points a, b, c, d, and e are shown in
	the midplane density map at 1,000 orbits in the lower right panel.
	See §4.3.1.1 for details
4.4	2D standard deviation map of $V_r$ at 100, 300 and 1,000 orbits (left
	to right). The standard deviations are obtained within 5 orbits (see
	details in §4.3.1.1)
4.5	Group (a) panels: The non-axisymmetric components in $V_r$ at $2h$ at
	100, 300, and 1,000 orbits (left column), and their differences (right
	column). Group (b) and (c) panels: similar to group (a) panels, but
	for $V_{\phi}$ (b) and $V_{\theta}$ (c). The location of the planet is indicated by
	the cyan marker, and its size is set to $0.4R_{\rm H}$ , the expected size of
	the circumplanetary disk. The trajectories of the spirals in the sur-
	face density are indicated by the small green circles ((also shown in
	Fig. 4.1). Gap edges at $r = r_p - 2R_H$ and $r_p + 2R_H$ are marked with
	grey dashed circles. The magenta ellipse indicates the gas structure
	at L5. The two ends of the horseshoe flow inside the gap are indi-
	cated by black arrows and the strong converging flows are indicated
	by cyan arrows. The colorbars are in linear scale. See §4.3.1.2 for
	details

4.7 The three components in non-axisymmetric velocity perturbations along the primary spiral density waves (traced out by the green circles in Figs. 4.1 and 4.6) at 2h away from the midplane at 1,000 orbits for 4 simulations with different numerical resolutions: cells per scale height (CPH) of 7, 10, 14, and 20. We exclude the region within  $R_{\rm H}$  from the planet at 100 au due to insufficient resolution in the circumplanetary region. The velocity field along the spirals is converging with resolution. See §4.3.2 for further discussions. . . . 138

4.9 Successive residual channel maps of the same kind as panel (a-b) in Fig. 4.8 of the simulation with CPH= 20 at 1,000 orbits. Signals in the maps highlight non-axisymmetric velocity perturbations induced by the planet. Potentially detectable residuals are highlighted by  $3\sigma$  contours (green). We only mark  $3\sigma$  signals with a size bigger than a beam. Such signals are most prominently present in channels at  $V_{\rm ch}=1.8$  to 2.2 km/s (highlighted with a red frame). Grey and blue dashed lines denote gap edges and the primary spirals, respectively. The location of the planet is indicated by the cyan marker. The disk rotation direction is marked in the lower left panel. The colorbar is in a linear scale. See §4.4.1 for further discussions. . . . 141

4.10	Residual channel maps (the same kind as panel (a-b) in Fig. 4.8) of
	the simulation with CPH= 20 at $V_{\rm ch}=0.6$ (the (a) panels), 1.6 (b),
	and 2.2 km/s (c). Results at 100, 300, and 1,000 orbits are shown
	from top to bottom. Planet-induced non-axisymmetric kinematic
	signatures evolve with time. The planet is positioned at the position
	angle $\phi_p=315^\circ$ in the disk frame. Residual emissions stronger
	than $3\sigma=\pm$ 3.0 mJy/beam are marked with green contours. In
	each panel, the blue dashed curve represents the primary spirals at
	2h away from the midplane, and grey lines mark the inner and outer
	gap edge. The beam size is displayed at the bottom left. The disk
	rotation direction is marked in panel (a1). The colorbar is in a linear
	scale. See §4.4.2 for discussions
4.11	Resolution convergence test of synthetic channel maps. For
	each $V_{\rm ch}$ , the left and right columns present residuals (similar to
	Fig. 4.8(a-b)) and differences, respectively. Difference channel
	maps are obtained by subtracting residual channel maps at different
	resolutions. Residual or difference emission stronger than $3\sigma=\pm$
	3.0 mJy/beam are marked with green contours. The disk rotation
	direction is marked in the top left panel. The colorbar is in a linear
	scale. See §4.4.3 for discussions
4.12	Azimuthally averaged $\tau = 1$ surface of synthetic CO $J = 2 - 1$ emis-
	sion (blue line) of the simulation with CPH= 20 at 1,000 orbits.
	Dashed lines in magenta, cyan, and yellow represent 1, 2, and 3
	scale heights, respectively. The grey dashed-dotted lines mark the
	inner and outer gap edge. The planet is at $r = 100$ au
4.13	Similar to Fig. 4.3 but for $V_{\phi} - V_{\text{Kep}}$
4.14	Similar to Fig. 4.3 but for $V_{\theta}$

4.15	Comparison of $V_{\phi}$ perturbations obtained by subtracting azimuthal
	average background (left) and Keplerian background (right) from
	original FARGO3D simulation results. Note that the colorbars are
	in linear scale and the ranges differ between these two groups of
	panels
4.16	Successive channel maps of our disk model at 1,000 orbit and with
	CPH=20. Grey and blue dashed lines denote gap edges and the
	primary spirals, respectively. The location of the planet is indicated
	by the cyan marker. The disk rotation direction is marked in the
	lower left panel. The colorbar is in a linear scale

# **List of Tables**

2.1	FARGO3D main parameters. Parameters in each column below the
	second row in this table are corresponding to the cases of planet
	location $r_p = 4$ , 10, or 30 au, respectively
2.2	RADMC3D parameters
2.3	Comparison of inner and outer gap edge eccentricity $e$ of massive
	planets at different $r_p$ from iteration or non-iteration method. $e$ is
	measured by either "graph" or "formula" method and the averaged
	values of the last 500 orbits are marked as "mean" and the uncer-
	tainty are marked as "std". Values of $e > 0.05$ are highlighted with
	purple background
3.1	FARGO3D main parameters. Parameters in each column below the
	nineth row in this table are corresponding to the cases of planet
	location $r_p = 4$ , 10, or 30 au, respectively. Different $\alpha$ studies are
	only for cases of $100M_{\oplus}$
3.2	RADMC3D parameters
4.1	Temporal standard deviations (STD) of $V_r$ shown in Fig. 4.3 ( $V_r$
	within 5 orbits at 5 different locations at $t = 100$ , 300, and 1,000
	orbits)

## **Chapter 1**

# Introduction

Studying exoplanets has significant implications for understanding our place in the universe and the possibility of life on other planets outside the solar system. Since the first exoplanet was discovered around a Sun-like star in 1995 (Mayor & Queloz, 1995), more than 5,000 exoplanets have been detected and confirmed<sup>1</sup>. As the population of exoplanets grows rapidly, the diversity of exoplanetary systems highlights the importance of studying planet formation and early evolution.

The origins of our solar system and the formation of planets have been long-standing questions in astronomy and astrophysics. In the 18th century, German philosopher Immanuel Kant and French mathematician Pierre-Simon Laplace proposed the nebular hypothesis, suggesting that the solar system formed from a nebula of gas and dust. In the late 20th century, observations of disks around young stars provided direct evidence supporting the nebular hypothesis. More recently, in 2018, the first image of a young exoplanet forming in a circumstellar disk around PDS 70 was captured using near-infrared instruments (Keppler et al., 2018). This long journey, from the nebular hypothesis to the direct observation of a forming planet, marks a significant success in the study of planet formation and modern astronomy.

The title of this thesis is inspired by a classical musical form called the concerto. A concerto is a musical composition for a solo instrument (such as a piano, violin, or cello) accompanied by an orchestra. Typically, a concerto consists of three movements: fast, slow, and fast. The first movement is usually in sonata form,

https://exoplanets.nasa.gov

comprising an exposition, development, and recapitulation. The second movement is slower and more lyrical, while the third movement is faster and more lively.

Planet formation occurs in so-called protoplanetary disks (PPDs), which are gaseous disks surrounding young stars. A star with its surrounding protoplanetary disk can be likened to a conductor with an orchestra. The interaction between the orchestra and a soloist during a concerto mirrors the interaction between a planet and the protoplanetary disk...

# 1.1 History of concertos: protoplanetary disk formation

The formation process from molecular clouds to planetary systems has some parallels with the evolutionary history of concertos. The earliest form of the concerto is the concerto grosso, which emerged in the Baroque period<sup>2</sup>. A concerto grosso is a form of music played between a small group of soloists and the whole orchestra. In short, in a concerto grosso, there is no single instrument standing out from the orchestra. The concerto grosso is performed as a whole, which is similar to the prestellar core or protostar stage, where no planets stand out from the disk.

As it entered the Classical and Romantic periods, the popularity of the concerto grosso was replaced by the solo concerto, which features a single soloist accompanied by an orchestra. The solo concerto is still the most popular form of concerto today. The interaction between the soloist and the orchestra in a solo concerto is similar to the planet–disk interaction.

We show a schematic diagram of the process from the prestellar core to the formation of a planetary system in Figure 1.1. Based on observational features in the spectral energy distribution (SED), young stellar objects (YSOs) are classified from Class 0 to Class III (Adams et al., 1987).

A large, cold, and dense cloud of gas and dust in space, mostly composed of molecular hydrogen, is called a molecular cloud. Within the molecular cloud, some small, dense clumps collapse under their own gravity. These clumps, known as

<sup>&</sup>lt;sup>2</sup>https://en.wikipedia.org/wiki/Concerto grosso

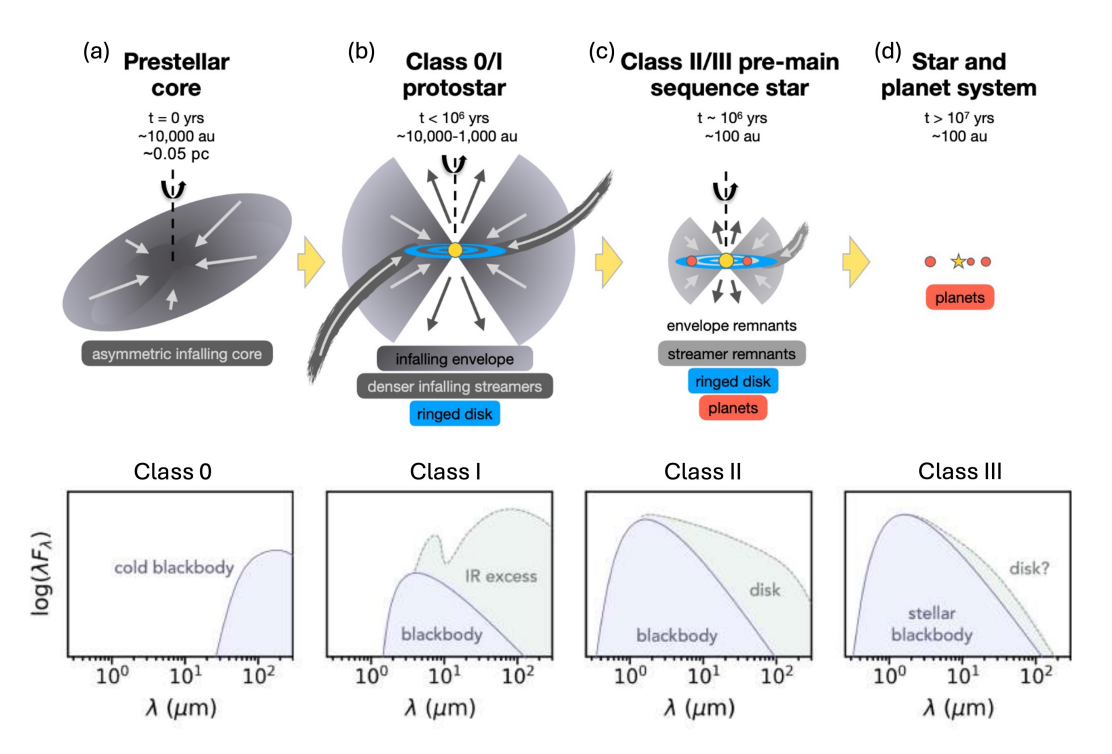


**Figure 1.1:** Schematic diagram illustrating the evolutionary sequence from a prestellar core to the formation of a planetary system, shown in panels (a)–(d). The spectral energy distribution (SED) features corresponding to Class 0, I, II, and III sources are depicted in the lower panels. The figure is adapted from Pineda et al. (2023); Keyte (2024).

prestellar cores, represent the initial stage of star formation (Figure 1.1(a)). The size of a prestellar core is typically on the order of  $10^4$  au. A prestellar core also carries angular momentum originating from large-scale turbulent motions.

On a timescale of approximately 10<sup>5</sup> years, the prestellar core collapses and forms a protostar along with a rotating disk around it (Figure 1.1(b)). Simultaneously, infall of material from the prestellar core to the disk creates a surrounding envelope. This stage is classified as Class 0. In the SED, envelope-dominated protostars exhibit high ratios of submillimeter to bolometric luminosity.

As protostars evolve over a few  $\times 10^5$  years, the circumstellar envelope becomes less dominant, and the central star and disk system become visible in the near-infrared (Class I). Recent discoveries of streamers, large-scale and narrow accretion filaments, in gas observations (Pineda et al., 2020) indicate that material is feeding the disk from scales of  $\sim 10^3$  au. These streamers can carry angular momentum and mass from large scales to the disk. This process could be a crucial

component in hydrodynamical simulations of the evolution from prestellar cores to disks.

At a timescale of  $\sim 10^6$  years, the YSO evolves into a pre-main sequence star with a protoplanetary disk and a negligible circumstellar envelope (Class II; Figure 1.1(c)). In the SED, Class II YSOs are characterized by near-infrared and submillimeter excesses, and the star becomes visible at optical wavelengths. A key feature of gaseous protoplanetary disks is the common presence of substructures, which are often interpreted as signatures of planet–disk interactions. In Class II disks, the "late-stage infall" process involving streamers may still be ongoing (e.g., Ginski et al., 2021; Speedie et al., 2025).

On a timescale of  $\sim 10^7$  years, as gas is dispersed through stellar accretion, photoevaporation, and planet formation, the disk evolves into a debris disk (Class III). In the SED, the star remains visible at optical wavelengths but shows very little infrared excess. A debris disk consists mainly of planets and dust particles, along with planetesimals which are similar to asteroid belts. After this stage, the system evolves into a mature planetary system (Figure 1.1(d)).

#### 1.2 Disk observations

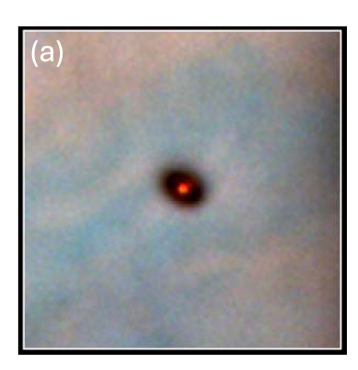
In this section, we discuss observations of protoplanetary disks (PPDs), which correspond to the Class II phase of YSOs described in the previous section. We also discuss observations of substructures within these disks.

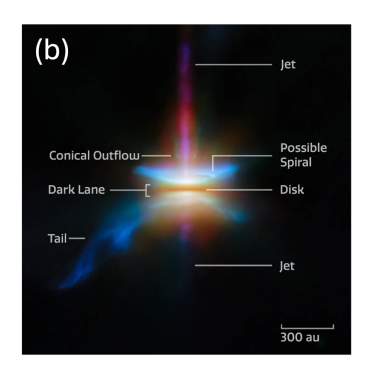
### 1.2.1 Optical and near-infrared observations

The central star and the innermost regions of the disk emit primarily at optical and near-infrared (NIR) wavelengths. Thermal emission from planets in disks might be also observed in these wavelengths. Beyond these compact regions, optical and NIR wavelengths mainly trace scattered light from small (micron-sized) dust grains on the disk surface.

In Figure 1.2, we show several examples of scattered light images of disks. Panel (a)<sup>3</sup> shows one of the well-known Orion proplyds, captured by the Hubble

<sup>&</sup>lt;sup>3</sup>https://esahubble.org/images/opo9545b/





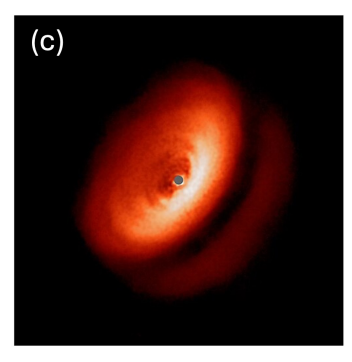


**Figure 1.2:** Scattered light images of protoplanetary disks. From left to right: the Orion proplyd observed by the Hubble Space Telescope (HST), HH 30 by the James Webb Space Telescope (JWST), and IM Lup by VLT/SPHERE. Image credits: (a) Mark McCaughrean (Max Planck Institute for Astronomy), C. Robert O'Dell (Rice University), and NASA/ESA; (b) ESA/Webb, NASA & CSA, Tazaki et al.; (c) ESO/H. Avenhaus et al., DARTT-S collaboration.

Space Telescope (HST). This is one of the first images of a protoplanetary disk. The proplyd is a disk-like structure surrounding a young star. Panel (b) shows HH 30, observed by the James Webb Space Telescope (JWST). This image not only reveals an edge-on disk but also shows outflows and jets from the poles. Panel (c)<sup>4</sup> displays IM Lup, imaged by the Very Large Telescope (VLT). This image shows a disk with multiple bright and dark rings on the surface and a dark lane along the midplane.

Recently, most scattered light images have been obtained by 8-meter-class telescopes equipped with adaptive optics (AO) and polarimeters, such as VLT/SPHERE, Gemini/GPI, and Subaru/HiCIAO. Large programs, such as DES-TINY (Ginski et al., 2021), have been conducted to survey disks in nearby star-forming regions. As another example, Bohn et al. (2021) studied misalignments between the inner and outer disks of 20 transition disks to explain shadows observed in VLT/SPHERE scattered light images.

### 1.2.2 Dust continuum and gas observation

Dust continuum emission in submillimeter and millimeter (sub-mm/mm) wavelengths provides information about large dust grains (mm-sized) in the disk midplane. The Atacama Large Millimeter/submillimeter Array (ALMA) has brought

<sup>4</sup>https://www.eso.org/public/images/eso1811c/

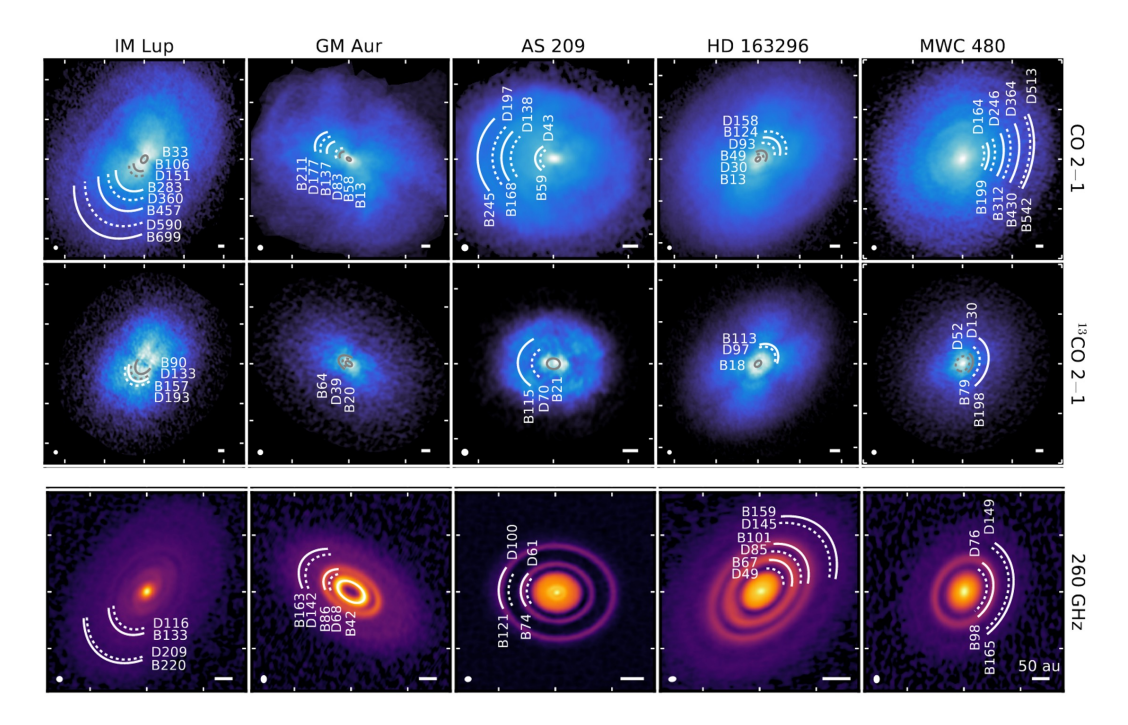


**Figure 1.3:** Gallery of DSHARP and MAPS disk images. Five disks that are included in both the DSHARP and MAPS samples are shown to illustrate how dust continuum and chemical substructures (CO and <sup>13</sup>CO), such as gaps and rings, differ in the same disks.

revolutionary progress to protoplanetary disk studies at (sub-)mm wavelengths. In the pre-ALMA era, using the Submillimeter Array (SMA), Andrews et al. (2011) presented a survey of 12 transition disks (TDs, disks with large dust cavities) at 0.3 arcsecond resolution and suggested that the presence of giant planets or brown dwarfs could explain the observed cavities. Thanks to ALMA's very high spatial resolution (up to 0.007 arcseconds at 650 GHz (Cleeves et al., 2015; Isella, 2020)) and high sensitivity, we now have much more detailed information about substructures in disks. The first high-angular-resolution (0.025 arcsec) ALMA image of a protoplanetary disk revealed astonishing annular rings and gap substructures in the dust continuum of the HL Tau disk (ALMA Partnership et al., 2015).

Besides obtaining high-resolution images of individual disks, ALMA has also made considerable progress in PPD surveys. For example, the DSHARP project studied dust continuum emission from 18 Class II disks (Andrews et al., 2018b; Huang et al., 2018), and found that substructures are common in the DSHARP sample. Later, the MAPS program surveyed molecular line emission from five disks

(Öberg et al., 2021; Law et al., 2021) and investigated chemical structures in disks at a resolution of 10 au. MAPS also found that substructures in different molecular lines are common in disks. Interestingly, the substructures seen in dust continuum and those seen in molecular line emission are not always spatially correlated. We show a gallery of the five disks included in both surveys in Fig. 1.3. In addition to these two surveys, Long et al. (2018) conducted an ALMA dust continuum survey of rings and gaps in disks in the Taurus region and found that low-mass planets in low-turbulence disks could explain these structures.

#### **1.2.3** Observation of Substructures

Below, we briefly list some of the most common substructures observed in PPDs, including gaps/rings, spirals, crescents and kinematic substructures. These features are detected in near-infrared (NIR) observations, dust continuum emission, or molecular gas lines. We will discuss the origins of these substructures in Sections 1.2.4 and 1.5.

It is worth noting that based on results from the large ALMA program eDisk (Ohashi et al., 2023), continuum substructures such as rings or spirals may already form during the Class 0/I phase, although they appear less frequently than in Class II disks. This suggests either that the high optical depth in dust continuum emission hinders the detection of substructures in Class 0/I disks, or that substructures develop rapidly during the transition from Class 0/I to Class II. In this thesis, we will focus on substructures in Class II disks. In addition, it is important to note that the number of observed substructures is affected by observational selection effects. Lower spatial resolution leads to fewer detected substructures, even though the actual number present in disks may be higher.

Gaps/rings Dark gaps and bright rings, as shown in Figure 1.3, are the most common substructures observed in disks. Gaps and rings appear about ten times more frequently in dust continuum observations than in NIR scattered light images (Bae et al., 2022). A possible explanation is that large dust particles are trapped in pressure bumps, which coincide with the observed millimeter dust rings.

Some well-known examples of disks with multiple gaps and rings include HL

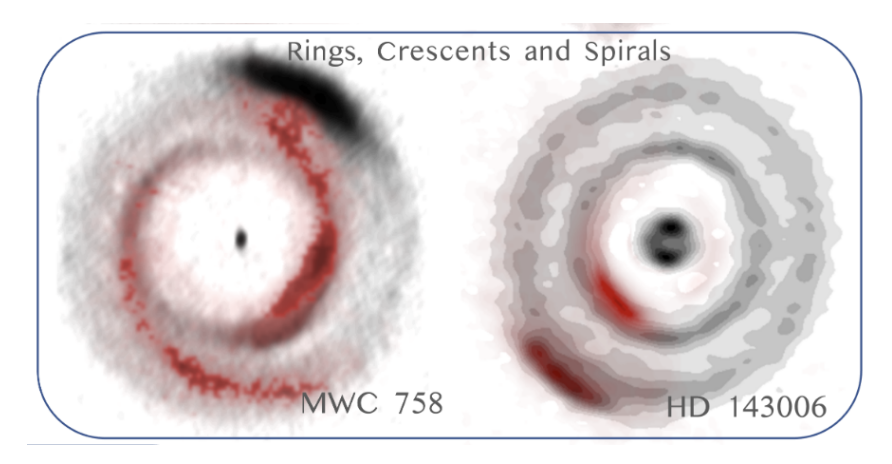


**Figure 1.4:** Illustration of rings, crescents, and spirals in disks. The grey color represents dust continuum emission, while the red color indicates near-infrared (NIR) emission. The figure is adapted from Bae et al. (2022).

Tau with seven gaps (ALMA Partnership et al., 2015), AS 209 with seven gaps (Huang et al., 2018), TW Hya with five gaps (Huang et al., 2018), HD 163296 with four gaps (Isella & Turner, 2018), CI Tau with four gaps (Clarke et al., 2018), and RU Lup with four gaps (Huang et al., 2018).

**Spirals** Spirals are another common substructure observed in disks. Figure 1.4 shows two large-scale spirals observed in NIR in the disk around MWC 758. Spirals are typically detected in NIR, and occasionally in dust continuum or molecular line emission. Interestingly, the number of spiral arms detected in a disk can range from one to eight, although more than 50% of disks with observed spirals exhibit two arms (Bae et al., 2022).

Crescents Crescents are rings with azimuthal variations in brightness. If the azimuthal brightness contrast is close to unity, the structure is considered a ring. For crescents, the minimum azimuthal intensity contrast is 1.5 (Bae et al., 2022). In other literature, crescents may also be referred to as arcs or vortices. We show an example of two crescents in the HD 143006 disk in Figure 1.4. The crescents are detected in both NIR and millimeter continuum. Additionally, a crescent is observed at the outer edge of the MWC 758 disk in dust continuum emission.

One of the most well-known examples of a crescent is the disk around Oph IRS 48, a transition disk with a large dust cavity. The crescent in this disk is detected in millimeter continuum with an azimuthal intensity contrast greater than

130. This represents a strong azimuthal dust trap in millimeter-sized grains, while the micron-sized grains and gas exhibit an axisymmetric distribution (van der Marel et al., 2013).

**Kinematic substructures** In addition to substructures identified in intensity maps, we can also detect kinematic substructures from channel maps of gas molecular lines. As shown in panel (a) of Figure 1.5, we can image a disk across different velocity channels (or frequencies), producing a 3D data cube. Sweeping through these frequencies reveals the typical butterfly pattern in channel maps.

For a single channel map (Figure 1.5 (b)) at velocity channel  $V_{\rm ch}$ , the emission originates from regions with a line-of-sight velocity  $V_{\rm LoS} = V_{\rm ch}$ . In practice, observational spectral resolution is finite, so  $V_{\rm ch}$  corresponds to a velocity range of  $V_{\rm ch} \pm 0.5 \Delta v$ , where  $\Delta v$  is the channel width. In addition, the observed emission in a single channel can come from both the upper and lower surfaces of the disk, and from both the near and far sides.

By integrating the data cube along the frequency axis, we obtain moment maps. The zeroth moment map (Figure 1.5 (f)) is the integrated intensity map, calculated as  $M_0 = \sum_{i=1}^N I_i$ , where i indexes the velocity channels and N is the number of channels. The first moment map (Figure 1.5 (e)) is the velocity map, given by  $M_1 = \sum_{i=1}^N I_i v_i / M_0$ . In the velocity map, red and blue colors indicate redshifted and blueshifted emission, respectively. The moment 1 map is often used to trace disk rotation.

Besides imaging, spectral line profiles are also valuable for studying disk kinematics. A local line profile at a given spatial position (e.g. Figure 1.5 (b), top panel) can reveal the intensity as a function of velocity and allow us to compare emission from the upper and lower disk surfaces. By integrating over all spatial pixels, we obtain the spatially integrated line profile (Figure 1.5 (d)), which typically shows a classical double-peaked profile in a Keplerian rotating disk.

For the tracers of kinematic observations, CO and its isotopologues are widely used in disks, such as HD 169142 (Yu et al., 2021) and TW Hya (Teague et al., 2022a,b). In kinematic observations, we are particularly interested in emission fea-

tures that deviate from the expected Keplerian rotation. Such non-Keplerian perturbations may be caused by planets (see also Section 1.5.3) or other dynamical processes such as infall, outflows, or gravitational instabilities. Recently, a large ALMA survey, exoALMA, has been conducted to search for kinematic signatures of planets and other physical processes in disks (Teague et al., 2025). The survey studies gas distribution and dynamics with high sensitivity (1.5 K in a 100 m/s channel), high spatial resolution (0.1 arcsec), and high spectral resolution (27 m/s).

#### 1.2.4 Substructure formation without planets

The origin of substructures observed in protoplanetary disks remains an open question. While the most compelling explanation involves planet-disk interactions (discussed further in Section 1.5), several alternative physical mechanisms that do not require planets have been proposed to account for the observations. These include secular gravitational instabilities (Takahashi & Inutsuka, 2014, see below for more details), zonal flows (Flock et al., 2015), icelines (Zhang et al., 2015; Pinilla et al., 2017, see also the introduction in Chapter 3), and disk winds (Bai, 2017).

**Gravitational instability** If the disk is massive enough (disk to star mass ratio about 0.1), the self-gravity of the disk can be important and lead to gravitational instability (GI). The critical Toomre Q parameter is used to determine whether the disk is gravitationally unstable. The disk is marginally unstable to GI when (Toomre, 1964)

$$Q \equiv \frac{c_{\rm s}\Omega}{\pi G\Sigma} < 1 \tag{1.1}$$

where  $c_s$  is the sound speed,  $\Omega$  is the angular velocity, G is the gravitational constant, and  $\Sigma$  is the surface density of the disk.

GI is a large-scale instability that may drive the formation of spiral structures. Dipierro et al. (2014, 2015); Cadman et al. (2020) modeled GI-induced spirals in self-gravitating (SG) disks, as well as the associated dust trapping within these spirals. Their results suggested that GI spirals could be detectable with ALMA observations and near-infrared scattered light imaging. However, Rowther et al. (2021) used smoothed particle hydrodynamics (SPH) simulations to demonstrate that disk

warping can suppress the development of GI spirals.

GI can also leave kinematic imprints in disks. Terry et al. (2021) empirically quantified the relationship between the amplitude of GI-induced "wiggles" and the disk-to-star mass ratio. Longarini et al. (2021) argued that gravitationally unstable disks should exhibit clear kinematic signatures in the form of velocity perturbations. Recently, Speedie et al. (2024) used ALMA CO observations to reveal the kinematic features of GI spirals in the AB Aurigae disk.

#### 1.3 The Orchestra: structure of disks

In this section, we discuss the basic structure of protoplanetary disks (PPDs) without perturbers (e.g. planets). Figure 1.6 shows a schematic diagram of the structure of a PPD. A PPD is a rotating disk of gas and dust surrounding a young star.

#### 1.3.1 Governing equations

We summarize the basic hydrodynamic (HD) equations governing the gas and dust in a protoplanetary disk. These include the continuity equation, the momentum equation, and the energy equation. Assuming a disk in 3D spherical coordinates (R,  $\phi$ ,  $\theta$ ) = (radial, azimuthal, colatitude). The gas and dust densities are denoted by  $\rho_{\rm g}$  and  $\rho_i$ , respectively, while the gas and dust velocities are represented by  $\boldsymbol{u}$  and  $\boldsymbol{v}_i$ . The subscript i indexes the dust species, ranging from 1 to  $N_{\rm dust}$ . Different dust species correspond to different grain sizes,  $a_i$ , and the number density of a grain size is typically described by a power law,  $n(a) \propto a^{-3.5}$  (Mathis et al., 1977). The dust species are modeled as pressureless fluids.

The continuity equations and momentum equations are given by

$$\frac{\partial \rho_{g}}{\partial t} + \nabla \cdot (\rho_{g} \mathbf{u}) = 0, \tag{1.2}$$

$$\rho_{g}\left(\frac{\partial \boldsymbol{u}}{\partial t} + \boldsymbol{u} \cdot \nabla \boldsymbol{u}\right) = -\nabla P - \rho_{g} \nabla \Phi - \nabla \cdot \tau - \sum_{i} \rho_{i} \boldsymbol{f}_{i}, \tag{1.3}$$

$$\frac{\partial \rho_i}{\partial t} + \nabla \cdot (\rho_i \mathbf{v}_i + \mathbf{j}_i) = 0, \tag{1.4}$$

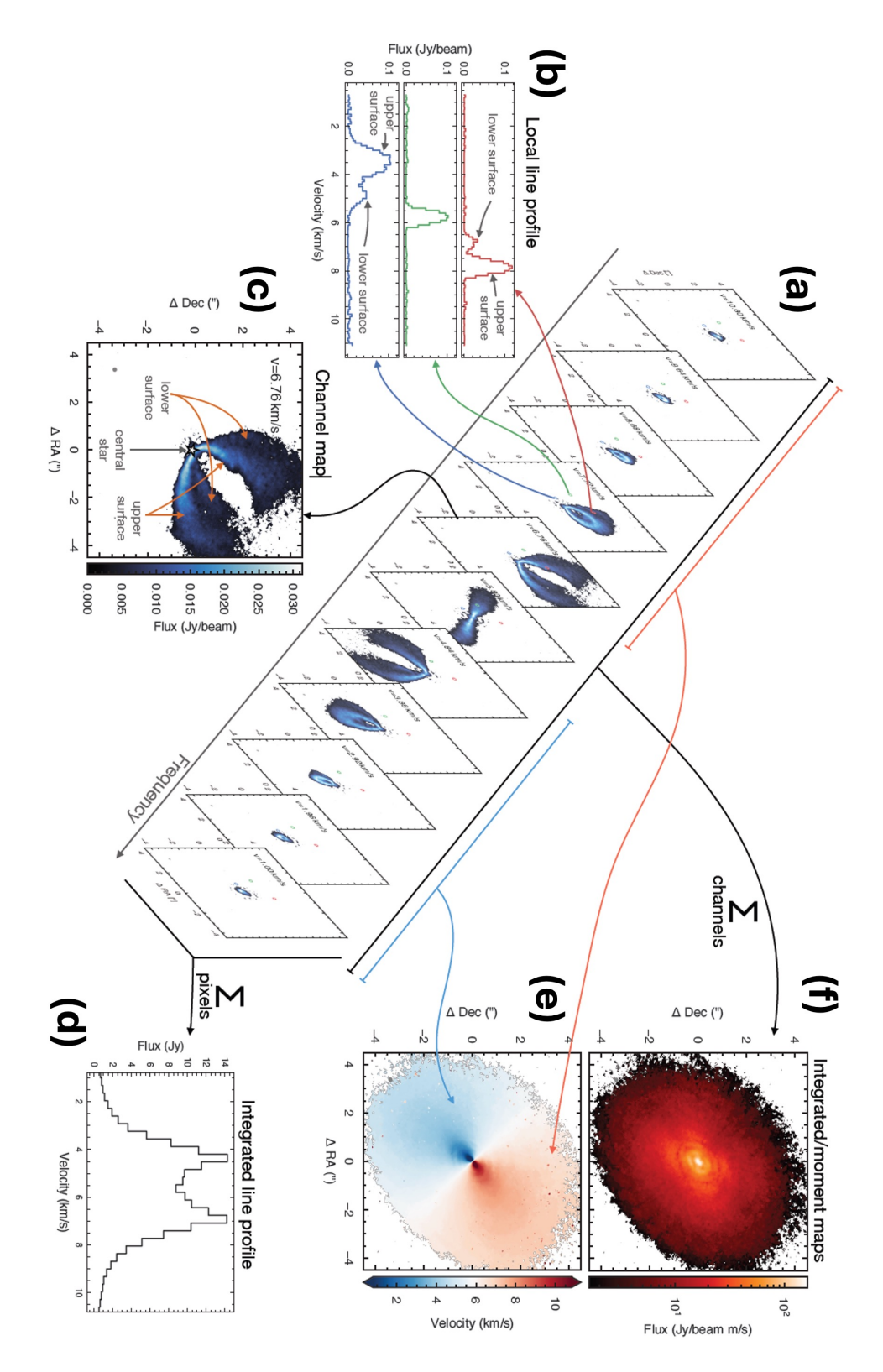


**Figure 1.5:** Illustration of channel maps of gas molecular line observations. Panel (a) shows the channel maps of the CO line in a disk. Panel (b) shows the line profiles at three given spatial positions. Panel (c) shows a channel map of the CO line at a given velocity channel. Panel (d) shows the spatially integrated line profile. Panel (e) shows the moment 1 map, which is the velocity map. Panel (f) shows the zeroth moment map, which is the integrated intensity map. The figure is adapted from Pinte et al. (2022).

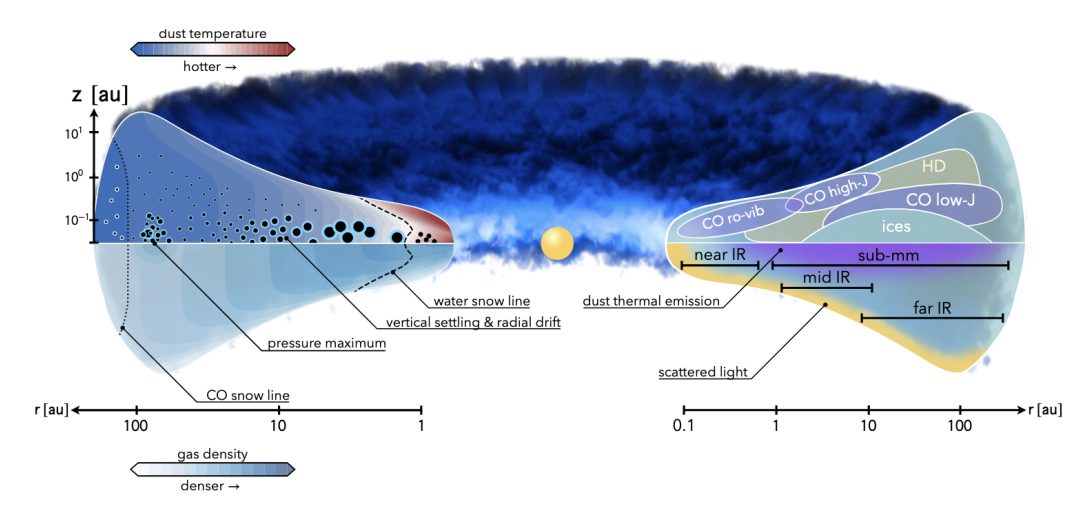


**Figure 1.6:** Schematic diagram of the structure of a protoplanetary disk. The figure is adapted from Miotello et al. (2022).

$$\rho_i \left( \frac{\partial \mathbf{v}_i}{\partial t} + \mathbf{v}_i \cdot \nabla \mathbf{v}_i \right) = -\rho_i \nabla \phi + \rho_i \mathbf{f}_i. \tag{1.5}$$

Under a widely used viscous-driven accretion disk model (see also Section 1.4.1), the viscous stress tensor  $\tau$  in Equation (1.3) is given by

$$\tau \equiv \rho_{g} v \left[ \nabla \boldsymbol{u} + (\nabla \boldsymbol{u})^{T} - \frac{2}{3} (\nabla \cdot \boldsymbol{u}) \boldsymbol{I} \right], \tag{1.6}$$

where I is the identity tensor, v is the kinematic viscosity, defined as (Shakura & Sunyaev, 1973)

$$v = \alpha c_{\rm S} h_{\rm g} \tag{1.7}$$

where  $\alpha$  is the dimensionless viscosity parameter,  $c_s$  is the sound speed, and  $h_g$  is the disk gas scale height. The value of  $\alpha$  is usually set to be between  $10^{-4}$  and  $10^{-2}$  (see dicussion in Section 1.4.1).

The gravitational potential  $\phi$  in Equation (1.3) from the star is given by

$$\Phi = -\frac{GM_{\star}}{R}.\tag{1.8}$$

The quantity  $f_i$  in Equation (1.3) and (1.5) is the drag force acceleration between gas and dust, which is given by (Whipple, 1972)

$$\boldsymbol{f}_i = \frac{\Omega_K}{\mathrm{St}_i} (\boldsymbol{u} - \boldsymbol{v}_i). \tag{1.9}$$

The Stokes number  $St_i$  is calculated by (Weidenschilling, 1977)

$$St_i = \frac{\rho_s a_i}{\rho_g c_S},\tag{1.10}$$

where  $\rho_s$  is the internal density of the dust particle.

 $\mathbf{j}_i$  in Equation (1.4) is the dust diffusion flux, which is given by Morfill & Voelk (1984)

$$\mathbf{j}_i = -D_i(\rho_g + \rho_i) \nabla \left( \frac{\rho_i}{\rho_g + \rho_i} \right). \tag{1.11}$$

And the dust diffusion coefficient  $D_i$  is a function of viscosity and Stokes number, which is given by Youdin & Lithwick (2007)

$$D_i = v \frac{1 + St + 4St_i^2}{(1 + St_i^2)^2}.$$
 (1.12)

For small particles,  $St_i \ll 1$ , we have  $D_i \simeq v$ .

In addition to the multifluid mass and momentum equations for gas and dust, energy equations can also be included. However, these become complex when accounting for various heating and cooling mechanisms, as well as radiative transfer in disks. For simplicity, many disk models adopt the locally isothermal approximation, assuming efficient cooling due to the disc being optically thin in dust continuum emission. As a result, such models have constant temperature profile.

We are primarily concerned with three fundamental physical properties in a PPD: density, temperature, and velocity—for both gas and dust components. Note that we use  $(r, \phi, z)$  denote cylindrical radius, azimuth, and height. Assuming axisymmetry and steady state (ignoring time evolution), each property has both radial and vertical structure, (r,z). In the following, we discuss how these properties are distributed in a PPD without embedded planets.

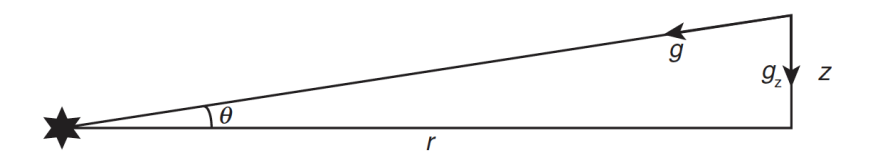


Figure 1.7: Illustration of the radial and vertical coordinates of a disk with the star's gravity.

#### 1.3.2 Disk density

Gas density The surface density  $\Sigma$  represents the mass per unit area of the disk. Assuming an axisymmetric disk, the gas surface density  $\Sigma_g$  is typically described by a power-law profile:

$$\Sigma_{g}(r) = \Sigma_{g,0} \left(\frac{r}{r_0}\right)^{-p},\tag{1.13}$$

where  $\Sigma_{g,0}$  is the gas surface density at a reference radius  $r_0$ , and p is the powerlaw index. In this thesis, p is typically set to 1 (see Section 1.4.1 for justification of this value), although other values are used in the literature. For example, Hayashi (1981) found p = 3/2 for the minimum mass solar nebula (MMSN) model.

The vertical gas density structure of disks is usually derived from hydrostatic equilibrium. The vertical coordinate *z* is defined as the height above the midplane. Assuming the gravity is dominated by the central star (neglecting the disk's self-gravity), and setting the vertical velocity to zero in momentum conservation, the hydrostatic equilibrium equation is given by:

$$\frac{dP}{dz} = -\rho_g g_z,\tag{1.14}$$

where P is the pressure,  $\rho$  is the density. The vertical gravitational acceleration  $g_z$  is given by (see Figure 1.7)

$$g_z = \frac{GM_{\star}}{r^2 + z^2} \frac{z}{\sqrt{r^2 + z^2}}.$$
 (1.15)

If we adopt an isothermal equation of state, then the pressure is given by

$$P = \rho_g c_s^2, \tag{1.16}$$

where  $c_s$  is the sound speed.  $c_s$  is related to the disk pressure scale height  $h_g$  by

$$c_s = h_g \Omega, \tag{1.17}$$

where  $\Omega$  is the angular velocity. The angular velocity is given by

$$\Omega = \sqrt{\frac{GM_{\star}}{r^3}}. (1.18)$$

Therefore, we obtain a Gaussian vertical density profile of gas

$$\rho_g(z) = \rho_{g,mid} \exp\left(-\frac{z^2}{2h_g^2}\right),\tag{1.19}$$

where  $\rho_{g,mid}$  is the gas density at the midplane, written as

$$\rho_{g,mid} = \frac{\Sigma_g}{\sqrt{2\pi}h_g}. (1.20)$$

**Dust density** The distribution of dust in protoplanetary disks is influenced by the coupling between gas and dust, which depends on the size of the dust particles. Small dust particles are well-coupled to the gas and tend to follow its motion, while larger particles decouple from the gas and experience radial drift toward the star or become trapped in pressure bumps (Whipple, 1972; Weidenschilling, 1977). These pressure bumps, formed through planet—disk interactions or instabilities, can act as dust traps preventing the rapid inward drift of larger particles (e.g., Pinilla et al., 2012a). This process plays a critical role in the formation of planetesimals and the overall evolution of the disk's structure.

In a disk under vertical hydrostatic equilibrium, where dust settling is balanced by turbulent diffusion, the vertical dust density profile can be described by (Fromang & Nelson, 2009):

$$\rho_{\rm d}(z) = \rho_{\rm d,mid} \exp \left[ -\frac{z^2}{2h_{\rm g}^2} - \frac{\rm St_{mid}}{\alpha} \left( \exp \left( \frac{z^2}{2h_{\rm g}^2} \right) - 1 \right) \right], \tag{1.21}$$

where  $\rho_{d,mid}$  is the dust density at the midplane and  $St_{mid}$  is the Stokes number at

the midplane.

if  $z \ll h_g$ , then we have a Gaussian vertical density profile of dust approximately:

$$\rho_{\rm d}(z) \approx \rho_{\rm d,mid} \exp\left[-\frac{z^2}{2h_{\rm d}^2}\right].$$
(1.22)

where  $h_d$  is the dust scale height, which is given by

$$h_{\rm d} = h_{\rm g} \sqrt{\frac{\alpha}{{\rm St} + \alpha}} \tag{1.23}$$

#### 1.3.3 Disk velocity

**Gas velocity** For an accretion disk with an accretion rate  $\dot{M}$ , the inward radial velocity  $v_{r,g}$  is given by

$$v_{r,g} = -\frac{\dot{M}}{2\pi r \Sigma_g}. (1.24)$$

The radial and vertical velocities in disks,  $v_r$  and  $v_z$ , are typically small compared to the azimuthal velocity  $v_{\phi}$ , and are therefore often neglected. For an axisymmetric disk, the azimuthal gas velocity  $v_{\phi,g}$  is given by:

$$\frac{v_{\phi,g}(r,z)^2}{r} = \frac{GM_{\star}r}{(r^2 + z^2)^{3/2}} + \frac{1}{\rho_g} \frac{\partial P}{\partial r} + \frac{\partial \phi_g}{\partial r}, \tag{1.25}$$

where  $\phi_g$  is the gravitational potential of the gas. The first term on the right-hand side is the gravitational force from the star, and the second term is the pressure gradient force. The third term is the disk self-gravity. For more discussion about the self-gravity of disks, please refer to Section 1.2.4.

If we ignore the self-gravity of the disk, in the disk midplane (z=0), the azimuthal velocity can be written as

$$v_{\phi,g} = v_{\rm K} \left( 1 - n \frac{c_{\rm s}^2}{v_{\rm K}^2} \right)^{1/2} \tag{1.26}$$

where  $v_k$  is the Keplerian velocity,  $v_{\rm K}=\sqrt{\frac{GM_{\star}}{r}}$ . n comes from  $P=P_0\left(\frac{r}{r_0}\right)^{-n}$ .

Thus, the azimuthal gas velocity is sub-Keplerian. For an isothermal disk with surface density  $\Sigma_g \propto r^{-1}$ , gas temperature  $T_g \propto r^{-1/2}$ , n=2.75. Assuming a typical value for the disk aspect ratio, h/r=0.1, we find that  $v_{\phi,g}$  is one percent slower than the Keplerian velocity  $v_{\rm K}$ .

**Dust velocity** For dust velocity in a disk without perturbers, since dust does not feel the pressure gradient force, it moves azimuthally at the Keplerian velocity.

$$v_{\phi,d} = v_{\mathbf{K}}.\tag{1.27}$$

The radial dust velocity depends on the aerodynamic drift between gas and dust (Whipple, 1972; Weidenschilling, 1977; Takeuchi & Lin, 2002).

$$v_{r,d} = \frac{St^{-1}v_{r,g} - \eta v_K}{St + St^{-1}},$$
(1.28)

where

$$\eta = -\left(\frac{c_s}{v_K}\right)^2 \frac{\mathrm{d}\ln P}{\mathrm{d}\ln r}.\tag{1.29}$$

For small particles with  $St \ll 1$ , the radial velocity of dust can be approximated as  $v_{r,d} \approx v_{r,g} - St\eta v_K \approx v_{r,g}$ , indicating that the dust closely follows the gas motion. For larger particles, especially when St = 1, the radial drift velocity reaches a maximum, with  $v_{r,d} = -0.5\eta v_K$ . Assuming a typical value of  $\eta \sim 10^{-3}$ , this yields  $v_{r,d} \sim 10^{-3} v_K$ . Consequently, large dust particles will drift inward and be lost on a timescale of approximately  $10^3$  orbital periods. Therefore, without any dust traps, large dust particles can be lost from the disk quickly.

# 1.3.4 Disk temperature

In this section, we perform a simple calculation of the disk radial temperature profile.

**Dust temperature** Consider a dust grain of size a located at a distance r from the central star. The equilibrium temperature of the dust grain,  $T_{\text{eqm}}$ , is determined by the balance between the absorbed stellar radiation (heating) and the thermal radiation it emits (cooling), assuming the grain is a blackbody.

$$\frac{L_{\star}}{4\pi r^2}\pi a^2 = 4\pi a^2 \sigma_{\rm SB} T_{\rm eqm}^4,\tag{1.30}$$

where  $L_{\star}$  is the stellar luminosity,  $\sigma_{SB}$  is the Stefan-Boltzmann constant. Therefore, the equilibrium temperature of the dust grain is given by

$$T_d = T_{\text{eqm}} = \left(\frac{L_{\star}}{16\pi^2 \sigma_{\text{SB}} r^2}\right)^{1/4} \propto r^{-1/2}.$$
 (1.31)

This simple calculation shows the dust temperature at a distance r from the star. However, for a real protoplanetary disk, the temperature profile is more complex due to the effects of disk geometry and radiative transfer (Chiang & Goldreich, 1997).

Gas temperature If we assume the gas is in thermal equilibrium with the dust, then the gas temperature  $T_{\rm g}$  is equal to the dust temperature  $T_{\rm d}$ . However, in some substructures of disks (e.g., gaps), the gas temperature can differ from the dust temperature (e.g., Facchini et al., 2018). Therefore, careful physico-chemical modeling of disks is required to accurately determine the gas temperature.

By using the disk temperature, we can determine the geometry of the disk. Due to the ideal gas law, the gas temperature T of the disk is related to the pressure and density by

$$P = \rho_g k_B T_g / (\mu m_H), \tag{1.32}$$

where  $k_B$  is the Boltzmann constant. So under the isothermal assumption, we get the relation between sound speed and temperature

$$c_s = \sqrt{\frac{k_B T_g}{\mu m_H}} \propto T_g^{0.5}. \tag{1.33}$$

Combine Equation (1.31) and (1.33), we can get the shape of the disk is flared

as

$$h_g = \frac{c_s}{\Omega} = \sqrt{\frac{k_B T_g}{\mu m_H}} \left(\frac{r^3}{GM_\star}\right)^{0.5} \propto r^{1.25}.$$
 (1.34)

The disk temperature plays an important role in the disk chemistry and the distribution of volatiles. Icelines are the locations where volatiles freeze out onto

dust grains due to the low temperature. The location of icelines is crucial for the formation of planets and the compositions of planets.

### 1.3.5 Iceline and disk composition

Icelines are important thermal structures in disks, which is determined by the disk temperature structure. An iceline of a specific molecule is the radius where the temperature is low enough so that such molecules freeze out from the gas phase onto dust grains (see upper part in Figure 1.8). Different molecules have different icelines, which are determined by the sublimation temperature  $T_{\rm sub}$  of the molecules. For example,  $T_{\rm sub}$  of H<sub>2</sub>O is around 150 K, while that of CO<sub>2</sub> is around 50 K. The  $T_{\rm sub}$  of CO is around 20 K. A more rigorous way to obtain  $T_{\rm sub}$  requires considering its dependence on pressure, rather than assuming it to be constant (Hollenbach et al., 2009). Qi et al. (2013); Zhang et al. (2017) reported the direct measurement of the CO iceline at around 20 au in TW Hya disk.

The lower part of Figure 1.8 shows the Carbon to Oxygen (C/O) ratio is changed at the iceline locations of H<sub>2</sub>O, CO<sub>2</sub>, and CO. The C/O ratio is a key parameter in determining the composition of planet atmosphere (Öberg et al., 2011). Also, by comparing the exoplanet atmosphere with the chemical composition in disk, we can trace the formation history of planets. Recently, The ALMA Disk-Exoplanet C/Onnection (DECO) program is proposed to study the C/O ratio of 80 disks. This survey will improve our understanding of disk and exoplanet chemical diversity.

# 1.4 Disk evolution

Moving beyond the steady-state picture of disks discussed in the previous section, we know that a protoplanetary disk is a dynamic system that evolves over time. The ultimate outcome of disk evolution is the formation of planetary systems. In our solar system, 99% of the mass resides in the Sun, while 98% of the angular momentum is contained in the planets. A protoplanetary disk is an accretion disk, requiring mechanisms to transport mass inward and angular momentum outward. Two primary mechanisms have been proposed to drive this evolution: disk viscosity

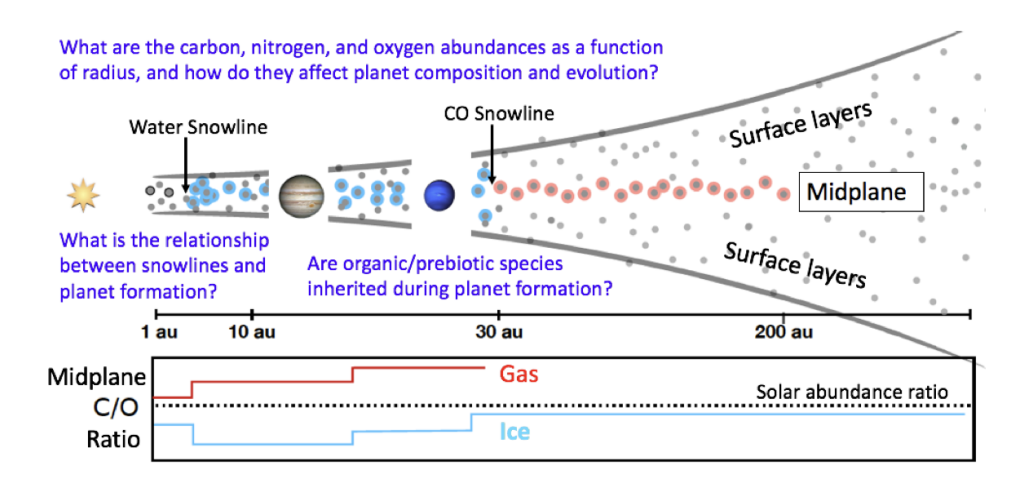


**Figure 1.8:** Schematic diagram of icelines in disks (upper) and the corresponding Carbon to Oxygen (C/O) ratio (lower). The figure is adapted from Cleeves et al. (2020).

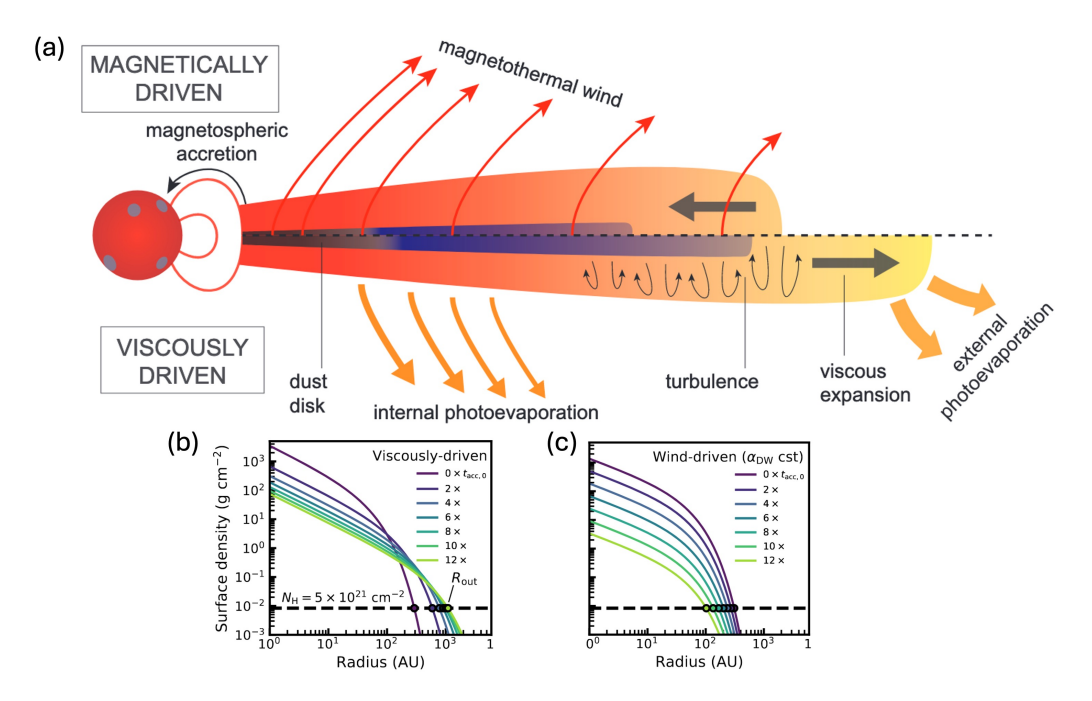


**Figure 1.9:** Panel (a) shows a schematic diagram of two disk evolution models: the viscous disk model (lower) and the magnetic winds model (upper). Panels (b) and (c) show the time evolution of the disk gas surface density in the viscous disk model and the MHD wind model, respectively. The figure is adapted from Trapman et al. (2021); Manara et al. (2022).

and disk winds. However, it remains an open question which of these mechanisms plays the dominant role in the evolution of protoplanetary disks.

#### 1.4.1 Disk viscosity

**Viscosity theory** For a viscous disk model, accretion is the results of redistribution of angular momentum. Such angular momentum transport is driven by the internal turbulence (or viscosity) in the disk (Shakura & Sunyaev, 1973; Lynden-Bell & Pringle, 1974). The angular momentum is transported outward and the disk size expands over time ("viscous spreading") (see the lower part of Figure 1.9(a)).

Combining the continuity equation (Equation (1.2)) and the azimuthal component of the momentum equation (Equation (1.3)), we can obtain how the gas surface density  $\Sigma_g$  evolves with time t and radius r in a Keplerian disk (Lynden-Bell & Pringle, 1974):

$$\frac{\partial \Sigma_g}{\partial t} = \frac{3}{r} \frac{\partial}{\partial r} \left[ r^{1/2} \frac{\partial}{\partial r} \left( v \Sigma_g r^{1/2} \right) \right]$$
 (1.35)

where v is the kinematic viscosity, which is decribed by Equation (1.7),  $v = \alpha c_s h_g$ .

Assuming the viscosity with a power law profile  $v \propto r$  (this means  $T \propto r^{-0.5}$ , Hartmann et al., 1998), we can get the "self-similar" solution of Equation (1.35) (Lynden-Bell & Pringle, 1974):

$$\Sigma_g(r,t) = \frac{M_0}{2\pi r_c^2} \left(\frac{r}{r_c}\right)^{-1} T^{-3/2} \exp\left(-\frac{(r/r_c)}{T}\right),\tag{1.36}$$

where  $M_0$  is the initial disk mass and  $r_c$  is the characteristic radius. The dimensionless time variable T is defined as  $T = 1 + t/t_V$ , where  $t_V$  is the viscous timescale. This expression shows that  $\Sigma_g(r)$  approximately follows a power law of  $r^{-1}$  for  $r < r_c$ , and decreases exponentially for  $r > r_c$ . In terms of time evolution, Figure 1.9(b) illustrates that  $\Sigma_g(t)$  decreases with time while spreading outward.

The viscous disk evolution timescale (also called viscous timescale)  $t_V$  is given by

$$t_{V} = \frac{r_{c}^{2}}{3V} = \frac{r_{c}^{2}}{3\alpha c_{s}h_{g}}$$

$$\approx 0.87 \,\text{Myrs} \left(\frac{\alpha}{10^{-3}}\right)^{-1} \left(\frac{h/r}{0.1}\right)_{R=r_{c}}^{-2} \left(\frac{1M_{\odot}}{M_{\star}}\right)^{1/2} \left(\frac{r_{c}}{30 \,\text{au}}\right)^{3/2}$$
(1.37)

If we assume the disk viscous timescale is about 1-10 Myrs, then we can estimate

the disk viscosity  $\alpha$  about  $10^{-4}$  to  $10^{-2}$ .

The origin of viscosity in disks is still not well understood. The most widely accepted explanation is the magneto-rotational instability (MRI) (Balbus & Hawley, 1991), a small-scale instability that can generate turbulence in disks. MRI is driven by magnetic fields, which can amplify turbulence and enable angular momentum transport. However, MRI requires a sufficient level of ionization to operate effectively, which may not be present in all regions of protoplanetary disks.

As a result, other hydrodynamic instabilities, such as the vertical shear instability (VSI) (Nelson et al., 2013), was proposed to contribute to turbulence generation. VSI presents in disks where has vertical gradient of angular velocity and requires efficient cooling to become active. Lin & Youdin (2015) found that VSI can operate at a few to a few tens of au in disks, where cooling is efficient. Furthermore, using linear theory, Latter & Kunz (2022) showed that non-ideal MHD effects can enhance the growth of VSI.

Viscosity observations The level of viscosity in PPDs is still an open question. Recent measurements of the  $\alpha$  viscosity in disks tend to suggest a low value. There are several ways to measure the  $\alpha$  viscosity. First, by directly measureing the line broadening of the gas emission lines,  $\alpha$  viscosity can be inferred. Flaherty et al. (2015, 2018) suggested the  $\alpha$  viscosity in disks is a few  $10^{-4}$ . Second, indirect measurements based on the dust scale height can also be used. Villenave et al. (2022) found a very low  $\alpha$  value of  $10^{-5}$  by measuring the vertical scale height of the edge-on disk Oph 163131. Similarly, Pinte et al. (2016) inferred an  $\alpha$  of  $10^{-4}$  from the scale height of the HL Tau disk. Additionally, Dullemond et al. (2018) used the radial widths of gas structures as an indirect probe of  $\alpha$ .

However, some observations still suggest relatively high  $\alpha$  values. For example, Flaherty et al. (2020) estimated  $\alpha \sim 6 \times 10^{-2}$  in the DM Tau disk to account for nonthermal gas motion. To explain the presence of micron-sized grains in the surface layer of the HD 142527 disk, Tazaki et al. (2021) argued that strong turbulence with  $\alpha > 2 \times 10^{-3}$  is required.

#### **1.4.2 MHD** winds

Wind theory Besides the traditional viscous-driven accretion evolution model, an alternative is the magnetohydrodynamic (MHD) wind-driven evolution model (see the upper part of Figure 1.9). Unlike the internal angular momentum transport in the viscous model, the MHD wind model relies on magnetic fields to launch disk winds, which carry away angular momentum. As the disk loses angular momentum (transferred to the wind), it spins down and disk material accretes onto the star. Over time, this process leads to a shrinking disk size and decreasing disk mass (see Figure 1.9(c)).

Tabone et al. (2021a,b) extended the  $\alpha$ -framework from viscous disk model to describe MHD wind-driven accretion and showed that winds can cause a steeper decline in disk mass and accretion rate than viscous models. This MHD wind scenario offers a potential explanation for observed disk demographics.

Wind observations As wind-driven models gain attention, increasing efforts have been made to observe winds from PPDs. Regarding MHD winds, Booth et al. (2021) reported the detection of an MHD wind from the Class II disk HD 163296 using MAPS data. Fang et al. (2023) presented high-resolution spectral mapping of TW Hya using VLT, suggesting that [O I] emission traces the MHD wind.

#### 1.4.3 Disk size and mass

The evolution of disk size and mass can help distinguish between the viscous and MHD wind-driven evolution models. Recently, the ALMA Survey of Gas Evolution in Protoplanetary Disks (AGE-PRO) was proposed to systematically study the evolution of gas disk mass and size over the disk lifetime (0.1–10 Myr) for 30 protoplanetary disks. AGE-PRO aims to provide valuable insights into differentiating between the two disk evolution mechanisms. Below, we summarize measurements of disk size and mass reported in some literature.

**Disk size** Disk size is a key physical property of protoplanetary disks. Theoretically, disk size is defined as the radius enclosing a given fraction of the disk mass, while observationally, it is typically the radius enclosing a certain fraction of the total flux. Observations can measure disk sizes in both dust continuum and molecular

gas emission. Using the one of the most abundant molecules, CO, as a tracer, gas disk sizes have been measured in large samples (Ansdell et al., 2017; Barenfeld et al., 2017; Long et al., 2022).

The millimeter (mm) dust disk size,  $R_{\rm dust}$ , is often defined as the radius within which 95% of the total mm continuum flux is enclosed. For example, Huang et al. (2018) measured mm dust disk sizes ranging from 30 to 250 au in the DSHARP sample. Other notable studies of dust disk sizes include Andrews et al. (2018a) and Tazzari et al. (2021). Accurate measurement of disk size often requires detailed modeling of the visibility data, rather than relying solely on intensity maps or images. For instance, Ilee et al. (2022) used the visibility modeling code FRANK (Jennings et al., 2020) to analyze the TW Hya disk. They detected mm continuum emission extending to  $\sim$ 100 au, which was significantly beyond earlier estimates of 60–70 au.

**Disk mass** In a protoplanetary disk, the typical dust-to-gas mass ratio is 1%. Dust mass is important because it represents the total amount of solid material available for the formation of terrestrial planets and the cores of giant planets.

Using dust surface density  $\Sigma_d$ , the dust mass  $M_d$  is given by

$$M_d = \int_0^{2\pi} \int_0^{r_{out}} \Sigma_d(r) r dr d\phi = 2\pi \int_0^{r_{out}} \Sigma_d(r) r dr, \qquad (1.38)$$

where  $r_{out}$  is the outer radius of the disk.

Measurement of dust mass is usually conducted by dust continuum observations. For example, surveys of different star-forming regions, including Taurus, Lupus, Upper Scorpius, Chamaeleon I, and  $\sigma$  Orionis (Andrews et al., 2013; Ansdell et al., 2016; Barenfeld et al., 2016; Pascucci et al., 2016; Ansdell et al., 2018).

Gas mass is the dormant component of the disk mass and affects the disk dynamics and evolution. Though  $H_2$  is the main component of gas, it is difficult to observe directly. Therefore, gas mass is usually measured by other gas tracers including CO (Ansdell et al., 2016; Manara et al., 2020), HD (Bergin et al., 2013; Kama et al., 2020), and other tracers. Here are two detailed examples: Kama et al. (2020) constrain the upper limit of disk masses for 15 Herbig Ae/Be disks to  $0.1 \, M_{\odot}$ 

using archival HD 1–0 Herschel data, which rules out the gravitationally unstable possibility for these disks. Trapman et al. (2022) use astrochemical simulations to measure disk gas masses from  $N_2H^+$  and  $C^{18}O$  emissions. Gas mass could also be measured by dynamical methods, such as measuring self-gravity or "GI wiggles" of massive disks (Veronesi et al., 2021; Terry et al., 2021).

# 1.5 The Concertos: Planet-disk interactions

We know that planets are formed in protoplanetary disks. After introducing the orchestra (the disk), we now turn to the solo concertos—planet-disk interactions. The governing equations of planet-disk interactions are mostly the same as those for disks without planets. The key difference is that we need to include the gravitational potential of the planet.

Now, the gravitational potential  $\phi$  in Equation (1.3) from both star, planet and the indirect star-planet interaction is given by

$$\Phi = -\frac{GM_{\star}}{R} - \frac{GM_{p}}{\sqrt{|\mathbf{R} - \mathbf{R}_{p}|^{2} + (bh_{p})^{2}}} + \frac{GM_{p}}{R_{p}^{2}}R\cos\phi, \qquad (1.39)$$

where b is the smoothing factor for HD simulations, which is set to b = 0.6 (Masset, 2002).

In addition, for simplicity, we often assume a locally isothermal disk (see Equation 1.16), which is a common assumption in planet-disk interaction simulations. Under this assumption, the disk follows an isothermal equation of state, and the temperature is fixed and does not evolve with time.

The outcome of planet-disk interactions includes the formation of substructures in the disk, such as gaps, rings, and spirals. As a back reaction, the disk can also influence the planet's migration and growth. However, in this thesis, we will focus on the disk structures and will not discuss planetary migration and growth.

# 1.5.1 Gap opening by planets

Here, we briefly introduce the gap opening theory in a 2D  $(r, \phi)$  (no vertical dimension) isothermal disk using linear theory (Lin & Papaloizou, 1986). Note that

the gap structures discussed in this section refer to gas gaps. The depth of the gap opened by a planet is determined by the balance between the gravitational torque exerted by the planet (Lindblad torque) and the viscous torque from the disk. Below we provide a simplified order-of-magnitude estimate (Fung et al., 2014).

The Lindblad torque exerted by the planet onto the disk is

$$T_{\rm L} \sim q^2 \left(\frac{r}{h}\right)^3 \Sigma_{\rm gap} \Omega^2 r^4,$$
 (1.40)

where  $q \equiv M_p/M_{\star}$  is the planet-to-star mass ratio,  $\Omega$  is the Keplerian angular velocity, h is the disk scale height, and  $\Sigma_{\rm gap}$  is the surface density of the gap.

The viscous torque in the disk is given by

$$T_{\rm v} \sim v \Sigma_0 \Omega r^2,$$
 (1.41)

where v is the kinematic viscosity,  $\Sigma_0$  is the initial unperturbed surface density at the planet location.

If torques balance,  $T_L = T_v$  and plugging in  $r = r_p$ ,  $h = h_p$  gives the gap depth

$$\frac{\Sigma_{\rm gap}}{\Sigma_0} \sim \frac{\alpha (h_p/r_p)^5}{g^2}.$$
 (1.42)

When we plug in  $q=(h_p/r_p)^3$ , we find that the gap depth is  $\Sigma_{\rm gap}/\Sigma_0\sim \alpha(h_p/r_p)^{-1}$ . Assuming typical values of  $\alpha\sim 10^{-2}$  and  $h_p/r_p\sim 0.1$ , the gap depth is about 10% of the unperturbed surface density. So we can roughly say that the gap opening condition is the planet mass exceed the thermal mass  $M_p>M_{\rm th}=(h_p/r_p)^3M_{\star}$ . However, we should note that this is a very rough estimate. Actually when  $M_p>M_{\rm th}$ , nonlinear effects must be considered and the accurate form of the gap depth can deviates from the preditions of linear theory (Fung et al., 2014; Kanagawa et al., 2015).

Regarding the gap width, there is no simple analytical formula. Here we present the empirical formula from Kanagawa et al. (2015) instead. The gap width  $\Delta_{gap}$  is defined as the radial distance between the two locations where the gas sur-

face density is reduced to half of the unperturbed surface density.

$$\frac{\Delta_{\text{gap}}}{r_p} = 0.41 \left(\frac{M_p}{M_{\star}}\right)^{1/2} \left(\frac{h_p}{r_p}\right)^{-3/4} \alpha^{-1/4} = 0.41 K^{1/4}, \tag{1.43}$$

where  $r_p$  is the planet's orbital radius,  $h_p$  is the disk scale height at the planet's location, and K is the dimensionless parameter, defined as

$$K = \left(\frac{M_p}{M_{\star}}\right)^2 \left(\frac{h_p}{r_p}\right)^{-3} \alpha^{-1}. \tag{1.44}$$

The above equations show that the gap depth and gap width are determined by the planet mass q, the disk aspect ratio at planet locaiton  $h_p/r_p$ , and the disk viscosity  $\alpha$ .

Fung et al. (2014); Kanagawa et al. (2015, 2016); Duffell (2020) conducted a large number of 2D simulations and summarized empirical formulas for gap profiles (i.e., gap depth and width) as functions of planet mass, disk viscosity, and aspect ratio. Note that all of these studies assumed a locally isothermal equation of state. In addition to 2D models, 3D simulations have also been carried out to study planet-induced gap formation (Fung & Chiang, 2016). These studies show that the surface density profiles of gaps are broadly consistent with those in 2D simulations. However, 3D models also reveal large-scale meridional flows: gas is pushed outward from the planet's location in the midplane and returns inward at higher latitudes (Fung & Chiang, 2016). Interestingly, such meridional flows have been detected in observations of the HD 163296 disk and are suggested to be induced by embedded planets (Teague et al., 2019a).

Simulations of gap-opening via planet-disk interactions are often used to interpret observations. For instance, Dong et al. (2015); Dipierro et al. (2015) performed simulations and found that three embedded Saturn-mass planets could reproduce the annular gap structures observed in the HL Tau disk. Similarly, the gaps observed in the CI Tau disk may be explained by embedded Jovian-mass planets (Clarke et al., 2018). With the rapid advancement of machine learning, some studies now use these techniques to directly retrieve planet masses from observed dust contin-

uum gap structures (e.g., Auddy & Lin (2020); Auddy et al. (2021); Zhang et al. (2021b)).

Caveats of the Equation of State: The assumptions used in the disk's equation of state (EoS) can significantly influence gap properties by altering the propagation of density waves. For example, Miranda & Rafikov (2019, 2020) theoretically showed that locally isothermal and adiabatic assumptions can lead to different gap structures. Zhang & Zhu (2020) further demonstrated via simulations that the cooling timescale affects the gap profiles. Moreover, Zhang et al. (2023) extend the study of planetary-induced gap depth and width by including the effects of cooling in the energy equation.

#### 1.5.2 Spirals excited by planets

Spiral arms in protoplanetary disks can be generated by planet-disk interactions, with their morphology shaped by both planetary and disk properties. Bae & Zhu (2018a,b) showed that higher planet masses and hotter disks lead to fewer spiral arms, highlighting the role of dynamical and thermal conditions. In addition, the orbital eccentricity of planets can influences spiral morphology. Zhu & Zhang (2021) found that spirals driven by eccentric planets differ significantly from those produced by circular orbits.

The amplitude and observability of spirals depend on the disk's thermal structure, particularly the cooling timescale. Miranda & Rafikov (2020) and Zhang & Zhu (2020) demonstrated the sensitivity of spiral amplitude to cooling efficiency, while Speedie et al. (2022) showed that different cooling timescales produce distinct observable features. Muley et al. (2021) further examined local temperature rises within spirals.

# 1.5.3 Kinematic planetary signatures

Planets can perturb the velocity field of disks and cause kinematics substructure in gas observation. By analyzing kinematics signatures, we can indirectly detect protoplants and constrain the properties of planets.

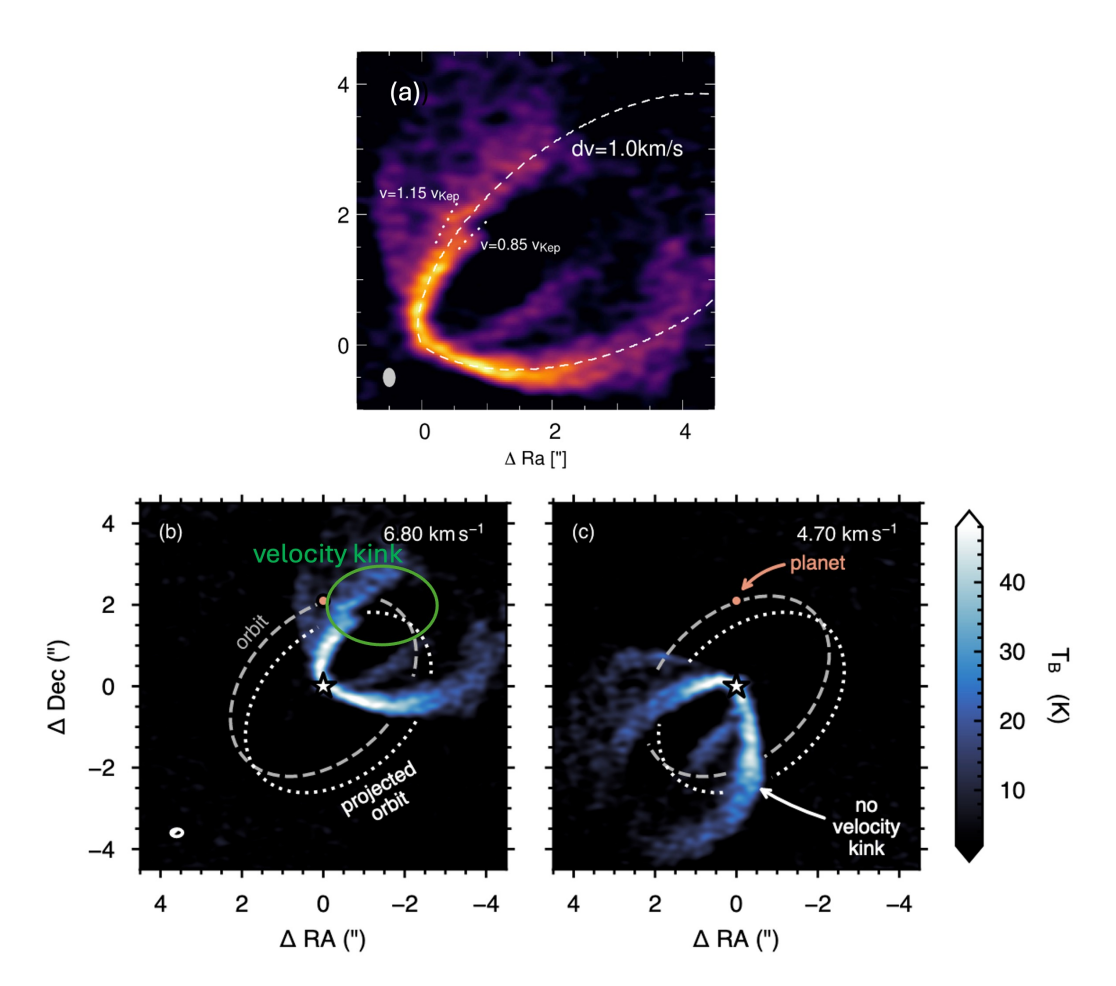


**Figure 1.10:** Schematic diagram of velocity kinks. Panel (a) shows how the emission feature (white dotted lines) deviates from the Keplerian isovelocity contours (white dashed line). Panel (b) displays the velocity kink in a channel map at a channel velocity of 6.8 km/s. The green circle highlights the kink. In panel (c), at another velocity channel, no kink is detected. In both panel (b) and (c), the orange dot marks the location of the planet in the midplane. The white dashed line represents the planet's orbit in the midplane, while the white dotted line indicates the projected orbit on the emission surface. Panel (a) is a close-up of panel (b). The figure is adapted from Pinte et al. (2018, 2022).

Kinematic theory For a Keplerian disk, if the disk geometry is known, the line-of-sight velocity  $V_{\text{LoS}}$  can be derived from the Keplerian velocity  $V_{\text{Kep}}$  at any position in the disk. This allows us to construct isovelocity contours of a Keplerian disk in synthetic channel maps. As shown in Figure 1.10(a), by comparing the observed emission features with the Keplerian isovelocity contours, one can identify "kink" features and quantify non-Keplerian deviations. In this case, the emission is no longer aligned with the isovelocity contours projected from  $V_{\text{Kep}}$ . Instead, the emission aligns with the contours corresponding to  $0.85V_{\text{Kep}}$  at smaller radii and  $1.15V_{\text{Kep}}$  at larger radii. Therefore, the velocity deviation  $\Delta v$  can be quantified as approximately  $0.15V_{\text{Kep}}$  in this example.

We summarize several relevant disk kinematics simulations. Perez et al. (2018) used 3D hydrodynamic simulations to demonstrate that deviations from Keplerian rotation induced by planets can be detected with ALMA gas observations. Rabago & Zhu (2021) used 3D hydrodynamic simulations to explore the relationship between velocity kink amplitude and planet mass. Calcino et al. (2022) showed, using SPH simulations, that secondary velocity kinks can trace the wake generated by embedded planets.

Kinematic observations Disk kinematics can also reveal signatures of embedded planets. Teague et al. (2018a) presented the kinematic detection of planets in the HD 163296 disk by precisely constraining the gas surface density profile. In the same disk, Alarcón et al. (2022) detected a localized kinematic structure in atomic carbon emission in the moment 1 map, spatially coincident with a previously proposed protoplanet. Izquierdo et al. (2021a) developed the DISCMINER code to robustly detect localized velocity perturbations, which are likely induced by two giant planets.

Recently, increasing numbers of velocity "kinks" have been detected. We show an example of a velocity kink detection in Figure 1.10(b), and a comparison case with no detected kink in Figure 1.10(c). Velocity kinks are localized perturbations in the disk's velocity field, appearing as lightning bolt-like features in specific velocity channels in channel map observations.

The first velocity kink was detected in the HD 163296 disk (Pinte et al., 2018), and was attributed to gas motion perturbed by a planetary spiral wake. Subsequent kink detections have been reported in the disks of HD 97048 and multiple disks in the DSHARP sample (Pinte et al., 2019, 2020), as well as in the IM Lupi disk (Verrios et al., 2022). Norfolk et al. (2022) confirmed that the kink and a spiral arm are spatially aligned in the HD 100546 disk. However, Speedie & Dong (2022) found that suggested gas spirals inferred from velocity kinks lack corresponding features in the dust continuum, suggesting that the interpretation of kinks as planetary-induced spirals remains uncertain and needs further investigation.

# 1.6 The soloist and conductor: Protoplanets and stars

#### 1.6.1 Protoplanets

A soloist is usually the superstar in a concerto; similarly, protoplanets are the focuses in observations of PPDs. Have we found any protoplanets in PPDs? The answer is yes. The most robust method to confirm that substructures in disks are caused by planet-disk interactions is the direct imaging of protoplanets. Despite significant efforts to search for planets in PPDs, only a few have been conclusively detected.

The most well-known case is the PDS 70 system. PDS 70 is a young star, approximately 5.4 Myr old (Müller et al., 2018), surrounded by a transition disk. Two confirmed protoplanets, PDS 70 b and PDS 70 c, have been detected in this disk (Keppler et al., 2018; Haffert et al., 2019). Their masses are estimated to be a few Jupiter masses (Wang et al., 2021), and they orbit at approximately 20 au and 34 au from the central star, respectively, which is close to a 1:2 orbital resonance. More recently, a third protoplanet candidate, PDS 70 d, located at around 13 au, has been suggested based on JWST observations (Christiaens et al., 2024).

PDS 70 b and PDS 70 c remain embedded in the circumstellar disk and continue to accrete material. This accretion can be traced via  $H\alpha$  emission, although the precise origin of this emission is still under debate. For example, Takasao et al.

(2021) used radiative hydrodynamic simulations to suggest that the H $\alpha$  emission from PDS 70 b may originate from the planetary surface rather than its circumplanetary disk (CPD). Zhou et al. (2021) imaged PDS 70 b in both UV and H $\alpha$ , providing further constraints on its accretion rate. Overall, mass accretion rates for PDS 70 b and PDS 70 c are estimated to lie between  $10^{-8}$  and  $10^{-6}$   $M_{\odot}$  yr<sup>-1</sup> (Haffert et al., 2019; Hashimoto et al., 2020).

PDS 70 c is a particularly interesting object for studying accretion processes and CPD evolution. From 2020 to 2024, both HST and ground-based observations have revealed strong variability in its H $\alpha$  flux, suggesting a dynamic accretion process (Zhou et al., 2025). A CPD around PDS 70 c has been detected by ALMA, with an estimated dust mass of about 0.01  $M_{\oplus}$  (Benisty et al., 2021). Portilla-Revelo et al. (2021) conducted radiative transfer modeling to study the structure of this disk in more detail. These observations provide critical insights into the formation and accretion of giant planets.

In addition to CPDs embedded within PPDs, circumplanetary disks have also been detected around free-floating planetary-mass objects (PMOs) or planetary-mass companions (PMCs) orbiting binary stars. These disks are often referred to as circum-PMO disks (CPMODs). Notable examples include SR 12 c and DH Tau b, where CPMODs have been identified with ALMA (Wu et al., 2022).

We can place confirmed protoplanets and protoplanet candidates—those inferred from disk substructures—on the same diagram as confirmed exoplanets to better understand the current detection limits for protoplanets. Figure 1.11 presents a diagram of planet mass versus semi-major axis for confirmed exoplanets and Solar System planets. Additionally, inferred embedded protoplanets in disks are also indicated. In the ALMA era, these protoplanets or candidates typically appear to be an order of magnitude more massive and located 1–3 orders of magnitude farther from their host stars than confirmed exoplanets.

Most of these protoplanet candidates lie beyond the current detection limits of exoplanet surveys, underscoring the difficulty of directly detecting protoplanets with existing instruments. However, in the exciting near future, with the advent of next-generation facilities such as the Extremely Large Telescopes (ELTs) and the Next Generation Very Large Array (ngVLA), it will become possible to detect protoplanets with properties comparable to sub-Neptune or super-Earth planets (Chen & Szulágyi, 2021; Krieger & Wolf, 2022).

#### 1.6.2 Star-disk interactions

As stars are not the main focus of this thesis, we only briefly introduce their effects on disk properties. Like a conductor directs an orchestra, the host star plays a crucial role in shaping the structure and evolution of the protoplanetary disk. For instance, stellar accretion stages and stellar multiplicity can have significant impacts on the morphology and dynamics of the disk.

Since most stars form in binary or multiple systems, disks in these environments often exhibit complex and intriguing structures. Bi et al. (2020) present ALMA 1.3 mm observations of a circumtriple disk around GW Ori, showing misaligned and eccentric features that point to strong star-disk interactions. Similarly, Martin et al. (2022) investigate a circumbinary disk (CBD) in HD 98800, where the influence of an outer stellar companion induces polar alignment of the CBD. Stellar accretion activity can also impact disk properties. For example, Vorobyov et al. (2021) demonstrate that FU Ori-type accretion bursts can alter the dust size distribution and shift the locations of icelines within the disk, thereby affecting conditions for planet formation.

#### 1.7 Outline of this thesis

The main goal of this thesis is to study the interactions between planets and disks, with a focus on the impact of planets on disk thermal structure and kinematic signatures. We aim to understand how these interactions can be used to interpret disk composition and exoplanetary atmosphere, as well as to hunt for young planets in disk kinematic observations. Similar to there being three movements in a typical concerto, this thesis also includes three main chapters from my work during my PhD period.

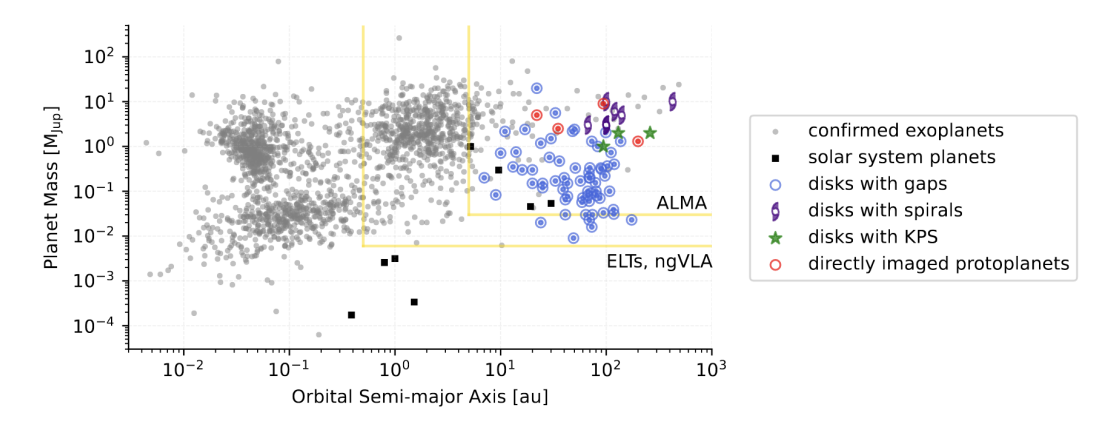


**Figure 1.11:** Diagram of planet mass and semi-major axis of confirmed exoplanets and embedded protoplanets. The properties of protoplanets are inferred from gaps, spirals, or kinematic planetary signatures (KPS) or confirmed by direct imaging. This diagram is from Bae et al. (2022).

**Chapter 2** presents a novel iterative model integrating hydrodynamic and radiative transfer simulations to assess the impact of giant planets on disk temperature, ice distribution, and C/O ratio. We find that a giant planet can significantly alter the disk temperature, complicate the ice line locations, and affect the C/O ratio.

Chapter 3 further extends the study of planet feedback on disk thermal structure by implementing multiple dust species into the iterative model in Chapter 2. We find that the implementation of multiple dust species does not significantly affect the disk temperature and midplane iceline locations. In addition, we explore the effects of different viscosity and do not find a simple correlation between viscosity and temperature of disk substructure.

**Chapter 4** conducted 3D hydrodynamic simulations to study velocity perturbations during planet-disk interactions, followed by radiative transfer post-processing to examine kinematic signatures in synthetic images. For the first time in disk kinematics simulations, we propose using residual velocity and channel maps—created by subtracting an azimuthally averaged background—to reveal planet-induced velocity perturbations. We also provide a guide for the choice of simulation parameters, including the duration and numerical resolution of simulations.

**Chapter 5** summarizes the main findings of this thesis and their impact on a broader framework of planet formation and disk evolution. We also discuss the potential

implications of our findings for future research directions.

# Chapter 2

# Planet Gap-opening Feedback on Disk Thermal Structure and Composition

# **Abstract**

(Exo-)planets inherit their budget of chemical elements from a protoplanetary disk. The disk temperature determines the phase of each chemical species, which sets the composition of solids and gas available for planet formation. We investigate how gap structures, which are widely seen by recent disk observations, alter the thermal and chemical structure of a disk. Planet-disk interaction is a leading hypothesis of gap formation and so such changes could present a feedback that planets have on planet-forming material. Both the planet gap-opening process and the disk thermal structure are well studied individually, but how the gap-opening process affects disk thermal structure evolution remains an open question. We develop a new modelling method by iterating hydrodynamical and radiative transfer simulations to explore the gap-opening feedback on disk thermal structure. We carry out parameter studies by considering different planet locations  $r_p$  and planet masses  $M_p$ . We find that for the same  $r_p$  and  $M_p$ , our iteration method predicts a wider and deeper gap than the non-iteration method. We also find that the inner disk and gap temperature from the iteration method can vary strongly from the non-iteration or disk without planets, which can further influence dust-trap conditions, iceline locations, and distribution of various ices, such as H<sub>2</sub>O, CO<sub>2</sub>, and CO on large dust grains ("pebbles"). Through that, a gap-opening planet can complicate the canonical picture of the non-planet disk C/O ratio and influence the composition of the next generation of planetesimals and planets.

# 2.1 Introduction

Chemical element abundance ratios in planets, and in comets or asteroids, are determined by the chemical composition and physical-chemical evolution of the protoplanetary disk they form in. The study of chemical element abundance ratios such as C/O (Öberg et al., 2011; Madhusudhan et al., 2014) or N/S (Turrini et al., 2021) may allow to connect planetary bodies to their formation history, which is important for understanding how the chemical diversity of planetary systems arises. The distribution of volatile chemical elements in the solid (dust, ice) and gas phases is set by the location of their icelines, which depend on the disk temperature structure. In this work, we employ hydrodynamical and radiative transfer models to study the feedback of planet-induced gaps on the temperature structure and hence the location of icelines.

ALMA observations have revealed that rings and gaps in the dust and gas components are common in protoplanetary disks (e.g., Andrews et al., 2018b; Öberg et al., 2021). One possible and intriguing explanation for the formation of such substructures is embedded young planets in disks. Despite great efforts, very few protoplanets have been detected in disks by direct imaging (Keppler et al., 2018, 2019; Haffert et al., 2019; Benisty et al., 2021; Currie et al., 2022; Hammond et al., 2023). Direct imaging is, however, biased towards super-Jupiter mass protoplanets, whereas most gaps may be due to lower-mass giant planets. Their masses can be inferred from the gap structure or gas kinematics (e.g., Zhang et al., 2018; Teague et al., 2018a). Alternative scenarios to explain gaps and rings without planets have also been proposed, such as secular gravitational instabilities (Takahashi & Inutsuka, 2014), dust evolution (Birnstiel et al., 2015), zonal flows (Flock et al., 2015), and icelines (Zhang et al., 2015).

A gap in the disk implies a reduced optical depth in a radially confined region. This allows shorter wavelength photons to penetrate deeper and heat the disk midplane, as well as the edges of the gap, so gaps potentially affect the disk temperature structure. An opposite, cooling effect may result from fewer photons being scattered by dust towards the midplane. The balance of these effects around a given

dust gap can be studied with Monte Carlo radiative transfer (RT) models (Broome et al., 2023). Previous studies of temperature changes around gaps used analytically prescribed surface density profiles: Cleeves et al. (2015) explored the spatial distribution of molecular abundances resulting from increased heating due to an accreting protoplanet in a gap, while Broome et al. (2023) used Monte Carlo radiative transfer to investigate the dust temperature structure around analytical gap profiles in a hydrostatic 1+1D disk model.

The temperature change caused by a gap can also affect the structure of the gap itself. Hydrodynamical (HD) simulations of planet-disk interactions and gap-opening processes assuming a locally isothermal equation of state (EoS) provide empirical formulas of gap depth and width (Fung et al., 2014; Kanagawa et al., 2015, 2016; Zhang et al., 2018; Duffell, 2020). Recently, Miranda & Rafikov (2019, 2020) suggest that the assumptions of the equation of state, locally isothermal or adiabatic assumptions, can affect the gap properties by altering the propagation of density waves. Additionally, Zhang & Zhu (2020) used simulations to show that the cooling timescale can influence the gap profile.

Disk thermodynamics plays an important role in setting the location of different icelines in disks. An iceline of a specific molecule is the location where the temperature is low enough so that such molecules freeze out from the gas phase onto dust grains. Though direct measurements of the location of molecular icelines are rare in observations (e.g., water iceline van 't Hoff et al. (2018), CO iceline Zhang et al. (2017); van 't Hoff et al. (2017)), icelines can play an important role in planet formation. Across icelines, the gas composition and ice reservoirs for the planet and planetesimal formation are changed (e.g., Öberg et al., 2011), and the efficiency of planetesimal formation can increase at the water iceline (e.g., Stevenson & Lunine, 1988; Schoonenberg & Ormel, 2017). In addition, dust trapping is closely related to the planet gap-opening process, which in combination with the location of icelines determine the location of planetesimal formation and their composition. Dust trapping in local pressure maxima is proposed to overcome rapid dust loss due to radial drift by the drag between the gas and the dust in disks Whipple (1972). For

example, Pinilla et al. (2012a) demonstrated that the pressure bump outside the gaps opened by planets can trap dust and produced ring-like structures as observed

Conventionally, previous studies on gap modeling or thermal structures in disks only conduct HD or RT simulations, or combine the final results from HD to RT simulations to compare with observations. However, as planets open gaps in disks, the temperature around gaps could deviate significantly from the temperature adopted for disks without planets. In the meantime, the temperature changes affect the disk gas scale height H and volume density  $\rho$  distribution.

In this paper, we build a new model to investigate the planet gap-opening process and the gap-opening feedback on disk thermal structure. Because the temperature controls which species can exist as solid ices, our model allows us to investigate the question: what is the feedback effect of giant planets on the composition of material subsequently accreted by the planets themselves, or by a new generation of forming planetesimals?

In order to improve previous models, we first feed HD simulations with a more physical energy field from RT models. During the planet gap-opening process, we combine the HD and RT simulations together and iterate them. We implement the new temperature calculated by RT to correct the energy field of HD simulations.

This paper is organized as follows. In Section 2.2 we describe our modeling method of how we iterate the hydrodynamical and radiative transfer simulations to study the gap-opening process. In Section 2.3, we present and quantify our modeling results of gap properties, disk temperature structure, and ice distributions. Section 2.4 discusses the impact of our results on disk composition, disk substructure observation, and the limits of our models. Section 2.5 summarizes the main conclusions of this paper.

# 2.2 Methods

In this section, we describe the codes and setup of our hydrodynamical and radiative transfer simulations, as well as the workflow of how we iterate these two simulations to study the temperature structure of a disk with a gap-opening planet.

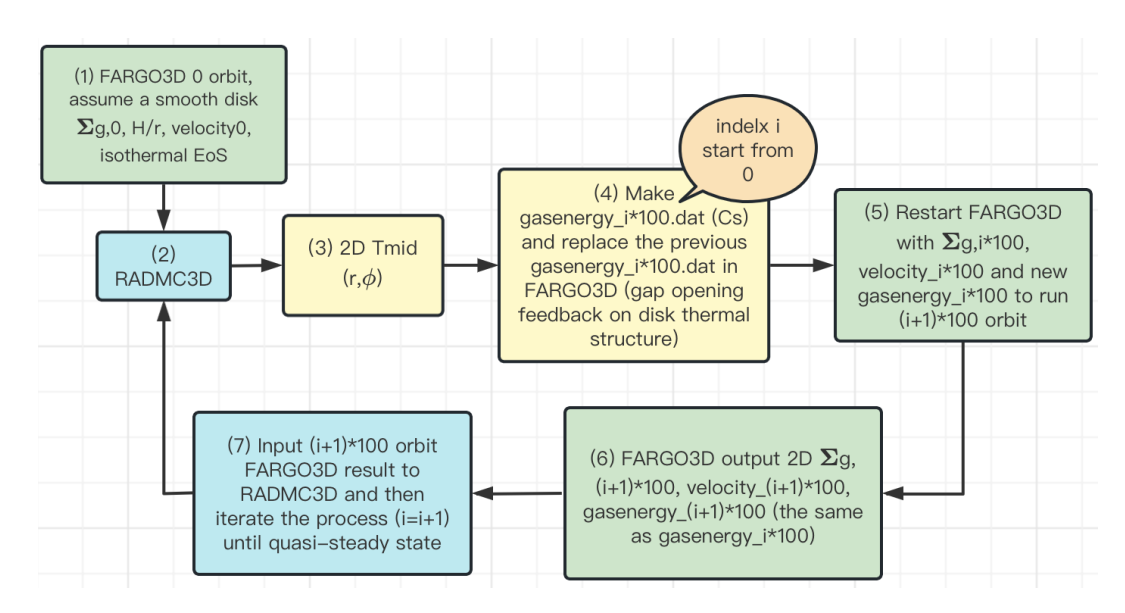


**Figure 2.1:** The workflow of the iteration method. The green, blue, and yellow boxes represent the steps of FARGO3D, RADMC3D, and post-processing between RADMC3D and FARGO3D, respectively. The iteration step is 100 planet orbits.

#### 2.2.1 Hydrodynamical simulations

We conduct 2D hydrodynamical simulations in polar coordinate  $(r, \phi)$  to study surface density evolution with FARGO3D (Benítez-Llambay & Masset, 2016). The main parameters of FARGO3D simulations are shown in Table 3.1.

For grid setup, we conduct global disk simulations of a transition disk which extend from  $r_{min} = 1$  au to  $r_{max} = 100$  au. The global disk simulations for FARGO3D avoid the radial extrapolation of the sound speed  $c_s$  setups for global disk RADMC3D simulations. Such consideration is necessary, as the extrapolation could be imprecise for a radially non-smooth  $c_s$  field. We set up mesh grids linearly distributed in  $\phi$  direction, and logarithmically distributed in r direction. The grid numbers  $(N_{r,HD}, N_{\phi,HD})$  resolve the gas scale height at the location of the planet with at least 5 grid cells and make the grid cells square shape at the planet location. We also do convergence tests by doubling the resolution, finding that the gap depth variations are less than 20%. So we keep on using the resolution in Table 3.1 to minimize simulation time during each iteration step.

Regarding the physical model setup, we only include gas in our simulations without dust and the radial initial gas density profile is  $\Sigma_g = \Sigma_0 (r/r_0)^{-1}$ . We assume

**Table 2.1:** FARGO3D main parameters. Parameters in each column below the second row in this table are corresponding to the cases of planet location  $r_p = 4$ , 10, or 30 au, respectively.

parameters	values		
$M_p$	$3M_{\rm J}, 1M_{\rm J}, 100M_{\oplus}, 10M_{\oplus}$		
$\alpha$	0.001		
$r_0 = r_p$ [au]	4	10	30
$r_{min} [r_0]$	0.25	0.1	0.033
$r_{max} [r_0]$	25	10	3.3
AspectRatio	0.04	0.05	0.066
$\Sigma_0[M_{\star}/r_0^2]$	$1.8^{-4}$	$4.5^{-4}$	$1.34^{-3}$
$N_{r,HD}$	580	460	350
$N_{\phi,HD}$	790	630	480

the whole disk mass is  $0.028M_{\odot}$ , which is a normal choice for solar-mass star (e.g., see review in Manara et al., 2022). The EoS is assumed locally isothermal and the flared disk is built with aspect ratio  $h/r \propto r^{1/4}$ . However, since we update  $c_s$  for each iteration step as described in section 2.2.3, we only use aspect ratios and flaring index as the initial conditions but do not need to use them at any later step of evolution. We adopt a Shakura & Sunyaev (1973) viscosity parameter  $\alpha = 10^{-3}$ . We use the scale-free parameter setup in FARGO3D which means G,  $M_{\star}$ ,  $r_0 = 1$ . Here we set  $r_0 = r_p$  and fix planets at circular orbits. The indirect term of potential is included in the simulations. The planets are introduced into disks from the beginning of the simulations without including any accretion onto the planets. We also examine introducing planets into a disk with a mass-taper function but find no significant difference in the results.

At the radial boundaries, we adopt power-law extrapolation densities and Keplerian extrapolation azimuthal velocities at both  $r_{\min}$  and  $r_{\max}$ . In terms of radial velocities, we adopt an outflow inner boundary and a symmetric outer boundary. Periodic boundaries are imposed in the azimuthal direction.

#### 2.2.2 Radiative transfer simulations

After obtaining the 2D  $\Sigma_g$  and  $c_s$  fields from FARGO3D simulations, we perform 3D Monte Carlo radiative transfer with RADMC3D (Dullemond et al., 2012) to obtain the temperature structure. The output gas temperature  $T_{gas}$  is used to update

the corresponding  $c_s$  field for FARGO3D (see Section 2.2.3). Within RADMC3D simulations, all parameters are in units of cgs and the main parameters are shown in Table 3.2.

For grid cell setup, RADMC3D keeps the same global transition disk simulation domain in  $(r, \phi)$  direction as FARGO3D. The vertical domain is  $\theta = [\pi/2 - 0.5, \pi/2]$  with mirror symmetry along the midplane. The azimuthal and vertical directions are sampled in linear space, while the radial direction is sampled in logarithmic space. We test different combinations of grid resolutions and decide  $(N_{r,RT}, N_{\phi,RT}, N_{\theta,RT}, N_{\theta,RT} = (256, 30, 53)$  in radial, vertical, and azimuthal direction is a proper resolution for using  $N_{\text{photon}} = 10^8$  photon packages. For small  $N_r, N_{\phi}$ , the asymmetry temperature feature in disks due to eccentric gaps is not recovered properly. For larger  $N_r, N_{\phi}$ , the  $T_{mid}$  map gets bad photon statistics and it is noisy unless we adopt a larger number of photons  $N_{\text{photon}} > 10^9$ , which takes more than 10 hours with paralleling 40 threads for just one iteration step. Also,  $N_{\text{photon}} = 10^8$  gets similar smooth temperature results as  $N_{\text{photon}} > 10^9$  with more grid cells. Hence, we keep  $N_{\text{photon}} = 10^8$  for all the simulations presented in this paper. After RADMC3D, we interpolate the values in RADMC3D grid cells to match the  $(r, \phi)$  grid cells in FARGO3D.

For the stellar parameters, we adopt typical values for a T Tauri star,  $M_{\star}=1M_{\odot}$ ,  $R_{\star}=1.7R_{\odot}$ , and  $T_{\star}=4730$ K. We only consider stellar radiation as the heating source and ignore viscous heating. We assume silicate dust particles with isotropic scattering and the intrinsic density is  $3.710\,\mathrm{g\,cm^{-3}}$ . We also assume dust to gas mass ratio  $\varepsilon=0.01$  and dust grain size of  $0.1\mu m$ . As the small dust grains couple well to the gas, we do not assume any dust settling. Also, we do not consider any dust evolution process, such as dynamics, growth, or fragmentation of particles (Birnstiel et al., 2010). The disk density distribution in three dimensions is assumed to be

$$\rho_d(r, z, \phi) = \frac{\Sigma_d(r, \phi)}{\sqrt{2\pi}H(r)} \exp\left(-\frac{z^2}{2H(r)^2}\right)$$
 (2.1)

where  $\Sigma_d(r,\phi)$  is the dust surface density and  $\Sigma_d(r,\phi) = \varepsilon \Sigma_g(r,\phi)$ . H(r) is the gas pressure scale height and  $z = r \tan \theta$ .

**Table 2.2:** RADMC3D parameters.

parameters	values
$M_{\star}$ $[M_{\odot}]$	1
$R_{\star}$ [ $R_{\odot}$ ]	1.7
$T_{\star}$ [K]	4730
$N_{photon}$	$10^{8}$
ε	0.01
$N_{r,RT}$	256
$N_{\phi,RT}$	30
$N_{m{ heta},RT}$	53

#### 2.2.3 Workflow

Our iterative approach makes use of FARGO3D and RADMC3D codes. The work-flow of our iteration method is illustrated in Figure 2.1. The green, blue, and yellow boxes represent the steps of FARGO3D, RADMC3D, and post-processing from RADMC3D to FARGO3D, respectively. Our methodology consists of the following steps:

**Step 1:** We set up our initial physical disk models without planets by assuming azimuthal symmetric 1D gas surface density  $\Sigma_{g,0}(r)$  and aspect ratio h/r of the disks (shown in Box(1)). Then, we output FARGO3D results of 0 orbit to obtain initial 2D  $\Sigma_{g,0}(r,\phi)$  and sound speed  $c_{s,0}(r,\phi)$  map. Note that the energy field outputs in FARGO3D simulations in this paper are actually the isothermal  $c_s$ .

**Step 2:** 2D surface density field from FARGO3D are read by RADMC3D and extend to 3D volume density by following Eq. 2.1, where the scale height H is calculated from FARGO3D  $c_s$  field. Then the dust radiative transfer simulations are conducted (Box (2)), and the output of the dust temperature  $T_{dust}(r,\theta,\phi)$  is obtained. As RADMC3D does not include any photochemistry simulations, we assume  $T_{gas}(r,\theta,\phi)) = T_{dust}(r,\theta,\phi)$ . From  $T_{dust}(r,\theta,\phi)$ , the midplane temperature  $T_{mid}(r,\phi)$  can be obtained (Box (3)). Using this RADMC3D temperature as the non-planet disk temperature can help us to get rid of the initial temperature profile assumption in FARGO3D. In fact, such a step is also done in Fig. 6(a) in Bae et al. (2019) to get the first Monte Carlo radiative transfer (MCRT) temperature, which aims to get rid of the assumed stellar irradiation-dominated temperature  $T_{irr}$ . We

also test the iteration process (assuming vertical hydrostatic equilibrium) described in Appendix A in Bae et al. (2019) to get the multiple iteration MCRT temperature but the differences between the first MCRT temperature and multi-time MCRT temperature in our disk model are negligible. This MCRT iteration process makes no difference in our case but at least doubles our MCRT workload and costs much more computation time. So we directly use our RADMC3D temperature for later steps.

**Step 3:** By using the  $T_{mid}(\mathbf{r}, \phi)$  from the last step, we could infer a new  $c_s$ field by assuming a vertical isothermal approximation. Even though we still use the isothermal assumption here, because of the non-smooth  $T_{mid}(\mathbf{r}, \phi)$  reflecting the gap-opening process, such new  $c_s$  does not equal the initial isothermal  $c_{s,0}$  anymore. The new  $c_s$  is treated as the new gasenergy.dat file for the next FARGO3D run (Box (4)). This is the important step that moves beyond the isothermal assumption in the conventional non-iteration method and shows the feedback effect of the gapopening process. In Appendix 2.6.2, we have a test to compare a vertical density weighted temperature with  $T_{mid}$ . We find that they are similar, especially in gap regions. For simplicity, we use  $T_{mid}$  in this paper. Next, we restart the FARGO3D simulation and evolve it over 100 orbital times (we assume the iteration step is 100 orbit here) (Box(5)) and as a result, we get the output as Box(6). Again, during the FARGO3D step, the EoS is assumed isothermal. Malygin et al. (2017); Pfeil & Klahr (2019) demonstrate that the thermal relaxation time varies across the disk, and in some regions, there is large cooling time (>100 local orbits), where our iteration time is a good approximation. However, in some outer disk regions, like a few tens of au, (the specific regions depend on the model conditions) have short cooling time, where our choice of 100 orbits can be too long. As a test, we performed simulations with iteration steps of 50 orbits in Appendix 2.6.1, and found no difference with the 100 orbits case. We also test iteration step of 100 orbits against 500 orbits in Appendix 2.6.1, which do not converge very well in gap regions. It means the iteration step of 500 orbits could not replace 100 orbits. For these reasons, we keep 100 orbits for all the main simulations of this work.

**Step 4:** The result of 100 orbit FARGO3D is used as the input for RADMC3D (Box(7)). During the RADMC3D setup, the gas pressure scale height H is given by the FARGO3D  $c_s$ ,  $H = c_s/\Omega$ . Therefore, the extension of 2D  $\Sigma_g$  to 3D volume density  $\rho$  (shown as Equation 2.1) can be also modified by the gap-opening feedback.

**Step 5:** Repeat Step 2 to Step 4 and iterate until reaching a quasi-steady state, which also means the iteration process is from Box(2) to Box(7). We iterate all the simulations over 2000 planet orbital time which corresponds to  $1.6 \times 10^4$  yrs for  $r_p = 4$  au,  $6.4 \times 10^4$  yrs for  $r_p = 10$  au,  $3.3 \times 10^5$  yrs for  $r_p = 30$  au, respectively.

In summary, there is density and velocity evolution but no energy/ $c_s$  evolution over time in HD simulations, while the energy/ $c_s$  field is evolved by executing RT simulations. Meanwhile, the evolving  $c_s$  field contains the information from the gap-opening feedback. As a comparison, in this paper, the conventional non-iteration method is running FARGO3D then RADMC3D simulation once. To be more specific, non-iteration uses FARGO3D with the physical assumptions (initial isothermal  $c_s$ ) in Box(1) to obtain  $\Sigma_g$ . Then input this  $\Sigma_g$  into RADMC3D to get the temperature  $T_{mid}$ . The whole process is finished after doing this once.

# 2.3 Results

In this section, we describe the results of our simulations, and compare the results between the iteration and non-iteration methods.

# 2.3.1 Gas surface density

Based on Step 3 in the iteration workflow described in section 2.2.3, we can obtain the surface density in disks. From left to right columns, Figure 2.2 shows the 2D gas surface density maps of gaps opened by planets at 2000 orbits in masses of  $3M_{\rm J}$ ,  $1M_{\rm J}$ ,  $100M_{\oplus}$ , and  $10M_{\oplus}$  at orbital radii of 4 au. The iteration and non-iteration results are presented in upper and lower panels, respectively. The gaps from the iteration method are generally deeper and wider than their counterparts simulated by the non-iteration method.

As gap structures are shown in most simulations, we quantify the gap width and

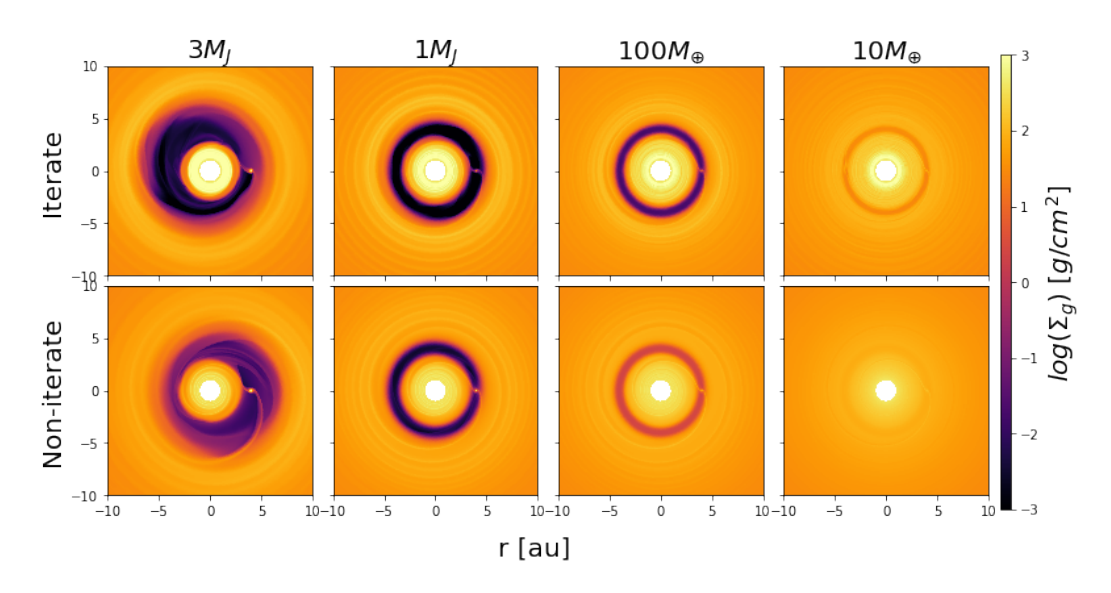


**Figure 2.2:** 2D gas density map of planets at fixed radius of 4 au over 2000 orbits of iteration method (upper panels) and non-iteration method (lower panels). From left to right columns, gaps are opened by planets of  $3M_{\rm J}$ ,  $1M_{\rm J}$ ,  $100M_{\oplus}$ , and  $10M_{\oplus}$ , respectively.

depth from the data of surface density and compare iteration with the non-iteration models. In this work, we define the gap width  $\Delta_{\rm gap}$  with the method in Kanagawa et al. (2016) which is the radial region where  $\Sigma_{\rm gap}/\Sigma_0 \leq 0.5$ . Meanwhile, we define the gap depth  $\Sigma_{\rm gap}/\Sigma_0$  as that in Fung et al. (2014) which is the radial averaging value within  $2 \times max(R_{\rm H}, H)$  of the planet, where  $R_{\rm H}$  and H are hill radius and scale height at  $r_{\rm p}$ . Both the gap width and gap depth are obtained by azimuthal averaging and the last 500-orbit averaging.

Figure 2.3 displays the comparison of the normalized gap width  $\Delta_{\rm gap}/r_{\rm p}$  (green) and gap depth  $\Sigma_{\rm gap}/\Sigma_0$  (blue) as a function of  $M_p$  of iteration (dashed lines) and non-iteration (solid lines) methods. From top to bottom panels,  $r_{\rm p}=4$ , 10, and 30 au, respectively. Uncertainty of gap depths and widths are also shown, which come from time averaging of the last 500 orbits. The choice of final 500 orbits is because our simulations appear to reach quasi-steady states at around 1500 orbits though gap depth and gap eccentricity are still slightly fluctuating. Under the definition of gap width and gap depth here,  $M_p=10M_{\oplus}$  cannot open gaps except for  $r_{\rm p}=4$  au of iteration. With regard to the  $\Sigma_{\rm gap}/\Sigma_0$  of non-iteration method, we find them consistent with the empirical formulas in Fung et al. (2014) except the ec-

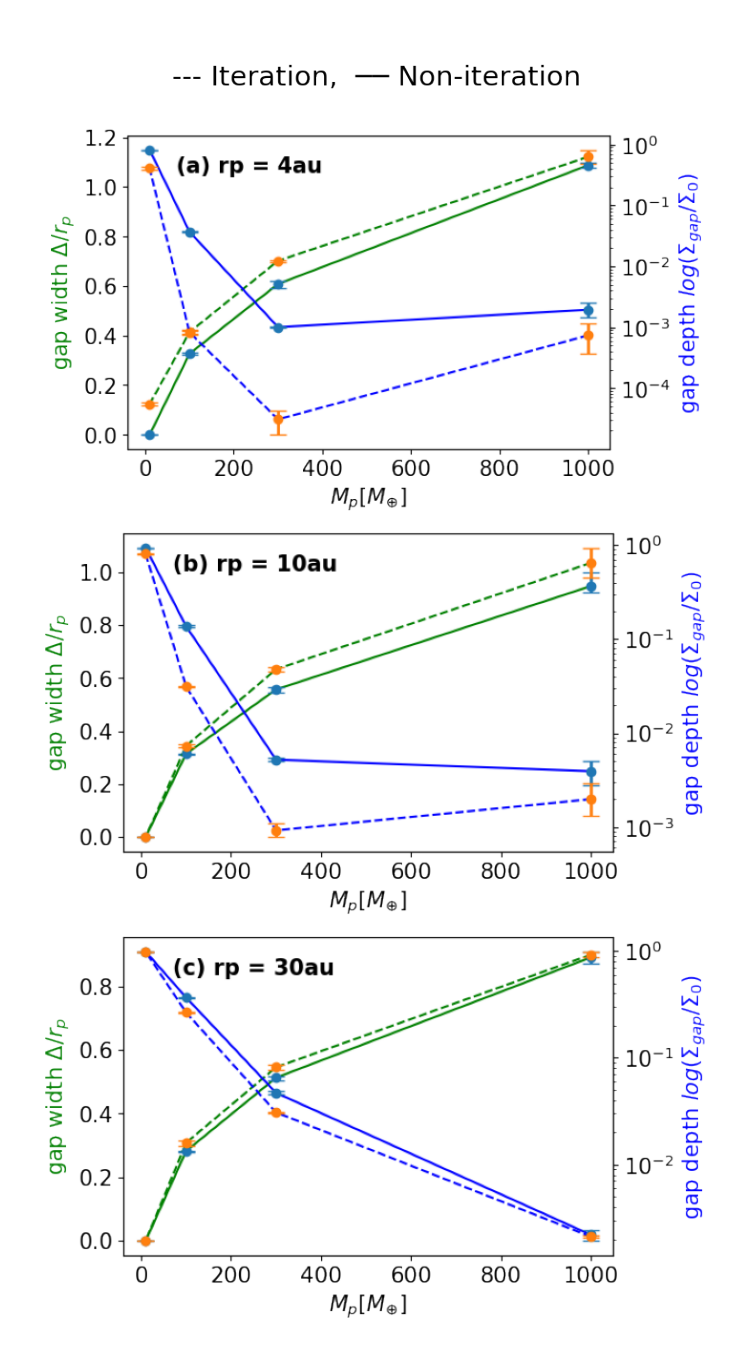


**Figure 2.3:** Normalized gap widths  $\Delta_{\rm gap}/r_{\rm p}$  (green) and depths  $\Sigma_{\rm gap}/\Sigma_0$  (blue) and their uncertainties (error bars) as a function of  $M_p$  at  $r_{\rm p}=4$  (panel (a)), 10 (panel (b)), and 30 au (panel (c)), respectively. Dashed and solid lines represent the iteration and non-iteration results.

centric case caused by  $M_p=3M_{\rm J}$ . In general, the iteration method infers a slightly wider gap width  $\Delta_{\rm gap}$  than the non-iteration method, whereas iteration predicts an order of magnitude deeper gap depth  $\Sigma_{\rm gap}/\Sigma_0$  than non-iteration. The reason for the deeper gap in iteration is the aspect ratio h/r at the gap region is smaller than the non-iteration. Based on equation 3 in Fung et al. (2014), a lower h/r lead to a smaller  $\Sigma_{\rm gap}$ . As the iteration method predicts a deeper gap than the non-iteration method, which means a lower mass planet can possibly open a deep gap. For instance, in Figure 2.3(a), when  $r_{\rm p}=4$ au, the iteration predicts that a Saturn mass planet can open a gap as deep as a Jupiter mass planet in the non-iteration method. This can help to explain why massive planets predicted by usual non-iteration simulations are supposed to be observable but have not actually been widely detected in real observations.

Among the gap depth of the iteration method, as  $M_p$  increases,  $\Sigma_{\rm gap}/\Sigma_0$  decreases, though this trend is invalidated to  $M_p=3M_{\rm J}$  at  $r_{\rm p}=4$  or 10 au. In these two cases, planets open appreciable eccentric gaps and streamer structures appear, which increases gas density in gaps. Similar situations also happen in the non-iteration cases, though the streamers are less strong and the measured  $\Sigma_{\rm gap}/\Sigma_0$  are close for  $M_p=1M_{\rm J}$  and  $3M_{\rm J}$ . In terms of gap width  $\Delta_{\rm gap}$ , as  $M_p$  increases,  $\Delta_{\rm gap}$  increases. For  $M_p=3M_{\rm J}$ , it can open a gap roughly as wide as the planet orbit  $r_{\rm p}$  in our disk models. For a fixed  $M_p$ , if  $r_{\rm p}$  increases, the normalized gap width  $\Delta_{\rm gap}/r_{\rm p}$  is smaller and the gap depth  $\Sigma_{\rm gap}/\Sigma_0$  is shallower. This is because the higher disk scale height h/r in the outer disk makes pressure torque stronger to prevent the gap opening process. Besides the disk density profiles of planets at 4 au, Fig. 2.12 and 2.13 in Appendix show the 2D gas surface density map of planets at 10 au and 30 au. As planets move further away from the central stars, they open shallower gaps than their counterparts at 4 au.

## 2.3.2 Midplane temperature

After implementing dust radiative transfer (described in Step 2 in section 2.2.3) and assuming  $T_{gas} = T_{dust}$ , we get the 3D  $T_{gas}$  structure of disks. As we are concerned about icy-pebbles or planetesimals which mainly concentrate at the disk

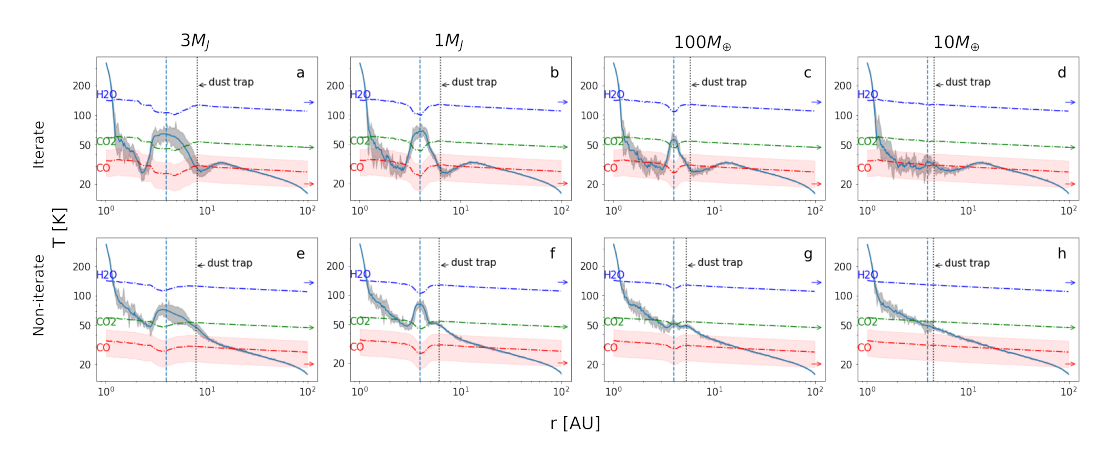


**Figure 2.4:** Midplane temperature  $T_{mid}$  as a function of disk radius from RADMC3D simulations of planets at 4 au over 2000 orbits of iteration method (upper panels) and non-iteration method (lower panels). The cyan solid lines represent the azimuthal averaged  $T_{mid}$ , while the shading areas represent the deviation of the profiles along different azimuthal angles. From left to right, there are results of  $3M_{\rm J}$ ,  $1M_{\rm J}$ ,  $100M_{\oplus}$ , and  $10M_{\oplus}$ , respectively. The blue, green, and red dash-dotted lines near the horizontal direction represent the pressure-dependent sublimation temperature  $T_{evap,H_2O}$   $T_{evap,CO_2}$ , and  $T_{evap,CO}$ , respectively.  $T_{evap,CO}$  is shading with a light red region to highlight the wide range of possible values calculated from different binding energies given by KIDA. As a comparison, constant  $T_{\rm sub}$  in Öberg et al. (2011) are marked with short arrows in these three colors on the right edge of each panel. The vertical cyan dashed lines and grey dotted lines mark the location of the planets and pressure maximum/dust trapping.

midplane, we focus on the midplane temperature  $T_{mid}$  derived from both iteration and non-iteration methods.

Figure 2.4 shows the comparisons between azimuthal averaged  $T_{mid}$  (cyan lines) of planets at 4 au over 2000 orbits calculated by iteration method (upper panels) and non-iteration method (lower panels). The gray shading regions represent the  $T_{mid}$  in different azimuthal angles. Three molecules and their pressure-dependent sublimation temperatures  $T_{evap,H_2O}$ ,  $T_{evap,CO_2}$ , and  $T_{evap,CO}$  (calculations follow the recipe in Hollenbach et al. (2009)) are marked as blue, green, and red dash-dotted lines, respectively. We use binding energy provided on KIDA<sup>1</sup> database. The uncertainty of  $T_{evap,CO}$  due to different binding energy choices is shown as a light red shading area. As for comparison, the constant sublimation temperatures  $T_{evap,H_2O} = 125$ K,  $T_{evap,CO_2} = 47$ K,  $T_{evap,CO} = 25$ K in Öberg et al. (2011)

<sup>&</sup>lt;sup>1</sup>https://kida.astrochem-tools.org

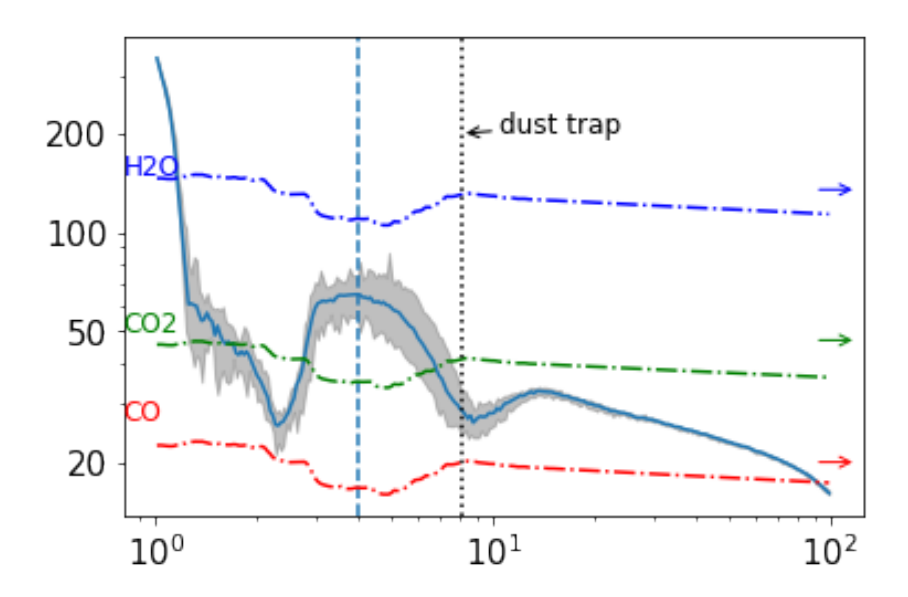
are marked as short horizontal arrows in corresponding colors. Overall, the iteration method predicts distinct  $T_{mid}$  when compared with the non-iteration method at two regions. In particular, in the inner disk regions(r < 10au) and the gap regions.

At the inner disk, iterated  $T_{mid}$  drops more rapidly than non-iterated  $T_{mid}$ . For example, we can clearly see the differences between Panel d and h in these three figures. As  $M_p = 10 M_{\oplus}$ , such low planet has negligible effects on disk temperature as they are difficult to open gaps to influence  $T_{mid}$ . Therefore, the difference between Panel d and h does not come from the planet opening gaps, instead, the difference comes from the methods we adopt, iteration or non-iteration. The underlying physical explanation will be discussed in more detail in section 2.4.3. In short, the puff-up of the scale height at the inner dust rim cause a strong shadowing effect and lower the temperature in these regions.

At the gap regions, iteration predicts more significant  $T_{mid}$  contrasts between inside gap regions and outside gap edges than the non-iteration. The highest contrast of  $T_{mid}$  can be up to 40K (increase from 30K to 70K) when  $3M_{\rm J}$  or  $1M_{\rm J}$  at 4au of iteration method (see Panel a and b). The underlying explanation is the iteration tends to open deeper gaps than the non-iteration and allows more stellar photons to penetrate into the midplane and increase  $T_{mid}$ . However, the peak values of  $T_{mid}$  from both methods are similar in the same  $M_p$  and  $r_p$  conditions.

Regarding the iteration results, as  $M_p$  increases, the  $T_{mid}$  at gaps increases more significantly. It is because more massive planets are able to open deeper and wider gaps and more stellar photons can penetrate deeper at the gap region and heat up midplane dust and gas. Such a trend is also seen in the non-iteration method. Furthermore, the midplane temperature of  $r_p = 10,30$  au are shown in Figure 2.14 and 2.15, respectively.

By combing the sublimation temperature and the disk midplane temperature, we can measure where the midplane icelines of different molecules are in section 2.3.5. The numbers of icelines primarily rely on the values of  $T_{\rm sub}$  and the disk  $T_{mid}$ . If we use the values of binding energy suggested in Öberg et al. (2011), the overall profiles of sublimation temperature of all these three volatile will shift up or down.



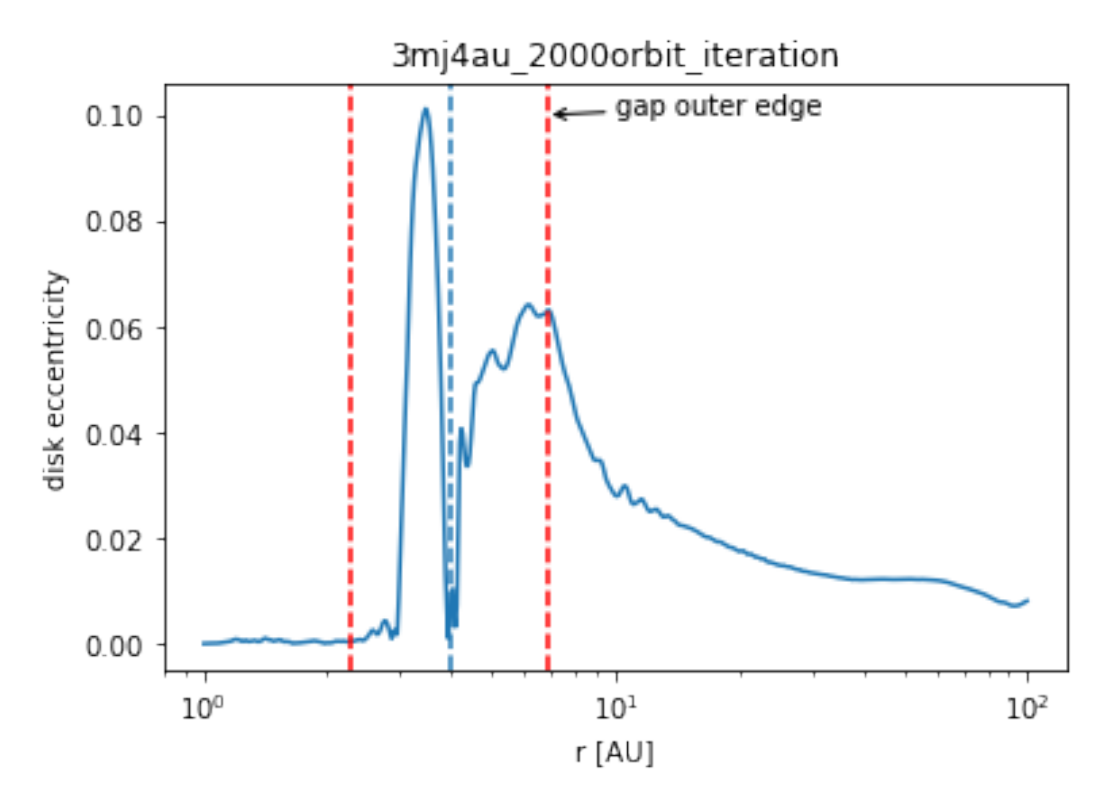
**Figure 2.5:** Similar to Figure 2.4 (a) but  $T_{\text{sub}}$  is calculated by using molecule binding energy in Öberg et al. (2011).

Figure 2.5 is a plot of  $T_{mid}$  but with  $T_{sub}$  calculated from binding energy adopted by Öberg et al. (2011). Compared with 2.4(a), now the whole  $T_{evap,CO}$  shifts lower significantly and the CO iceline moves outward dramatically to around 90au, and only one CO iceline exists. Therefore, in this case, particles or pebbles with CO ices only exist in the very outer disk.

## 2.3.3 Eccentricity

When comparing the density results within either iteration or non-iteration method, if the planet masses  $M_p < 1 M_{\rm J}$ , they open quite circular gaps and more massive planets open deeper and wider gaps. In terms of the most massive cases of  $3 M_{\rm J}$  in our modeling, the planets open eccentric gaps. Our results agree with the results from Kley & Dirksen (2006) who found that planets with mass  $M_p > 3 M_{\rm J}$  open eccentric gaps in disks with a viscosity of  $v = 10^{-5}$  or  $\alpha \approx 0.004$ . In this section, we quantify the eccentricity e of the gaps opened by  $M_p = 3 M_{\rm J}$  or  $1 M_{\rm J}$  with two kinds of methods. Because the inner and outer edge of a gap has different eccentricities, we measure them separately.

The first method is obtaining *e* by fitting ellipses to the shape of the inner/outer



**Figure 2.6:** Disk eccentricity calculated from Equation 2.2 for an example of  $3M_J$  at 4au of iteration method. Planet location is marked with a vertical blue dashed line. The gap inner and outer edges are marked by red dashed lines.

edges of gaps. The second method is using equation 28 in Ju et al. (2016)

$$e(r) = \frac{|\int d\phi \Sigma(r,\phi) v_r \exp(i\phi)|}{\int d\phi \Sigma(r,\phi) v_\phi}$$
 (2.2)

to calculate e at the location of the inner/outer edges of gaps. Figure 2.6 displays an example of using the equation 2.2 to calculate the e as a function of radius of the simulation of  $3M_{\rm J}$  at 4 au over 2000 orbit by using iteration method. At this case,  $e \sim 0.06$  at the gap outer edge, which is not very different from the value in Kley & Dirksen (2006) though the disk parameters (e.g. viscosity  $\alpha$ , aspect ratio H/r) are not exactly the same.

Table 2.3 summarizes gap eccentricities e from different simulations measured by different methods, fitting ellipse in "graph" or calculating with "formula". Names of different cases are written in abbreviations. For example,  $3mj4au_it_graph$  means the case of  $3M_J$  at 4 au of iteration measured by graph method, and so on.

In both methods, we average the values of the last 500 orbits (shown as "mean" in Table 2.3) and calculate their standard deviations (shown as "std" in Table 2.3). In general, both iteration and non-iteration methods get similar e. Also, the values of e are similar from the graph and formula measuring method.  $M_p = 3M_{\rm J}$  induces relatively high  $e \sim 0.07$  when  $r_{\rm p} = 4$  or 10 au, which could also be seen from the eccentric gaps in Figure 2.2 and Figure 2.12.  $M_p = 1M_{\rm J}$  only open gaps in almost circular shapes.

The high eccentricity of a gap can have a non-neglectable effect on the temperature. For the most eccentric case, for example, e = 0.08 measured by graph fitting of 3mj4au of the iteration method, we can obtain  $r_{min} = 6$  au and  $r_{max} = 7.6$  au from fitting the ellipse of the outer gap edge. By plugging them into the corresponding temperature profile, we can find  $T_{mid}$  varies from about 40 to 27K. In other words, CO ice might exist at the semi-major axis side but sublimate at the semi-minor axis side of the outer edge of gaps.

#### 2.3.4 Dust trap

Dust grains in a disk experience radial drift unless they get trapped in gas pressure bumps (e.g. Pinilla et al. (2012a,b); Dullemond et al. (2018)). We can investigate pressure gradient profiles around the gaps to see how our model affects dust-trapping conditions. Pressure is given by  $P(r) = \Sigma(r)c_s^2(r)$ . Here both the gas surface density and sound speed  $c_s$  are azimuthally averaged after 2000 orbits. Different pressure gradients from iteration and non-iteration can lead to different efficiency of dust trapping. Thus, dust of different sizes could be distributed differently.

The location of the pressure maximum, also named dust-trapping location  $r_{\rm dt}$  here, is when the pressure gradient is zero ( ${\rm d} \log P/{\rm d} \log r=0$ ). We obtain the  $r_{\rm dt}$  of different cases of  $M_p$  and  $r_{\rm p}$  of the iteration and non-iteration methods. We find that there are no dust traps in the cases of  $M_p=10~M_{\oplus}$  when planets are at  $r_{\rm p}=10$  au of the non-iteration method, and  $r_{\rm p}=30$  au of both methods. Figure 2.7 shows the normalized dust trapping location  $(r_{\rm dt}-r_{\rm p})/R_{\rm H}$  as a function of planet mass  $M_p$ . If for a specific case, there is no  ${\rm d} \log P/{\rm d} \log r=0$ , we put  $(r_{\rm dt}-r_{\rm p})/R_{\rm H}=0$ .

**Table 2.3:** Comparison of inner and outer gap edge eccentricity e of massive planets at different  $r_{\rm p}$  from iteration or non-iteration method. e is measured by either "graph" or "formula" method and the averaged values of the last 500 orbits are marked as "mean" and the uncertainty are marked as "std". Values of e > 0.05 are highlighted with purple background.

	e_in_mean	e_in_std	e_out_mean	e_out_std
3mj4au_it_graph	0.01	0	0.08	0.03
3mj4au_it_formula	0	0	0.06	0
1mj4au_it_graph	0.01	0	0.01	0.01
1mj4au_it_formula	0	0	0.01	0
3mj4au_nonit_graph	0	0	0.08	0.04
3mj4au_nonit_formula	0	0	0.07	0
1mj4au_nonit_graph	0.02	0	0.01	0
1mj4au_nonit_formula	0	0	0.01	0
3mj10au_it_graph	0.01	0	0.06	0.02
3mj10au_it_formula	0	0	0.07	0
1mj10au_it_graph	0.01	0	0.01	0
1mj10au_it_formula	0	0	0.01	0
3mj10au_nonit_graph	0.03	0.02	0.06	0.03
3mj10au_nonit_formula	0.02	0	0.07	0.01
1mj10au_nonit_graph	0.04	0.01	0	0
1mj10au_nonit_formula	0.01	0	0	0
3mj30au_it_graph	0.01	0	0.01	0
3mj30au_it_formula	0	0	0	0
1mj30au_it_graph	0	0	0	0
1mj30au_it_formula	0	0	0	0
3mj30au_nonit_graph	0.05	0.03	0	0
3mj30au_nonit_formula	0.04	0	0	0
1mj30au_nonit_graph	0	0	0.01	0
1mj30au_nonit_formula	0	0	0	0

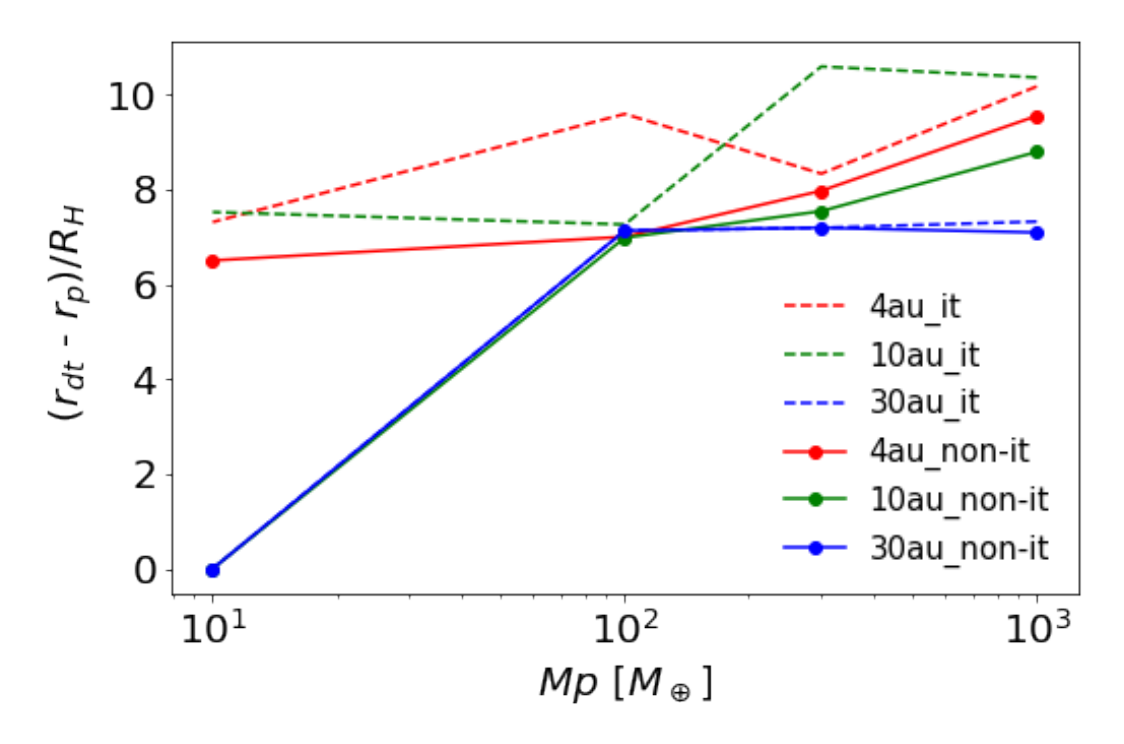


**Figure 2.7:** Normalized dust trapping location as a function of planet mass  $M_p$ . The iteration and non-iteration are marked with dashed and solid lines and different  $r_p = 4$ , 10, and 30 au are in red, green, and blue, respectively.

In general, if a planet can form a pressure maximum to trap dust around the outer gap edge,  $r_{\rm dt} - r_{\rm p} = 7 \sim 10 R_{\rm H}$  regardless of different  $M_p$  and  $r_{\rm p}$ . The dust-trapping locations  $r_{\rm dt}$  from both methods do not show a big difference, especially for  $r_{\rm p} = 30$  au cases. In smaller  $r_{\rm p}$  cases, iteration tends to trap grains in slightly outer locations than non-iteration for a given  $M_p$  and  $r_{\rm p}$ . Furthermore,  $r_{\rm dt} - r_{\rm p}$  is roughly equal to the gap widths in each case. In other words, the outer gap edges are approximately the middle points between planets and dust-trapping locations.

As small dust particles can couple well with gas and may flow through the dust trap, there should be a minimum grain size so that grains larger than this threshold can be trapped by the pressure bump. Thus, we can further infer what ratio of dust is trapped by a pressure bump. The minimum particle size that can be trapped is described by: Pinilla et al. (2012a)

$$a_{\text{critical}} = \frac{6\alpha\Sigma_{\text{g}}}{\rho_{\text{s}}\pi|(\text{dlog}P/\text{dlog}r)|} \left| \left( \frac{3}{2} + \frac{\text{dlog}\Sigma_{\text{g}}}{\text{dlog}r} \right) \right|$$
(2.3)

In our modeling,  $\alpha = 10^{-3}$ ,  $\rho_s = 3.710g/cm^3$ . We find that the iteration has

similar  $a_{\text{critical}}$  of about 0.3cm as the non-iteration results at the location of pressure maximum  $r_{\text{dt}}$ . Furthermore, we assume grain size distribution follows Mathis et al. (1977),  $n(a) \propto a^{-p}$ , where p = 3.5. The range of dust sizes is from  $0.1 \mu m$  to  $a_{\text{frag}}$ , where  $a_{\text{frag}}$  is the maximum particle size before they fragment due to turbulent relative velocities  $v_f$  (Birnstiel et al., 2012):

$$a_{\text{frag}} = \frac{2}{3\pi} \frac{\Sigma_{\text{g}}}{\rho_{\text{s}} \alpha} \frac{v_f^2}{c_{\text{s}}^2}$$
 (2.4)

Follow Pinilla et al. (2012a), we set  $v_f = 10\,\mathrm{m\,s^{-1}}$ . We find that the iteration,  $a_{\mathrm{frag}}$  could be a few times higher than non-iteration. To calculate the fraction of dust mass trapped in the dust-trapping regions, we multiply the number of particles in a size bin n(a)da by the mass of a spherical particle (of size a) and integrate over the size range from  $a_{\mathrm{critical}}$  to  $a_{\mathrm{frag}}$ . The dust-trap fraction is:  $f_{trap} = (a_{frag}^{0.5} - a_{cri}^{0.5})/(a_{frag}^{0.5} - a_{\min}^{0.5})$ .  $f_{\mathrm{trap}}$  represents the fraction of the dust mass that could be trapped in the pressure bump region compared to the total dust mass of the pressure bump region.

If we take the  $3M_{\rm J}$  at  $4r_{\rm p}$  as an example, at the region of the pressure bump (assume from outer gap edge  $r_{gap,out}$  to  $2r_{\rm dt}-r_{gap,out}$ ), both iteration and non-iteration have similar averaged  $a_{\rm critical}=2\times10^{-2}$  cm. If we assume  $a_{min}=10^{-5}$  cm, and plug in averaged  $a_{\rm frag}=10$  cm for iteration or averaged  $a_{\rm frag}=3$  cm for non-iteration. Therefore, we have  $f_{\rm trap}=0.96$  for iteration and  $f_{\rm trap}=0.92$  non-iteration, which means a slightly higher fraction of dust mass could be trapped in the pressure bump predicted by the iteration. Proper inclusion of dust evolution is needed to test this hypothesis in the future.

## 2.3.5 Distribution of ice species

Figure 2.4, 2.14, and 2.15 show  $T_{gas}$  from the iteration method and how it deviates from the non-iteration approach. For this reason, the ices of  $H_2O$ ,  $CO_2$ , and CO are distributed in different locations when comparing the two methods. More ice means more solid masses could contribute to the pebble or planetesimal formation, while the available species of ice can affect the final planetesimal composition. Therefore,

in this section, we use temperature and pressure information to show where different icelines are, where ice distributes throughout the whole disk, and what kinds of ice species form at dust trapping locations.

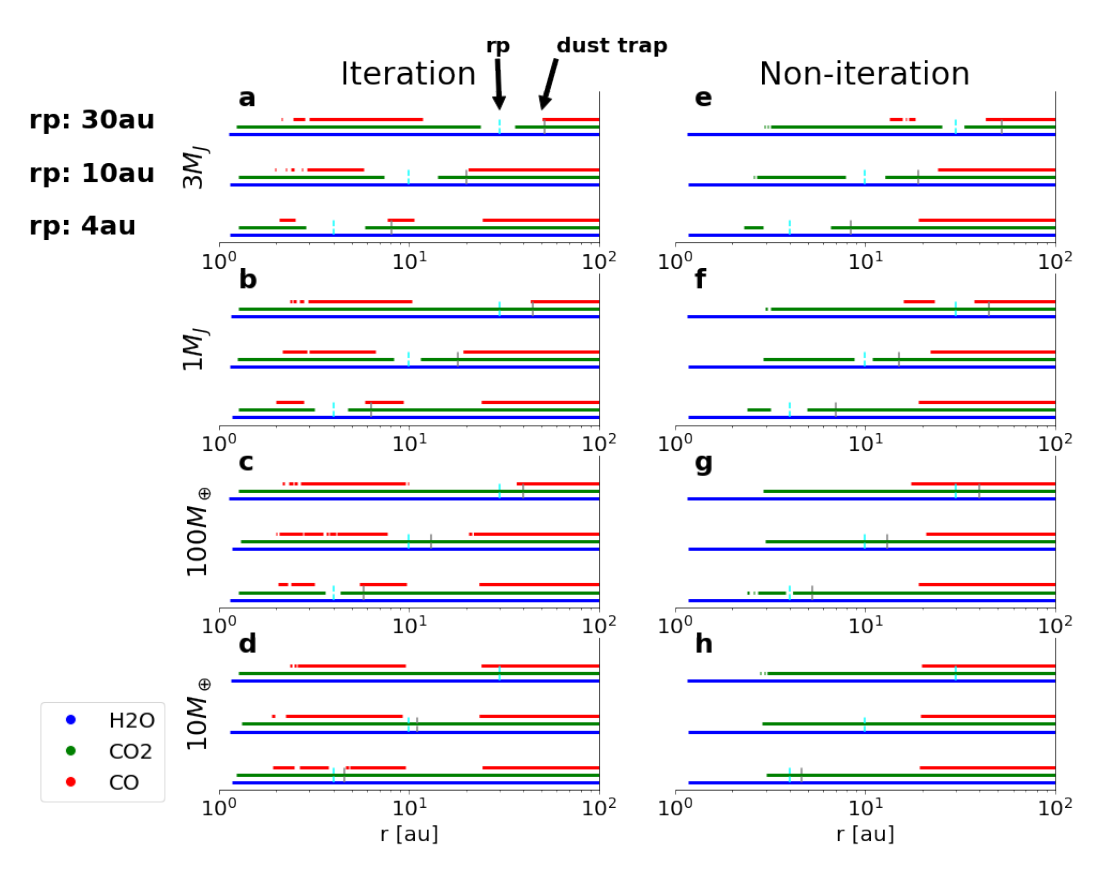
For each specific molecular iceline, the number of radial icelines depends on the number of intersections between the disk midplane temperature  $T_{mid}$  and the radial pressure-dependent sublimation temperature  $T_{sub}$ . We notice the binding energy of CO has a wide range of values in KIDA and we show the uncertainty of the  $T_{evap,CO}$  with light red shading regions in Figure 2.4, 2.14, and 2.15. Therefore, we need to keep in mind that the numbers and locations of CO iceline could vary due to adopting different binding energy of CO.

Figure 2.8 summarizes the ice distribution of  $H_2O$ ,  $CO_2$ , and CO throughout the whole disk. The left and right columns show iteration and non-iteration results. In each column, from top to bottom panels,  $M_p = 3M_J$ ,  $1M_J$ ,  $100M_{\oplus}$ , and  $10M_{\oplus}$  are shown. In each panel, from bottom to top, cases of  $r_p = 4$ , 10, and 30 au are shown. The ices of  $H_2O$ ,  $CO_2$ , and CO are displayed as horizontal blue, green, and red bars, respectively. Planet and dust trap locations are marked as cyan and grey dashed lines. To simplify, here we only consider the azimuthal averaged  $T_{mid}$  to obtain the radial midplane iceline locations for different volatiles. However, for some high eccentric cases caused by massive planets, the iceline locations can vary at different azimuthal angles. In addition, we define an iceline as the boundary where volatile freeze out and condense into solid, but do not count it when volatile sublimates.

Without considering the time evolution and dust drift, our static ice distribution model gives the following results for the main species:

 $H_2O$  ice: all modeling results from the iteration or non-iteration methods for different  $M_p$  and  $r_p$  yield only one water iceline in the disk, and similar iceline locations at around 1.2 au in our disk model. Therefore, planetesimals formed outside 1.2 au can have  $H_2O$  ice.

 $CO_2$  ice: Both iteration and non-iteration methods in the massive planet cases can have two obvious  $CO_2$  icelines shown in Panels a, b, e, and f (except  $r_p =$ 



**Figure 2.8:** Ice distribution in disks with different  $M_p$  and  $r_p$ . The iteration and non-iteration results are shown in the left and right panels, respectively. High to low  $M_p$  are listed from top to bottom panels. In each panel, for instance,  $3M_J$  of iteration method, there are three groups of data representing the cases of planets at 4 (bottom), 10 (middle), and 30 au (top), respectively. The location of  $H_2O$ ,  $CO_2$ , and CO ice is in blue, green, and red bars. Vertical cyan dashed lines mark  $r_p$  and grey dashed lines display the corresponding dust-trap location. Note that in some cases there is no grey-dashed line because there is not dust trapping.

30 au in Panels b and f) in Figure 2.8. Because the presence of a massive planet  $(M_p \ge 1M_{\rm J})$  opens deep enough gaps that increase the  $T_{mid}$ , which causes  ${\rm CO}_2$  ice to sublimate at the gap regions and freeze out again in the outer disks. Locations of outer  ${\rm CO}_2$  icelines are close to gap outer edges. In the inner disk, locations of  ${\rm CO}_2$  icelines are predicted to be around 1.5 au in iteration whereas about 3 au in non-iteration.

CO ice: One of the most distinct features between the two kinds of models is that the iteration predicts more complicated CO icelines features than non-iteration. Because of the  $T_{mid}$  increase at the gap regions, all models of iteration suggest the

CO ice would sublimate except  $10M_p$  cases. For  $r_p = 4$  au, despite neglecting the short discontinuations in red bars (due to noise in radiative transfer temperature) in those iteration panels, we find three icelines of CO in iteration while only one iceline in non-iteration. In this case, the CO ice can exist in three discrete radial regions in iteration results. The first region, from 1 au to somewhere close to the inner edges of gaps, where the inner disk  $T_{mid}$  drops. The second region, from somewhere near the outer edges of the gap to around 10 au, is ascribed to gap heating with the shadowing effect in the inner disk causing  $T_{mid}$  to drop. The third region starting from about 25 au is due to the outer disk temperature decrease, which is broadly similar to the non-iteration CO ice distribution region outside 20 au.

## 2.4 Discussion

Our coupled treatment of hydrodynamics and radiative transfer allows us to shed new light on the feedback of gap-opening planets on the temperature and pressure structure of the protoplanetary disk, which in turn may influence the composition of planetesimals and planets. We discuss this below, followed by a discussion of iceline and disk substructure, as well as caveats of this work and potential improvements for future models.

## 2.4.1 The C/O ratio as a planet formation tracer

The carbon-to-oxygen ratio is a potential signature of the history of planet formation (Öberg et al., 2011). Physical and chemical models of protoplanetary disks, with varying degrees of complexity, have been developed to understand the radial behaviour of the C/O ratio (e.g., Cleeves et al., 2018; Zhang et al., 2019; Miotello et al., 2019; Bosman et al., 2021). Recently, an azimuthal C/O ratio variation in protoplanetary disk has also been reported and modelled (Keyte et al., 2023). As we have shown, planet-induced gaps introduce significant new complexity to this picture by creating feedback and altering the thermal structure. This in turn modifies various ice lines and thus the C/O-ratio imprinted on subsequently forming planetesimals and planets.

To investigate how radial variations in the C/O ratio are affected by feedback

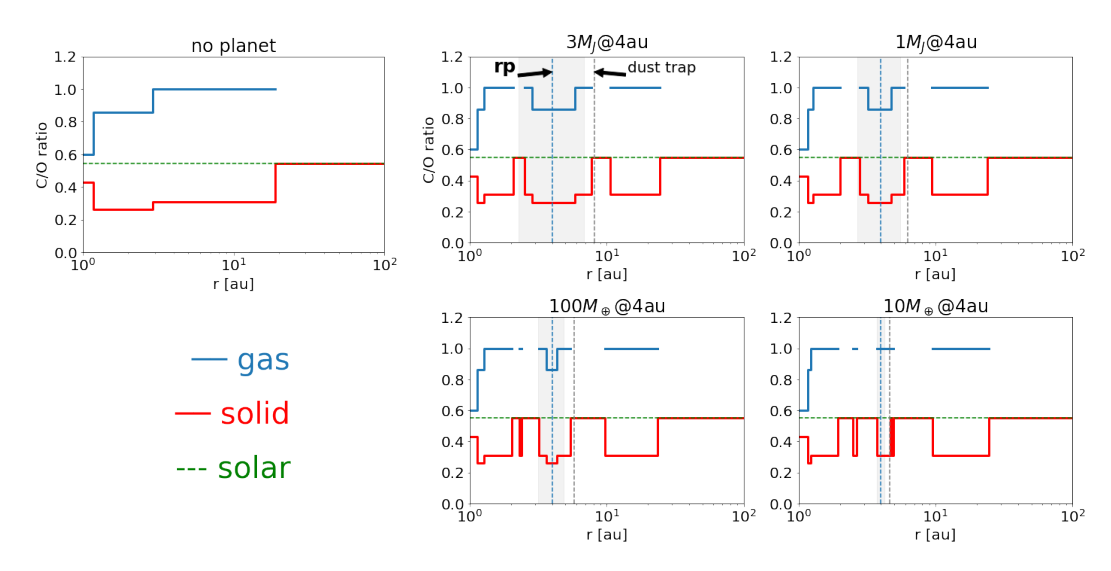


**Figure 2.9:** C/O ratio as a function of location in a disk, for different masses of a gapopening planet at 4 au. From the upper middle to lower right panels, we show a planet mass of  $3M_{\rm J}$ ,  $1M_{\rm J}$ ,  $100M_{\oplus}$ , and  $10M_{\oplus}$  at 4 au using the iteration method, and a disk without planets (upper left panel) for comparison. The blue and red solid lines show gas- and solid-phase C/O ratios, whereas the solar C/O ratio is marked by a green dashed line. The gap regions are shaded. The planet location and dust trap location are marked as vertical cyan and grey lines.

from gap-opening planets, and the presence of a puffed-up inner rim, we follow the prescription from Öberg et al. (2011). We assume the only C and O carriers are  $H_2O$ , CO,  $CO_2$ , refractory carbon, and silicate minerals, using the same abundances as that study. The total abundance of each species summed over the gas and solid phase does not vary with radius.

Figure 2.9 shows how the gas- and solid-phase C/O ratio varies as a function of location in a disk, and for different  $M_p$  at  $r_p = 4$  au, for models using our iteration method. For comparison, the baseline model without a planet is also shown, analogous to the standard "Öberg model" for the C/O profile. We note that analogous changes can be observed for planets at larger orbits, but due to the relevance to most known planetary systems which are close-in, as well as the analogy with the solar system, we focus here on the 4 au case.

Based on our iterative models, the introduction of a gap-opening planet significantly alters the radial profile of the C/O ratio in the gas and solid phase, compared to the baseline (no-planet) case.

Firstly, the presence of a gap makes the disk temperature (and pressure) profile

strongly non-monotonous, which can create multiple iceline locations for a single chemical species. A monotonous, smoothly decreasing temperature profile underlies the widely studied picture of well-defined, unique icelines. In that case, the more refractory species (silicates, organic carbon, water ice) each have their iceline closer to the star than the more volatile species (e.g., CO).

Secondly, by comparing the results from disks hosting different mass planets, we can see the planet gap-opening effect on C/O is stronger as planet mass increases. The reduced optical depth within the gap leads to increased heating which causes  $T_{mid}$  to rise above the CO<sub>2</sub> sublimation temperature. This returns proportionally more oxygen than carbon back to the gas phase, thereby decreasing the gas-phase C/O ratio locally.

Our results show that the feedback from gap-opening planets can significantly affect the gas- and solid-phase C/O ratio at small spatial scales within a protoplanetary disk. Such variations have important implications for the composition of icy planetesimals, and the gas from which giant planets accrete their envelopes. Additionally, our findings demonstrate that radially distinct regions of the disk can be characterised by the same C/O ratio, which complicates the usage of C/O as a formation tracer. To construct more accurate models, it is essential that future observations focus in measuring the C/O ratio at planet-forming scales. We note, however, that some of the variations seen in the radial location of molecular icelines in our models are as little as  $\sim 1$  au, which can be difficult to resolve even with ALMA, though the larger shifts ( $\sim 10$  au or more) can be more easily measured. The largest-scale variations are evident for high-mass planets at large separations ( $M_P = 3M_J$  at 30 au in our model, Figure 2.8a).

The degree to which the gap-modified gas and solid composition will be reflected in the atmospheric composition of a forming planet will further depend on the degree of mixing between the core and atmosphere, and the amount of sublimation that takes place during accretion. The scenario is further complicated by considering the vertical layer in which planets accrete their envelopes. Meridional flows from the disk surface may favour the accretion of gas and small grains from

the disk surface layers, for example (e.g. Teague et al., 2019a).

#### 2.4.2 Ice lines and dust rings

The altered thermal and ice line structure of a disk with a gap-opening planet has implications for the observational study of disk substructure, both spectroscopy of the gas and also the dust rings which are widely observed in disks with ALMA.

We illustrate this for the case outlined in Figure 2.4(a), a  $3M_{\rm J}$  planet at 4 au. Heating due to gap-opening increases the local midplane temperature above the CO sublimation temperature, introducing a new CO condensation front at the outer edge of the gap in a region of the disk where CO would otherwise be entirely frozen out.

As also highlighted in Figure 2.4, a dust trap is located in the pressure maximum just outside a gap. Furthermore, results in the literature suggest regions near ice lines may be favorable for the pile-up of icy pebbles (e.g., Hyodo et al., 2019). As pebbles cross the ice line and sublimate, outward diffusion followed by recondensation may locally enhance the surface density outside of the iceline, triggering instabilities which can lead to rapid pebble and planetesimal growth (Drążkowska & Alibert, 2017). High dust-to-gas ratios and viscosity gradients produced by the density enhancement could further amplify the effect (e.g., Brauer et al., 2008; Ros & Johansen, 2013; Bitsch et al., 2014; Drążkowska & Dullemond, 2014; Flock et al., 2015).

This rapid growth of pebbles around condensation fronts is tentatively supported by observations of disks such HL Tau, where the location of millimeter dust rings has been linked to the icelines of water and other key volatiles (Zhang et al., 2015). Similarly, grain size distributions inferred from ALMA observations of HD 163296 are consistent with the enhanced production of large grains at the CO iceline (Guidi et al., 2016). However, no unambiguous correlation between dust rings and ice lines on a standard monotonously radially decreasing temperature profile has been found. Results using empirical temperature estimates seem to disfavor such correlation (Long et al., 2018).

Although icelines have been invoked to explain the rings and gaps observed in a handful of disks, such as HL Tau (Zhang et al., 2015), icelines are not a preferred

explanation when looking at large surveys of protoplanetary disks (Huang et al., 2018; Long et al., 2018; Van Der Marel et al., 2019). This is because most of the locations of substructures do not coincide with the sublimation temperature of the main disk volatiles, when assuming that the disk temperature is set by stellar irradiation. Under this hypothesis, a correlation between the location of substructures and the stellar luminosity is expected.

However, as we show in this work, this potential correlation may get much more complicated when a planet is embedded in the disk. The planet alters the temperature-pressure profile of the disk, moving the ice lines to different radii and even creating multiple, radially widely separated ice lines for a single species. Therefore, our current results suggest that it is not necessarily a correlation with the stellar luminosity as it is usually assumed, but that embedded gap-opening planets need to be accounted for to fully assess the locations of ice lines and their correlation with the locations of dust (pebble) rings.

In addition, Pinilla et al. (2017) demonstrated that due to the variations of dust sticking properties, ice-covered dust particles can create "traffic jams", which result in rings and gaps when observed at different wavelengths. The inclusion of dust evolution models in the framework of our models is needed to test if multiple substructures are expected in the disks as a result of a single planet embedded and multiple icelines locations of different volatiles.

## 2.4.3 Inner rim midplane temperature drops

In this section, we discuss the temperature decrease in the inner few au in disks in section 2.3.2. As Figure 2.4, 2.14, and 2.15 show, even the lowest  $M_p = 10 M_{\oplus}$  case which represents minor or no planet effect on the disk, the iteration method predicts strong  $T_{mid}$  drops in this inner disk region. On the contrary, such an effect is not shown in the non-iteration method. The physical explanation is that the puff-up of the scale height can cause a strong shadowing effect to decrease the temperature within 10 au in the RADMC3D simulation. The reason why there is a puffed-up scale height at the inner rim at 1 au in our transition disk models is that stellar photons hit a dust wall, increasing the dust temperature.

As we assume the dust and gas temperatures are well coupled, the gas temperature is also high and causing the gas scale height to have a strong puff-up. This phenomenon is also suggested in Figure 3 in Dullemond et al. (2001), as well as Jang-Condell & Turner (2012, 2013); Siebenmorgen & Heymann (2012); Zhang et al. (2021a). In our RADMC3D setups, we input time evolving scale height for the surface density to volume density extension process. As the scale height indicated by the  $T_{mid}$  from last RADMC3D has puff-up in the inner rim, our iteration models can naturally capture such effects. However, in the non-iteration method, the input scale height for RADMC3D is just the smooth flaring scale height as that in the FARGO3D setup. Therefore, the iteration can have an advantage in making use of the physical temperature obtained by radiative transfer for a specific disk model rather than using the initially assumed temperature as non-iteration. In addition, we measure the aspect ratio h/r of the puff-up inner rim at 1 au is about 0.035 and then it decreases to the lowest value of about 0.015 at about 1.5 au. For the region further away from 1.5au, h/r increases as a power law with a flaring index of 0.25 which is similar to the power law profile of non-iteration h/r.

The change in inner disk temperature structure between the commonly used isothermal (non-iteration) method and our iteration method also impacts the behaviour of elemental ratios like C/O. In our models using the iteration method, shadowing by the puffed-up inner rim causes  $T_{mid}$  dropping off more quickly within the inner disk, moving the  $H_2O$  and  $CO_2$  icelines inwards. This translates to a steep rise in the gas-phase C/O ratio, as a large proportion of the total atomic oxygen is frozen-out into solids. In this scenario, C/O reaches unity within  $\sim 1.5$  au, compared to  $\sim 3$  au in the non-iteration and classical models.

## 2.4.4 Assumptions and limitations

There are a number of simplifications in our hydrodynamical and radiative transfer simulations that can be improved in future work. First, we only consider 2D hydrodynamical simulations in radial and azimuthal directions instead of full 3D hydrodynamical simulations, which benefits us for speeding up the whole iteration process. However, 3D hydrodynamical simulations can allow one to get rid of the

vertical isothermal assumption which will be useful for addressing vertical stratified problems (e.g. ice-surface distribution, gas molecule emission layers.) In this paper, we only focus our discussion on the midplane temperature and its effect on midplane ice distribution.

Second, we have some simplifications about dust in our modelings. hydrodynamical simulations, we do not include dust species in order to speed up the simulation process. In addition, only one small grain size,  $0.1\mu m$ , is included in the radiative transfer simulations. If we consider grain size distribution or dust evolution process, like grain growth or fragmentation, it is still unclear how can these factors change the dust distribution and hence disk temperature. Because we do not have a dust density distribution in our models, we also neglect dust settling in our models. As a consequence, it is possible that when dust settling is included, less dust remains on the disk surface, allowing stellar radiation to penetrate deeper into the disk and increase  $T_{mid}$ . Our models also neglect to account for dynamical effects such as radial drift and mass accretion, which add considerable complexity. For example, studies have shown that radial drift can produce multiple icelines Cleeves (2016) or make icelines thermally unstable under typical disk conditions (Owen, 2020). Icy volatiles drift faster that those in the gas-phase, which results in the iceline progressively moving inwards, condensing more volatiles. The iceline then recedes as volatiles sublimate, on timescales much shorter that the disk lifetime (1000-10,000 years). Similarly, the mass accretion rate plays an important role in iceline evolution, with iceline moving inwards when accretion rates are high, and migrating back out in the later stage of disk evolution when the accretion rate decreases (Oka et al., 2011). The combined effects of radial drift and mass accretion can cause molecular icelines to moves inwards by as much as 60% (Piso et al., 2015)

Third, we do not consider viscous heating which can be dominant in the midplane of the inner disk (e.g. Broome et al. (2023)). Thus, the viscous heating may have sufficient effects on increasing the very inner disk  $T_{mid}$ . This may have a strong effect on our 4au cases. Also, our models do not capture shock heating from the planet which can be significant for massive planet cases.

Finally, we choose 100 orbits as our iteration step to implement the feedback from RADMC3D to FARGO3D. However, we notice that the thermal relaxation time can vary from about 100 to 0.1 dynamic timescale from 1 to a few tens au (Malygin et al., 2017; Pfeil & Klahr, 2019) and our model can not capture this. The number of the iteration step we decide is a balance between the total simulation time and reflecting the gap opening thermal feedback properly. One possible way to improve the approach is if we are only concerned about the radial temperature structure but ignore the azimuthal variations, we can use fewer photon package numbers for fewer azimuthal grid cell RADMC3D simulations to speed up each iteration step and do more iterations.

In future work, we will focus on the improvement of some of these limitations, in particular the effect of including dust in the models.

## 2.5 Conclusions

In this paper, we present a new method to study the gap-opening effect on protoplanetary disk temperature structure by iterating hydrodynamical and radiative transfer simulations. We quantify the planet-opening gap profiles including gap width, depth, and eccentricity, and explore the dust-trapping condition in outer gap edges. By obtaining the temperature profiles in disks, we study the volatile iceline locations and ultimately provide new C/O ratio for disks with embedded planets. During the modeling, we compare our iteration models with the conventional non-iteration models and conduct parameter studies of different planet masses  $M_p$  and planet locations  $r_p$ . Our main conclusions are as follows:

- (i) Gap profiles: the iteration method predicts deeper and more eccentric gaps than the non-iteration. The most significant difference in gap depth comparison between these two methods is seen at  $1M_{\rm J}$  at 4 au or 10 au, where the iteration gap depth is about an order of magnitude deeper than the non-iteration.
- (ii) Dust trap: both iteration and non-iteration indicate similar locations of pressure maximum for dust trapping  $r_{\rm dt}$ , which is about 7-10  $R_{\rm H}$  further away from

- $r_{\rm p}$ . However, the iteration predicts a larger fragmentation grain size across the pressure bump, and as a consequence, a slightly higher fraction of dust could be trapped in the pressure bump.
- (iii) Midplane temperature: our iteration models can capture the gap-opening process by a planet and its effect on the time evolution of the disk temperature structure, whereas the conventional non-iteration models do not capture. By implementing the iteration method, we show that the strong midplane temperature drops in the inner few au of disks because of the shadowing effect caused by the puff-up disk inner rim. Meanwhile, the midplane temperature  $T_{mid}$  increases significantly in the gap regions due to more photons can penetrate into the midplane. The maximum  $T_{mid}$  contrast between gap edges and gap center is about 40K when  $3M_{\rm J}$  or  $1M_{\rm J}$  presents at 4 au.
- (iv) Icelines: because of  $T_{mid}$  drops,  $CO_2$  and CO ice may exist in the inner disk region (at a few au) in the iteration model. At gap regions, both iteration and non-iteration predict that  $CO_2$  or CO ice may sublimate. As a result, the non-iteration suggests that more than one  $CO_2$  or CO iceline can appear in a disk, whereas the iteration models propose that even more CO icelines might exist in giant planet-forming disks. This result suggests that the combination of an embedded planet and different locations of the iceline of the same volatile can still explain the observed substructures in protoplanetary disks.
- (v) C/O ratio (Fig. 2.9): the radial C/O ratio profile across the disk is significantly more complex due to the presence of gaps opened by giant planets in comparison to disk models without embedded planets. As a consequence, the feedback of the planet-opening gap on the disk thermal structure can significantly influence the composition of material available for the giant planet's atmosphere or for the next generation of planet formation.

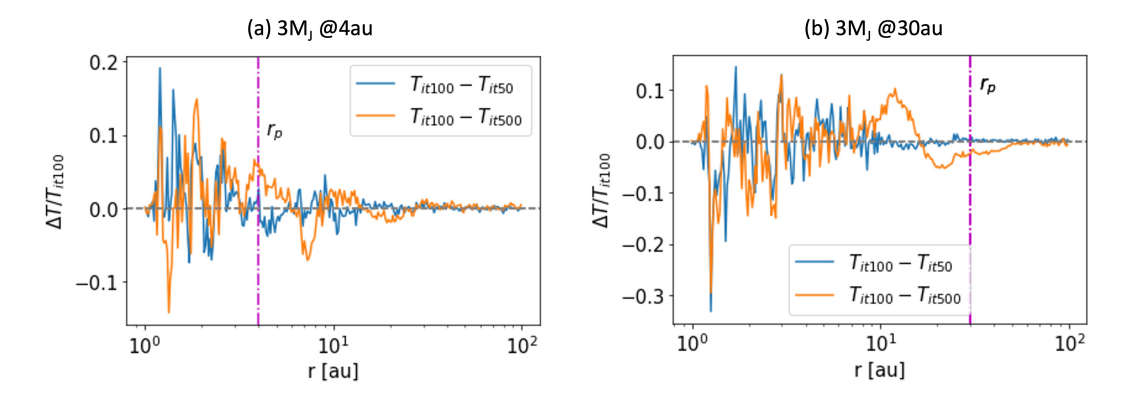


**Figure 2.10:** Comparison of midplane temperature over 2000 orbits by using different iteration steps. The y-axes  $\Delta T/T_{\rm it100}$  show the normalized temperature difference between two iteration steps.  $T_{\rm it500}$ ,  $T_{\rm it100}$ , or  $T_{\rm it500}$  is the temperature by adopting iteration steps of 50, 100, or 500 orbits, respectively.

## 2.6 Appendix

#### **2.6.1** Tests of iteration steps

We compare the midplane temperature after 2000 planetary orbits by implementing iteration steps of 50 orbits, 100 orbits, or 500 orbits in Figure 2.10. We show two case of  $3M_{\rm J}$  at 4 au (left) and  $3M_{\rm J}$  at 30 au (right). The differences between the iteration step of 100 orbits and 50 orbits displayed by blue lines are small, especially at the gap regions, the normalized temperature difference  $\Delta T/T_{\rm it100} \sim 0$  and the maximum is < 0.1. On the other hand, the differences between the iteration step of 100 orbits and 500 orbits show relatively larger fluctuations around 0. Therefore, the iteration step of 100 orbits basically is able to reproduce the iteration step of 50 orbits, whereas the iteration step of 500 orbits could not reproduce the iteration step of 100 orbits very well. Meanwhile, we acknowledge that the thermal relaxation time can vary more than several magnitudes in different disk radii (Malygin et al., 2017; Pfeil & Klahr, 2019) but our model can not capture this. Nevertheless, due to the limit of computing capability, we think adopting 100 orbit as the iteration step is suitable for our studies.

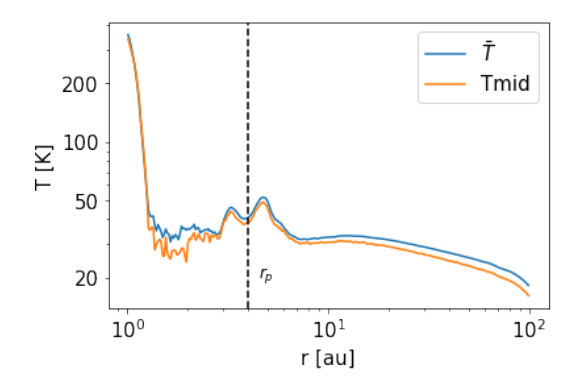


**Figure 2.11:** Comparison of midplane temperature and the density-weighted vertical averaged temperature from RADMC3D simulations of  $3M_{\rm J}$  at 4au over 100 orbits.

## 2.6.2 Comparisons between midplane temperature and densityweighted vertical averaged temperature

We compare the midplane temperature and the density-weighted vertical averaged temperature from RADMC3D simulations of  $3M_{\rm J}$  at 4au over 100 orbits in Figure 2.11. The density-weighted vertical averaged temperature is calculated by

$$\bar{T}(r) = \frac{\int \rho(r,z)T(r,z)dz}{\int \rho(r,z)dz}$$
 (2.5)

where T(r,z) is the azimuthal average temperature.

Overall, the density-weighted temperature is not significantly different from the midplane temperature as the volume density is much higher in the midplane than on the surface. Especially the gap region temperature is very similar. The strongest difference is in the shadowing region where the midplane temperature is lower than the weighted temperature for up to 10K. This is because the shadowing effect is strongest for the midplane. As the weighted temperature has a contribution from the surface temperature, which is not heavily affected by the shadowing effect, it makes the weighted temperature higher.

## 2.6.3 Gas density of planets at 10au and 30au

Figure 2.12 and 2.13 show the 2D gas density map of gaps opened by  $3M_{\rm J}$ ,  $1M_{\rm J}$ ,  $100M_{\oplus}$ , and  $10M_{\oplus}$  planets at 10 au and 30 au, respectively. The results of iteration and non-iteration are displayed in the upper and lower panels, respectively.

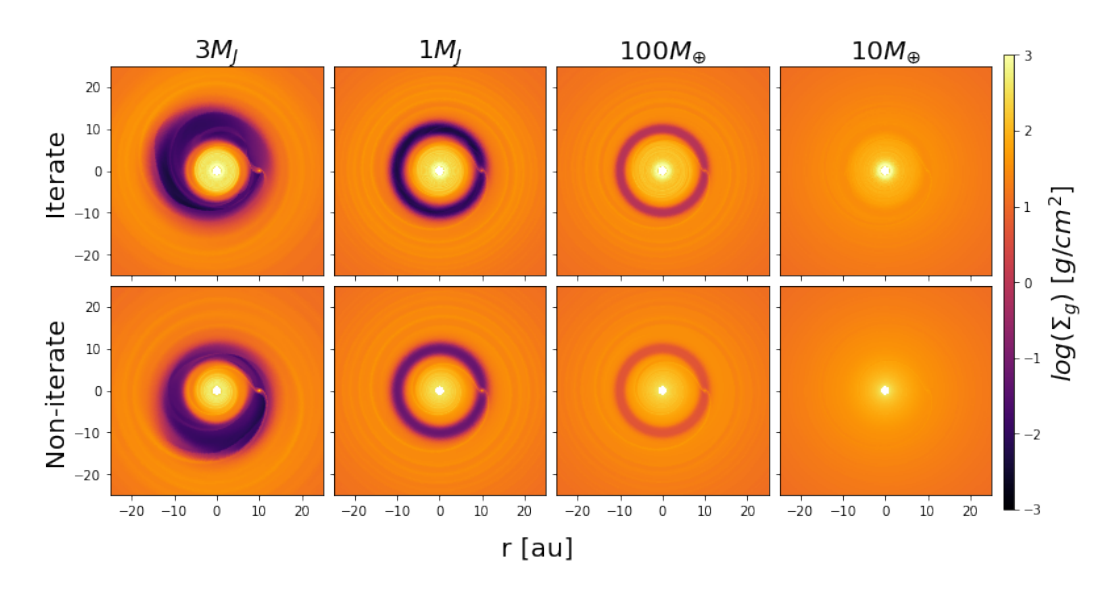


**Figure 2.12:** Similar to Figure 2.2 bur for planets at 10 au.

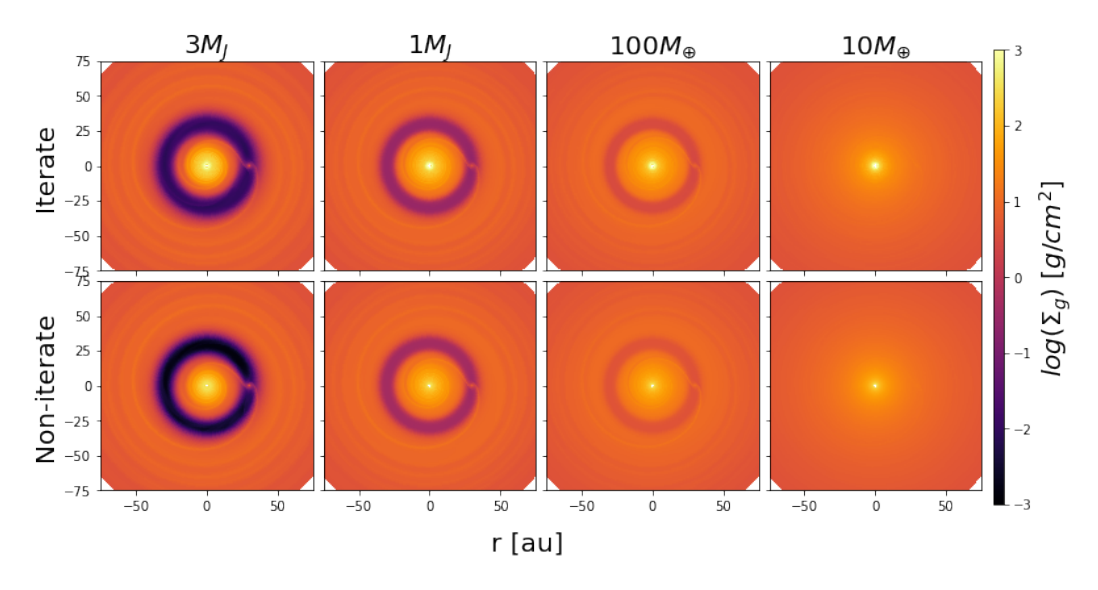


**Figure 2.13:** Similar to Figure 2.2 bur for planets at 30 au.

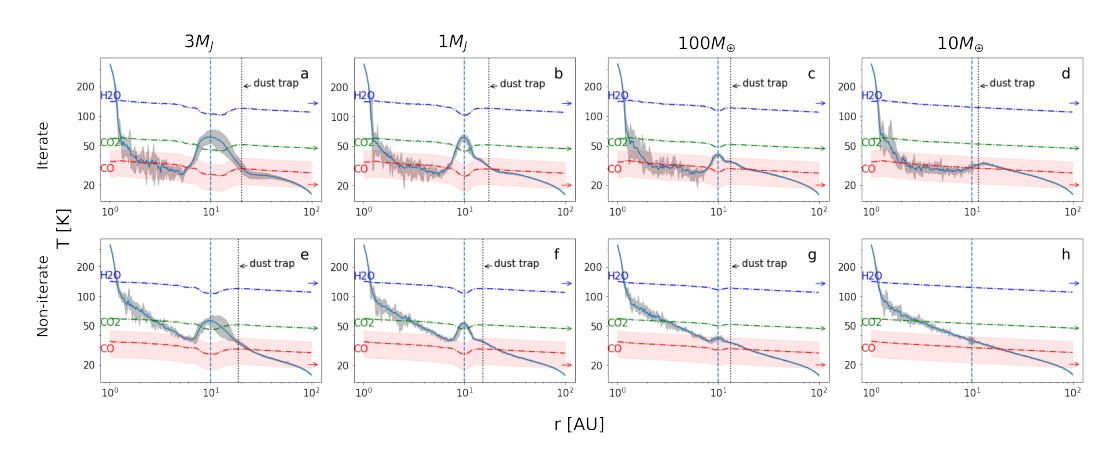


**Figure 2.14:** Similar to Figure 2.4 but for planets at 10 au.

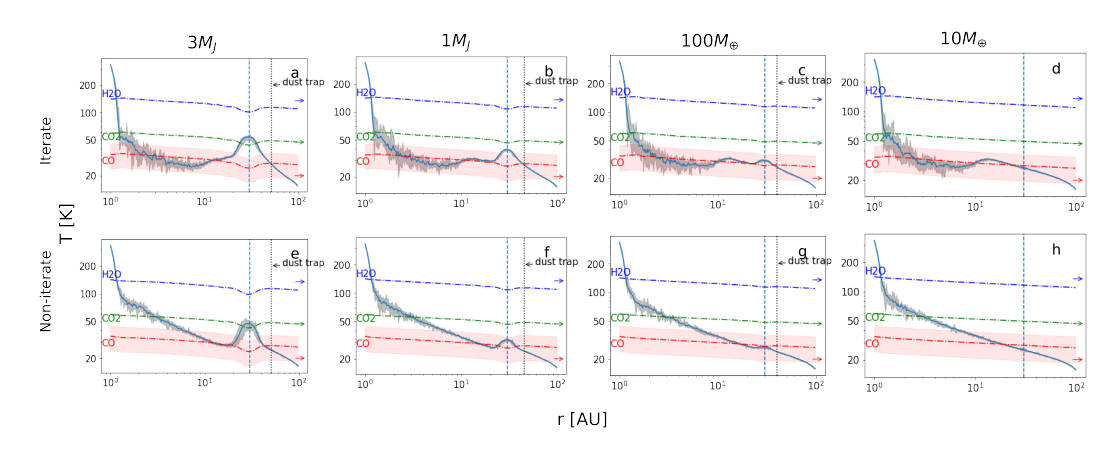


**Figure 2.15:** Similar to Figure 2.4 but for planets at 30 au.

## 2.6.4 Temperature of planets at 10au and 30au

Figure 2.14 and 2.15 show the midplane temperature as a function of disk radius when planet location is  $r_{\rm p}=10$  and 30 au, respectively.

# **Chapter 3**

# Planet-induced Gas and Dust Substructure Feedbacks on Disk Thermal Structure

## **Abstract**

Protoplanets can interact with their natal disks and form gas and dust substructures in disks. How these planet-induced substructures (e.g., gaps and rings) affect the disk temperature, and how that in turn affects the substructures, remains unclear. We aim to study disk substructures and thermal structure self-consistently, and to explore their impact on the volatile distribution. To this end, we perform multi-fluid hydrodynamical simulations and radiative transfer simulations in an iterative method to study planet-disk interactions. We find that the temperature in a structured disk, due to giant planet formation, significantly deviates from that of a smooth disk. The midplane temperature in gaps can increase by tens of Kelvin, causing volatile sublimation, and radial shifts and multiplication of icelines. Meanwhile, comparing our multi-dust models with previous gas-only models, we find that multi-dust model produces slightly shallower gaps with temperatures about 10 K higher than those of a gas-only model. Multi-dust model also shows that the temperature at dust rings formed by pressure bumps can drop by several Kelvin and act as a volatile freeze-out region. Nevertheless, the ice distribution is not significantly affected by whether the models include dust or not. In addition, we investigate the effect of varying viscosity. The disk midplane is about 10 K warmer when increasing  $\alpha$  from  $10^{-4}$  to  $10^{-2}$ . However, increasing viscosity suppresses gap opening and decreases the gap temperature enhancement. Therefore, there is no simple correlation between the iceline locations and viscosities. In addition, we provide a potential observational strategy to test the gap temperature change with ALMA observations.

## 3.1 Introduction

High-resolution observations have revealed that protoplanetary disks (PPDs) are highly structured, displaying gaps, rings, spirals, and asymmetries (Andrews et al., 2018b; Long et al., 2018; Öberg et al., 2021). Some studies have attempted to measure disk temperatures in both radial and vertical directions using images and line profiles (Fedele et al., 2016; Calahan et al., 2021). Additionally, recent observations have reported non-smooth radial brightness temperature profiles, suggesting that gas and dust temperatures in disks may not be radially smooth (?Leemker et al., 2022; Law et al., 2024). However, whether these disk substructures play a significant role in shaping the disk temperature remains an open question.

Monte Carlo Radiative Transfer (MCRT) simulations are used to model the disk temperature structure. Compared to other radiative transfer methods, MCRT has advantages in accurately handling dust opacities, absorption, scattering, and complex disk geometries. For example, by assuming a gap density profile induced by Jupiter in the solar nebula, Turner et al. (2012) used MCRT to find an increase in gap temperature; while Broome et al. (2023) examined how the gap temperature deviates from that of a disk without a gap by considering stellar radiation and viscous heating, though they also assumed fixed gap density profiles. In both cases, the gas and dust density structures in the MCRT simulations were analytically prescribed and fixed in time.

In a more realistic simulation, substructures may alter the disk temperature, and changes in disk temperature may, in turn, feedback on disk substructures. For example, the gap-opening process is influenced by the disk scale height (Fung et al., 2014; Kanagawa et al., 2015; Duffell, 2020), which is determined by the disk temperature. Another example is that temperature sets the locations of volatile icelines, which are crucial for planet and planetesimal formation (Öberg et al., 2011; Schoonenberg & Ormel, 2017). Icelines may lead to the formation of dust gaps or rings. Observations by Zhang et al. (2015) found that the dust continuum gaps in HL Tau align with several volatile iceline locations. Additionally, Pinilla et al. (2017) used dust evolution simulations to show that icelines can induce rings or gaps in scatter

light or dust continuum observations, depending on viscosity. However, later surveys (Huang et al., 2018; Long et al., 2018) found no simple one-to-one correlation between the radial locations of rings or gaps and expected iceline positions, assuming a smooth and monotonically decreasing radial temperature profile. These model and observation comparisons do not account for the possibility that a structured disk may have a structured temperature profile rather than a smooth one. Therefore, it is crucial to study disk temperature and disk substructures simultaneously and self-consistently.

Recently, Chen et al. (2023, hereafter C23) proposed a novel iterative hydrodynamical (HD) and MCRT method to study how a planet-induced gap can affect disk temperature. Simultaneously, the temperature change alters the disk scale height, further influencing the gap-opening process. They showed that in a gap induced by a Jovian planet at a few au (e.g., 4au) to a few tens of au (e.g., 30au), the midplane temperature can increase significantly, by up to several tens of Kelvin. As a result, volatiles such as CO ice can sublimate, leading to multiple CO icelines and new iceline locations, which differ significantly from the number and position of icelines in a smooth disk. Furthermore, the complex iceline distribution suggests a complex C/O ratio across the disk, challenging the canonical C/O ratio derived from a smooth disk in Öberg et al. (2011). However, C23 did not account for dust dynamics during the iteration process.

In this paper, we aim to use HD-MCRT simulations with multiple dust species to investigate how dust and gas substructures generated by planet-disk interactions influence the disk temperature structure and volatile distribution. Studying gas and dust distributions simultaneously is crucial, as dust and gas interact with each other. Dust densities are affected by gas drag, which alters the dust distribution and dust-to-gas ratio (Weidenschilling, 1977). Meanwhile, dust distribution and opacities strongly influence both dust and gas temperatures. These temperature changes, in turn, affect the gas density structure of the disk.

This paper is organized as follows. In Section 3.2, we describe our method of iterating HD and MCRT simulations with multiple dust species. In Section 3,

we present our results, comparing our new method (which includes multiple dust species) with our previous approach (which did not) and exploring the effects of different viscosities using the new method. Section 4 discusses model simplifications and potential observational strategies to test our model. We summarize our findings in Section 5.

## 3.2 Methods

We combine hydrodynamical (HD) and Monte Carlo radiative transfer (MCRT) simulations and iterate them to study how substructures can affect disk thermal structures. We modify our previous iteration model in Figure 1 in C23 to include dust of different grain sizes in both hydrodynamics and radiative transfer. In our previous model, we did not include dust in HD simulations and simply assumed that  $0.1 \,\mu m$  dust was well mixed with gas in MCRT simulations.

Including multiple dust species is important: first, in the HD simulation, dust may decouple from the gas, depending on the Stokes number (St), which is defined as

$$St = \frac{\pi}{2} \frac{\rho_s a}{\Sigma_g},\tag{3.1}$$

where  $\rho_s$  is the internal density of the dust particle, a is the dust grain size, and  $\Sigma_g$  is the gas surface density.

Large dust grains have larger St and can drift radially faster than small dust grains. Therefore, large grain sizes (e.g., 1 mm) can be distributed very differently from small grain sizes and gas. So we need to directly obtain dust density structures from HD simulations instead of assuming a well-mixed dust and gas density structure. Second, in MCRT, different grain sizes have different opacities and different levels of dust settling in disk vertical directions. Thus, the implementation of dust can alter the disk temperature, which can affect the planetary gap-opening process and further change the temperature at the gap as a consequence.

We show our workflow for implementing multiple dust species into our iteration method in Fig. 3.1. This workflow is modified from the workflow in C23

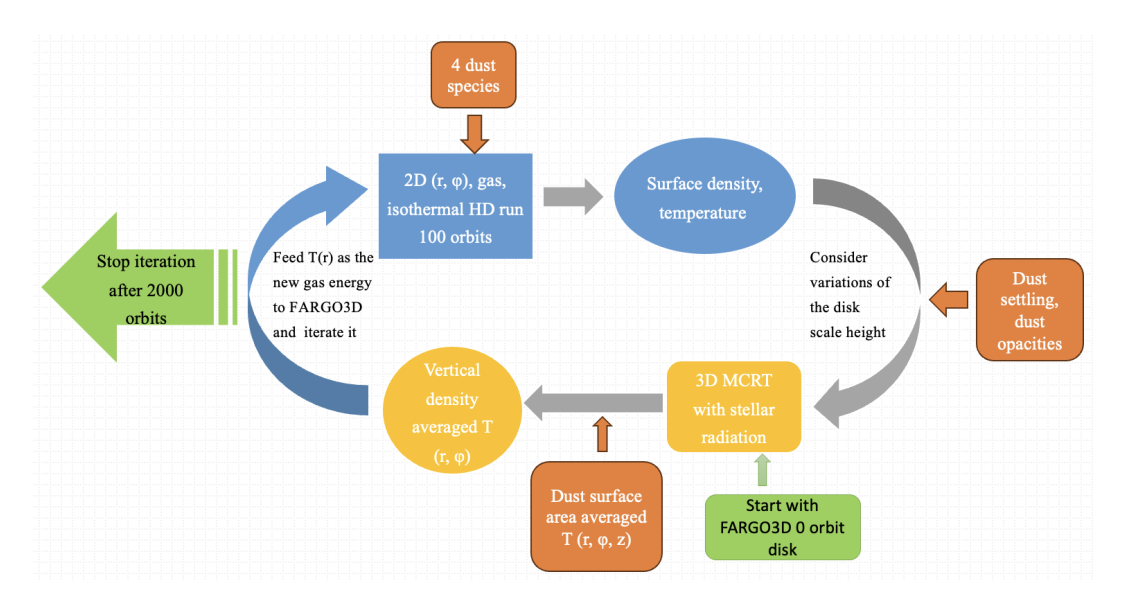


**Figure 3.1:** Workflow of our iteration method with the implementation of multiple dust species. The workflow is modified from the workflow in C23 by adding multiple dust species in both HD and MCRT simulations.

by adding multiple dust species in both HD and MCRT simulations. Basically, our iteration method can be understood as three main steps. First, we run HD simulations to get the density structure without temperature evolution. Second, we input the density from HD into MCRT simulations to get the temperature structure. Thus, there is no density evolution in MCRT. Third, we post process the MCRT dust temperature to get gas temperature and feed it into the HD simulation. Then we repeat the first two steps above. We discuss more about these three steps in the following sections. We perform the iteration process every 100 planetary orbits and iterate to 2000 orbits in total. We also carry out parameter studies of different planet masses  $M_p$ , planet locaitons  $r_p$ , and  $\alpha$  viscosities (shown in Table 3.1).

## 3.2.1 Hydrodynamical setups

For the setup of HD simulations, Table 3.1 summarizes our parameter space. We use the same disk and planet setup as C23. The entire disk extends from 1 to 100 au. We fix the planet on a circuler orbit. We run multi-species FARGO3D simulations with gas plus four different grain sizes (Weber et al., 2019) in 2D, radial and azimuthal directions  $(r, \phi)$ . Readers are referred to the governing equations in Section 2.1 of Weber et al. (2019). We use four grain sizes  $a_i$  of 0.1  $\mu m$ , 2.2 $\mu m$ , 46  $\mu m$ , and 1

**Table 3.1:** FARGO3D main parameters. Parameters in each column below the nineth row in this table are corresponding to the cases of planet location  $r_p = 4$ , 10, or 30 au, respectively. Different  $\alpha$  studies are only for cases of  $100M_{\oplus}$ .

parameters	values				
$\overline{M_p}$	$3M_{\rm J}$ , $100M_{\oplus}$ , $10M_{\oplus}$				
$a_i[\mu m]$	0.1, 2.2, 46, 1000				
SigmaSlope		-1			
FlaringIndex		0.25			
$M_{\star}$ $[M_{\odot}]$		1.0			
$\rho_{solid}$ [g/cm <sup>3</sup> ]		3.7			
$\gamma_{ m dust}$		-3.5			
$oldsymbol{arepsilon}$		0.01			
$r_0 = r_p \text{ [au]}$	4	10	30		
$r_{min} [r_0]$	0.25	0.1	0.033		
$r_{max}[r_0]$	25	10	3.3		
Aspect Ratio	0.04	0.05	0.066		
$\Sigma_0[M_\star/r_0^2]$	$1.8^{-4}$	$4.5^{-4}$	$1.34^{-3}$		
$N_{r,HD}$	580	460	350		
$N_{\phi,HD}$	790	630	480		
$\alpha$ (for $100\mathrm{M}_{\oplus}$ )	10-	$-2, 10^{-3},$	$10^{-4}$		

mm and the number density of grain sizes follow a power law  $n(a) \propto a^{-\gamma_{\rm dust}}$ ,  $\gamma_{\rm dust} = 3.5$ . The internal density of grains is  $3.7g/cm^3$ . For simplification, we refer to our previous model with only gas in hydro simulations and with 0.1  $\mu m$  dust in MCRT simulations as "Model G" and our new model with multiple dust species as "Model D". We include dust feedback on the gas, as well as dust diffusion, in our simulations.

Additionally, we study the effect of different viscosities in Model D. The level of disk turbulence can affect the HD simulations in several ways, including gap opening and dust diffusion. Also in MCRT simulations, different  $\alpha$  affects dust settling. Inspired by recent turbulence measurements in several disks (Flaherty et al., 2015; Pinte et al., 2016; Flaherty et al., 2018; Teague et al., 2018b; Dullemond et al., 2018; Flaherty et al., 2020), we adopt  $\alpha = 10^{-2}$ ,  $10^{-3}$ , and  $10^{-4}$ .

For boundary conditions, we use a damping prescription to minimize reflections near the boundaries. Similar to Pyerin et al. (2021), for the radial boundaries, we adopt power-law extrapolation for densities and Keplerian extrapolation for azimuthal velocities for both dust and gas. Regarding the radial velocities for gas and dust, we adopt symmetric inner and outer boundaries to conserve the disk mass. Periodic boundaries are imposed in the azimuthal direction.

#### 3.2.2 Monte Carlo Radiative Transfer setup

We use the 3D Monte Carlo radiative transfer code, RADMC-3D (Dullemond et al., 2012), to calculate the disk temperature structure. For the setup of the MCRT, we summarize our parameter choices in Table 3.2, which are mainly similar to the parameter choices in C23. In this project, we azimuthally average the model to minimize the effect of poor photon statistics, except for cases developing eccentric gaps, such as  $3M_{\rm J}$  at 4 au and  $3M_{\rm J}$  at 10 au with  $\alpha=10^{-3}$  and  $\alpha=10^{-4}$ , respectively. The star and disk setup are the same as the counterparts in C23 unless the treatment of dust which we discuss below.

As we have four dust species, ranging from 0.1  $\mu m$  to 1 mm, we calculate the corresponding dust opacity for different grain sizes using the optool package (Dominik et al., 2021). We input the dust surface densities and the evolving gas scale height from HD simulations into MCRT simulations. Following equation (19) in Fromang & Nelson (2009), the vertical distribution of the dust is calculated from gas scale height,  $\alpha$  and St. This is a steady state dust vertical distribution when turbulent diffusion balances dust settling. In other words, a larger grain size or a smaller  $\alpha$  viscosity leads to a smaller dust scale height. As a result, we can extend the 2D dust surface density into a 3D dust column density. We consider isotropic scattering for dust.

## 3.2.3 Post possessing between radiative transfer and hydro

From the MCRT in Model D, we obtain the dust temperature for each grain size in each grid cell,  $T_{dust,i}(r,\phi,z)$ , where i represents the i-th dust species. However, in the HD simulations, we need the gas temperature in the HD grid cell  $(r,\phi)$ . Therefore, when feeding the MCRT temperature to the HD simulations, we carry out the following processes.

First, we calculate the dust surface-area-averaged temperature in each grid cell,

Table 3.2: RADMC3D parameters.

parameters	values
$M_{\star}$ $[M_{\odot}]$	1
$R_{\star}$ [ $R_{\odot}$ ]	1.7
$T_{\star}$ [K]	4730
$N_{photon}$	$10^{8}$
$N_{r,MCRT}$	256
$N_{\phi,MCRT}$	1
$N_{\theta,MCRT}$	53

 $T_{dust}(r,\phi,z)$ .

$$T_{dust}(r, \phi, z) = \frac{\sum_{i} A_{i} n_{i}(r, \phi, z) T_{dust,i}(r, \phi, z)}{\sum_{i} A_{i} n_{i}(r, \phi, z)}$$
(3.2)

where  $n_i$  is the dust number density of species i,  $A_i = 4\pi a_i^2$ , i=1,2,3,4. Note that for Model G, since we only have one dust species, we do not need to do the above averaging.

Second, the surface-area-averaged dust temperature is a good approximation for the gas temperature when gas and dust particles are well mixed (Facchini et al., 2017). Therefore, we assume  $T_{dust}(r, \phi, z) = T_{gas}(r, \phi, z)$ .

Third, we calculate a vertically-averaged density-weighted gas temperature  $\bar{T}_{gas}(r,\phi)$  from  $T_{gas}(r,\phi,z)$  by using

$$\bar{T}_{gas}(r,\phi) = \frac{\int T_{gas}(r,\phi,z)\rho_{gas}(r,\phi,z)dz}{\int \rho_{gas}(r,\phi,z)dz}.$$
(3.3)

Fourth, we input  $\bar{T}_{gas}(r,\phi)$  as the iterative gas temperature for the next round of 2D HD run. Note that we also refer to  $\bar{T}_{gas}(r,\phi)$  as the iterative temperature  $T_{\text{iterate}}$  for simplicity in the following sections.

## 3.3 Results

We compare the results of our iteration methods with and without multiple dust species. To this end, we present the results of general disk modeling, including density structure, temperature structure, and iceline locations.

#### 3.3.1 Effects of dust

In this section, we present and analyze the results obtained from Model G in C23 and Model D (this work) with the same viscosity  $\alpha = 10^{-3}$ .

## 3.3.1.1 Density maps

We show the surface densities of  $100M_{\oplus}$  at 10au at 2000 planetary orbits from the Model G (left) and Model D (right) in Fig. 3.2. For the gas surface density, both models show similar simulation features in the 2D surface density map, such as spirals and concentric gaps. For dust densities in Model D, the 2D density maps show that dust gaps across four different grain sizes are concentric with  $100M_{\oplus}$  at 10au. Similar to Rosotti et al. (2016), as the grain size increases, the dust gap becomes deeper and wider (as shown in the 1D radial profile in Model D). Specifically, the gap in 1mm dust is about 5 au (0.5  $r_p$ ) wide, which is roughly 2 times wider than the 0.1  $\mu m$  one. Additionally, the former could be very depleted ( $< 10^{-6} g/cm^{-2}$ ) in the gap center, while the latter is only about 10 times lower than its initial values. This is expected, as the small grains couple well with the gas and follow the gas distribution, while large grains either experience radial drift inward inside the gap or get trapped in pressure maxima outside the gap. Thus, large grains are prevented from filling the gap.

## 3.3.1.2 Radial profiles of density, aspect ratio and temperature

We show the comparison of the gas surface density, disk aspect ratio, and disk iterative and midplane temperature as a function of disk radius of  $100M_{\oplus}$  at 10au at 2000 orbits obtained from Model G and Model D in Fig. 3.3. We remind the reader that, as explained in Section 3.2.3, the iterative temperature  $T_{\text{iterate}}$  is the temperature used for each HD step. It is a vertically-averaged, density-weighted temperature. Another temperature we are concerned about is the midplane temperature  $T_{mid}$  because ices of volatiles mainly locate at the midplane.

In the gap region, we find that the gas gap is shallower when calculated by Model D than by the Model G. The former is  $\Sigma_{gas}/\Sigma_{gas,0}=2.5\times10^{-2}$  at the gap center, while the latter is  $4\times10^{-2}$ . This is explained by the iterative temperature

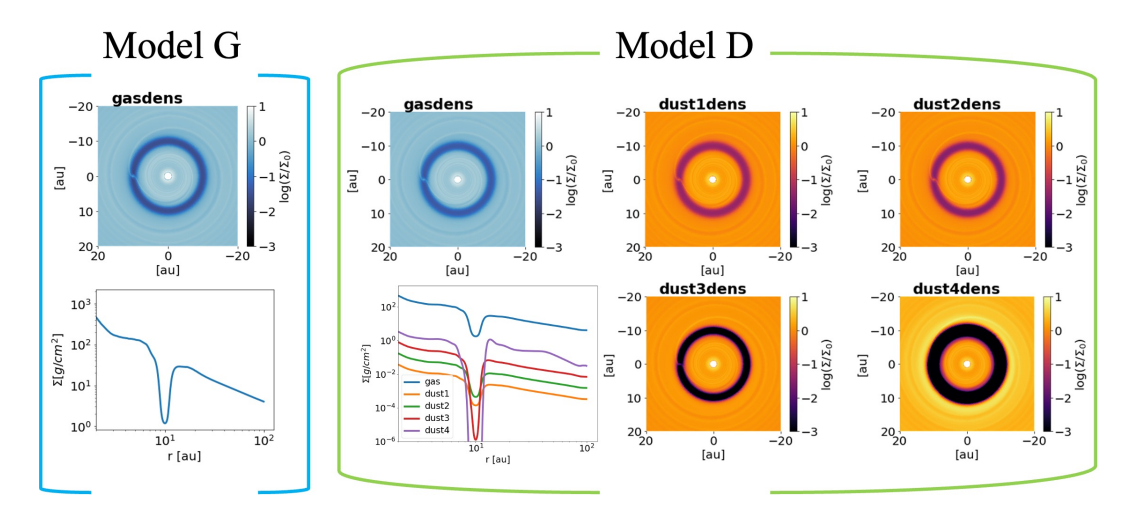


**Figure 3.2:** Comparisons of surface density between the Model G (left) and Model D (right) with iterations for  $100M_{\oplus}$  at 10au at 2000 orbits. For four dust species in Model D, with panels named from dust1dens to dust4dens, they are  $0.1\mu m, 2.2\mu m, 46\mu m$  and 1mm, respectively. 2D surface density maps are shown in units of normalized densities, while the 1D radial surface density profiles are shown in absolute values.

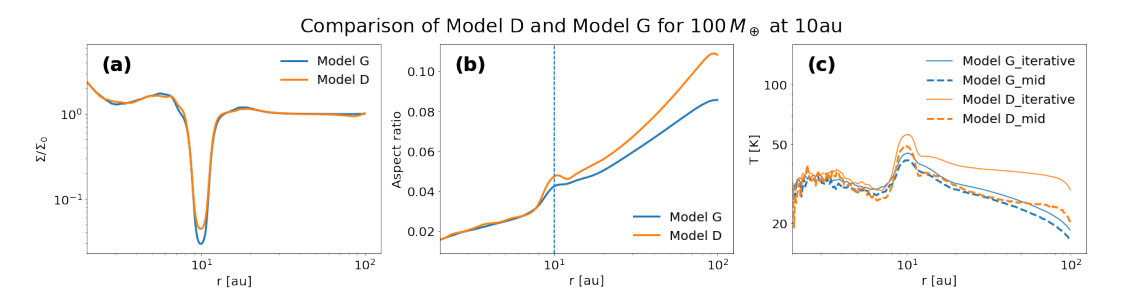


**Figure 3.3:** Radial profiles of gas surface density (a), gas aspect ratio (b), and temperature (c) of iterative process  $T_{\text{iterate}}$  (solid lines) and midplane  $T_{mid}$  (dashed lines) of  $100M_{\oplus}$  at 10au at 2000 orbits obtained from Model G and Model D, respectively.

 $T_{\text{iterate}}$  at the gap being about 10 K higher in Model D than in Model G, which makes the gas aspect ratio slightly increase from 0.045 (Model G) to 0.05 (Model D). A higher aspect ratio makes gap opening more difficult (Crida et al., 2006). We also find that  $T_{mid}$  is about 10 K higher in Model D than in Model G in the gap region.

In the regions outside the gap (Fig. 3.3(c)), Model D presents a similar  $T_{\text{iterate}}$  as Model G for  $r < r_{\text{p}}$ . We also note that  $T_{\text{iterate}}$  is approximately 10 K higher in Model D than in Model G in regions outside the gap,  $r > r_{\text{p}}$ , whereas the difference in  $T_{mid}$  is smaller.

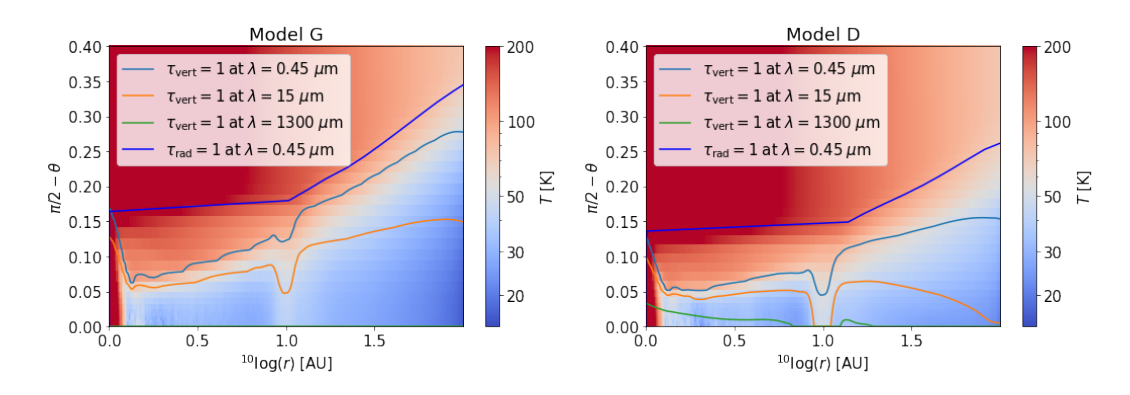


Figure 3.4:  $\tau = 1$  surfaces at different wavelengths of Model G (left) and Model D (right) of  $100M_{\oplus}$  at 10au at 2000 orbit, respectively. Background colormap is the dust temperature in Model G and dust surface area averaged temperature in Model D. Vertical and radial  $\tau = 1$  surfaces at different wavelengths are shown In lines with different colors.

Inside Model D,  $T_{\text{iterate}}$  at the gap center is about 55 K, which is about 10 K higher than the outer gap edge (14 au) and about 25 K higher than the inner gap edge (7 au). The inner gap edge is cooler because the inner dust rim at 1 au is puffed up, creating a shadowed region that extends up to about 10 au.

We check the gap opening in other  $M_p$  and  $r_p$  cases and find that they show the same trend as  $100M_{\oplus}$  at 10au, where the gap depth in Model D is shallower than that in Model G. There are some exceptions for cases with the presence of eccentric gaps caused by  $3M_J$ . In that case, the gas gap depth of Model G is shallower than that in Model D. This is because the more eccentric gap in Model G creates a denser streamer, which enhances the azimuthal average density at the gap.

To better understand the temperature differences between Model G and Model D, we show in Fig. 3.4 a 2D cut of the temperature structure with  $\tau=1$  surfaces at different wavelengths. Dust absorbs stellar photons at short wavelengths (optical, NIR;  $\lambda=0.45\,\mu\mathrm{m}$  is shown for reference) and re-emits at longer wavelengths (mid-IR to mm;  $\lambda=15\,\mu\mathrm{m}$  and  $1300\,\mu\mathrm{m}$ ). In Model G, the radial  $\tau_{\mathrm{rad}}=1$  and vertical  $\tau_{\mathrm{vert}}=1$  optically thick surfaces at  $\lambda=0.45\,\mu\mathrm{m}$  are higher, meaning that fewer photons at the stellar intensity peak wavelength can penetrate into the disk. In contrast, at  $\lambda=1.3\,\mathrm{mm}$ , Model G is optically thin, whereas Model D is optically thick. This results from the larger long-wavelength opacity of mm-grains,

which are absent in Model G. The lower opacity makes it easy for cooling radiation to escape in Model G. As a combined effect, Model G generally has a lower temperature than Model D at the same grid cell in the disk. However, it is important to note that for the midplane temperature  $T_{mid}$ , the difference between Model G and Model D is relatively small. On the other hand, the difference between Model G and Model D is larger in the vertically integrated, density-weighted temperature  $T_{iterate}$ .

#### 3.3.1.3 Temperature at dust rings

We also study how dust rings, formed by dust trapping at pressure maxima, can affect disk temperature.

For the case of  $3M_{\rm J}$  at 30au in Model D, a strong mm dust-trap ring is present at the outer edge of the gap (Pinilla et al., 2012b,a) at  $r \sim 50-60$  au. In contrast, no dust ring is present in Model G. This is because Model G only considers 0.1  $\mu m$  dust, which is assumed to follow the gas density, and there is no obvious gas ring at the outer gap edge.

Figure 3.5 shows a 2D mm dust density map in Model D (panel (a)) and the radial midplane and sublimation temperature (Hollenbach et al., 2009) profiles (panel (b)) obtained from Model G and Model D. At the dust trap location in Fig. 3.5(a), the mm dust surface density increases by more than 100 times from the initial condition, leading to a higher optical depth. As a result, the mm dust ring induces an approximately 5 K drop in  $T_{mid}$  compared to cases without a dust trap at the same radius in Model D, though the former is still nearly the same as  $T_{mid}$  in Model G. However, this temperature drop at the dust ring is small and likely difficult to detect in ALMA observations. We note that Zhang et al. (2021a) also found a disk temperature drop at the dust ring, although they directly assumed a Gaussian density profile for the width and peak of the dust ring.

To confirm whether the temperature drop in the dust rings is due to the higher optical depth of the dust ring or the shadowing effect caused by the puffed-up disk scale height at the gap (with temperature enhancement), we performed a test using a puffed-up disk model without dust surface density enhancement at the previous dust

ring location. We found that the temperature change at the dust ring location was negligible. In other words, the temperature drop at the dust ring is indeed primarily due to the optical depth effect of the dust ring.

Meanwhile,  $T_{\text{sub}}$  is about 5 K higher in Model D than in Model G, while the CO iceline shifts only slightly, moving a few au closer to the star. As  $T_{mid}$  is lower than the  $T_{\text{sub}}$  of CO at the dust ring, the dust ring can act as a volatile freeze-out region, similar to the findings in Alarcón et al. (2020). In addition, the hot gap can act as a highly active volatile sublimation region. Consequently, a significant amount of gas-phase volatiles diffuse to the outer gap edge and freeze out at the dust ring. This combination of a hot gap and a cold ring could provide a favorable environment for efficient pebble and planetesimal growth.

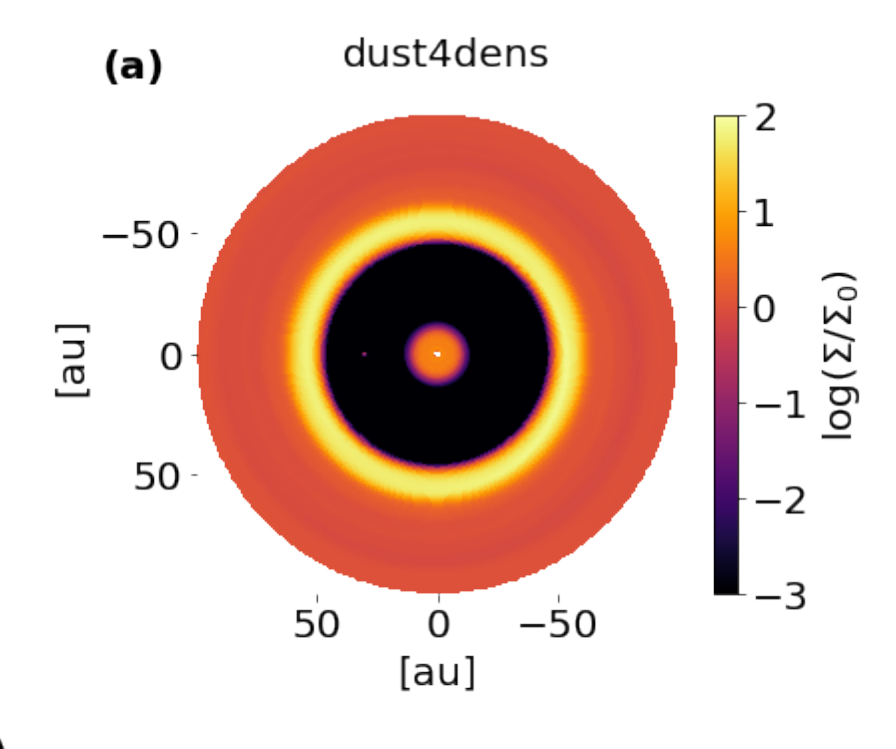
#### 3.3.1.4 Effects on icelines

In Fig. 3.6, we show the midplane and sublimation temperature for different planet masses  $(M_p)$  at  $r_p=30$  au for the Model D case. Since  $M_p=10M_\oplus$  is unable to open a deep gap, the temperature profile is similar to the smooth disk. As  $M_p$  increases, the gap region becomes hotter, which is consistent with the results in C23.  $T_{mid}$  is about 25 K at  $r_p$ . The midplane temperature of  $3M_J$  at 30 au is about 20 K higher than that of  $100M_\oplus$  at 30 au, and the latter is about 10 K higher than that of  $10M_\oplus$  at 30 au. The sublimation temperature of volatiles (e.g. CO) gets lower in gaps as  $M_p$  increases. Overall, the temperature contrast between gap and outside gap shows that a Saturn mass or even more massive planet can significant change the disk temperature structure.

As the midplane temperature of the disk and the pressure-dependent sublimation temperature of volatiles can be obtained from our models, we can proceed to investigate the behaviour of volatile icelines. Figure 3.7 shows a comparison of the radial H<sub>2</sub>O, CO<sub>2</sub>, and CO ice distribution for the case of Model G and Model D.

Overall, the iceline locations from these two models are similar. This is because we mainly focus on the ice distribution in the midplane, and the  $T_{mid}$  values from Model G and Model D are not significantly different, as shown in Fig. 3.3 (panel c). Specifically, beyond 10 au, the number of icelines for a given volatile

3.3. Results 113



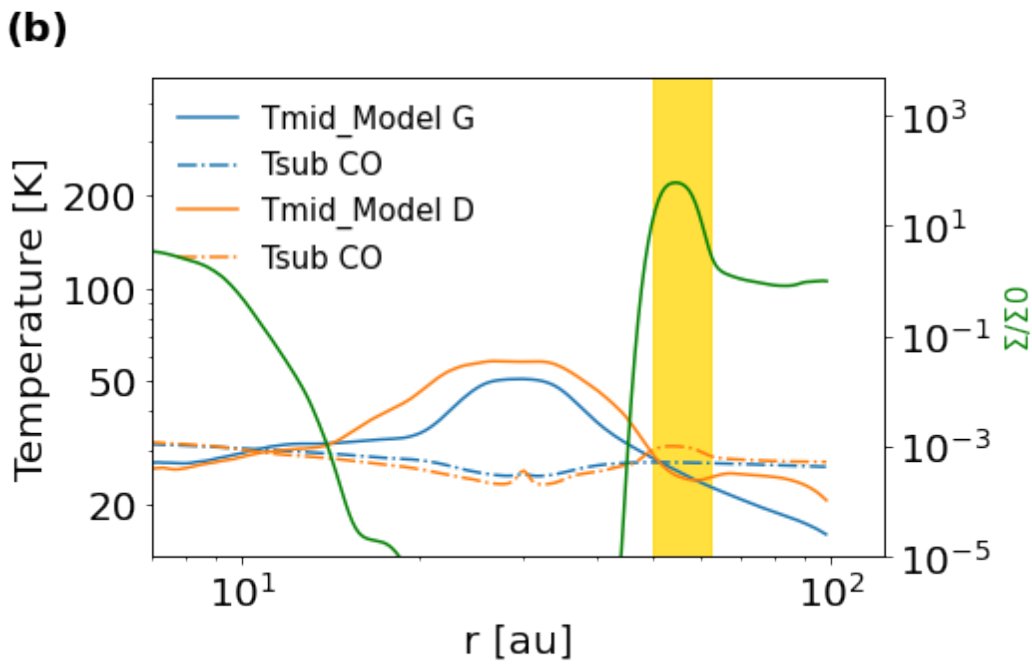


**Figure 3.5:** Dust trap in mm size grains of  $3M_{\rm J}$  at 30au at 2000 orbits. Panel (a) shows surface density map of mm dust and panel (b) shows  $T_{mid}$  (solid lines) and  $T_{\rm sub}$  (dashed lines) from Model G and Model D. In panel (b), the green line and the right-hand-side axis represent normalized mm dust density radial profile in Model D and the gold-shaded radius regions correspond to the mm dust ring regions in the density map.

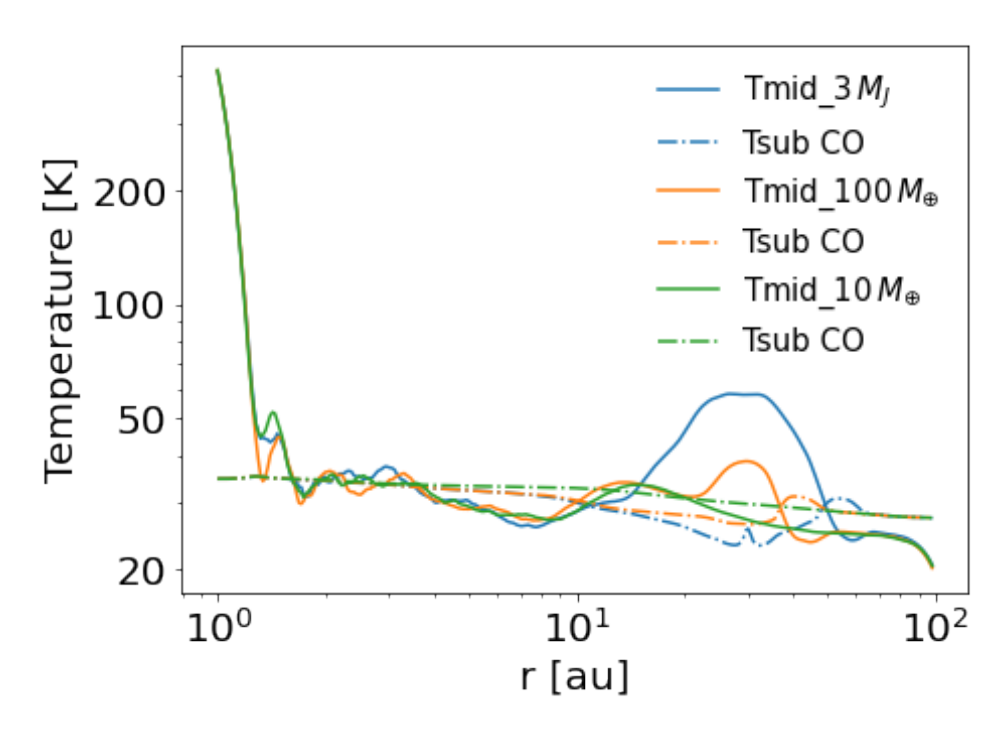


**Figure 3.6:** Miplane (solid) and sublimation (dashed) temperature profiles of different  $M_p$  at  $r_p = 30$  au of Model D

is essentially the same in both Model G and Model D, though their exact locations may differ.

The main differences in the gap regions appear in the case of a 3  $M_{\rm J}$  at 30 au, where Model D exhibits a wider CO<sub>2</sub> sublimation region (green bars are CO<sub>2</sub> ice region) around the planet (marked by vertical cyan dashed lines) compared to Model G. In Model D (the top third of panel (a2)), the CO<sub>2</sub> sublimation region extends from 20 to 40 au. In contrast, in Model G (the top third of panel (a1)), the CO<sub>2</sub> sublimation region ranges from 25 to 35 au. This difference arises because  $T_{mid}$  is higher in the gap regions of Model D than in Model G.

Outside the gap regions, the main differences occur in the inner disk, within the first few au. Although the  $T_{mid}$  values from Model G and Model D in this region differ by only a few Kelvin, the  $T_{mid}$  here is very close to the sublimation temperature of CO. As a result, the CO iceline is highly sensitive to even small differences in  $T_{mid}$  between Model G and Model D. We have more discussions about these compact ice regions in first few au in Section 3.4.3.

3.3. Results 115

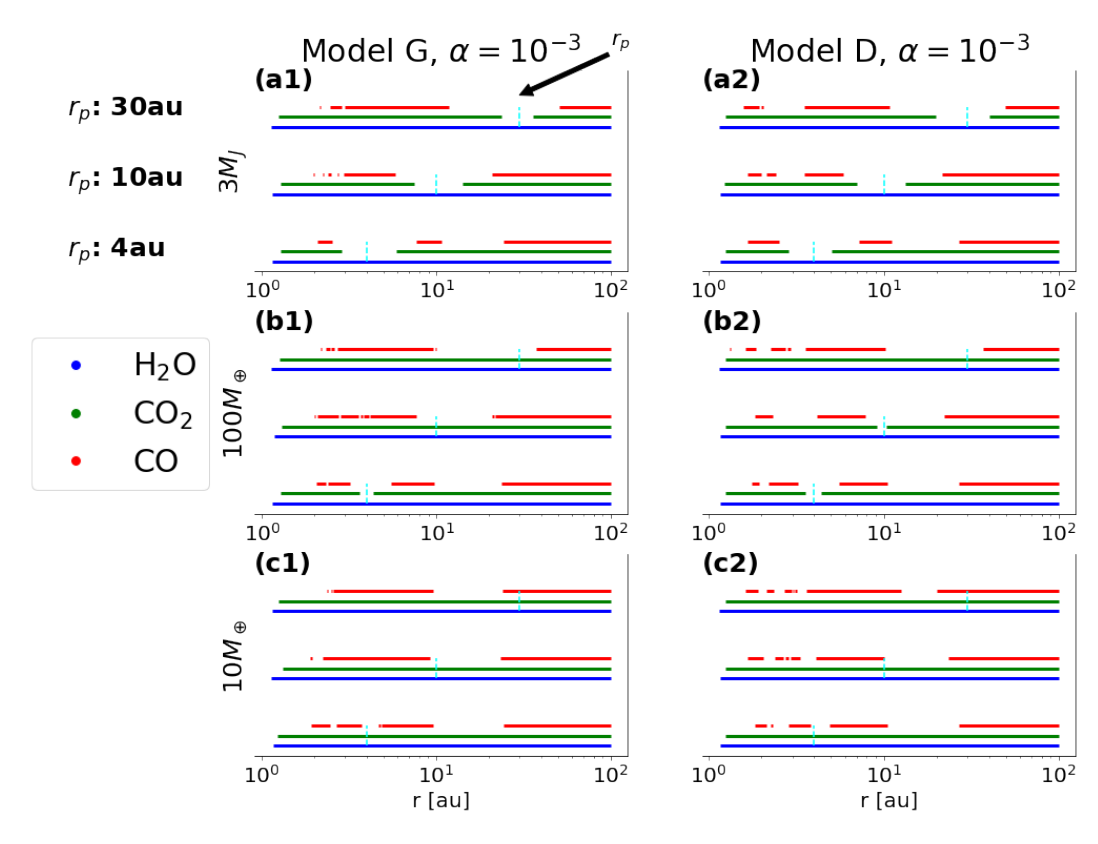


**Figure 3.7:** Comparions of radial ice distribution of  $H_2O$ ,  $CO_2$  and CO obtained from Model G (left) and Model D (right). We show different  $M_p$ ,  $3M_J$ ,  $100M_{\oplus}$  and  $10M_{\oplus}$  from top to bottom. In each panel, from top to bottom,  $r_p$  is 4, 10, and 30 au, respectively. Each bar represents ice existance regions in the midplane. Vertical cyan dashed lines represent the planet location.

### 3.3.2 Effects of different viscosity

Different levels of turbulent viscosity can alter dust settling, which in turn affects the disk temperature. At the same time, turbulence influences the gap-opening process and dust diffusion.

# 3.3.2.1 Disks without planets

When there is no planet in a disk, different turbulence levels can affect dust settling, which in turn changes the height of the  $\tau=1$  surface and impacts the disk's temperature distribution. Figure 3.8 compares the midplane temperature,  $T_{mid}$ , as a function of radius for non-planetary disks with viscosities of  $\alpha=10^{-2},10^{-3}$ , and  $10^{-4}$ . As  $\alpha$  decreases,  $T_{mid}$  becomes lower across the entire disk. The  $T_{mid}$  for  $\alpha=10^{-2}$  is about 10 K higher than that for  $\alpha=10^{-4}$  at  $r\leq 10$  au and a few K higher at larger radii. This trend occurs because lower  $\alpha$  allows for stronger dust

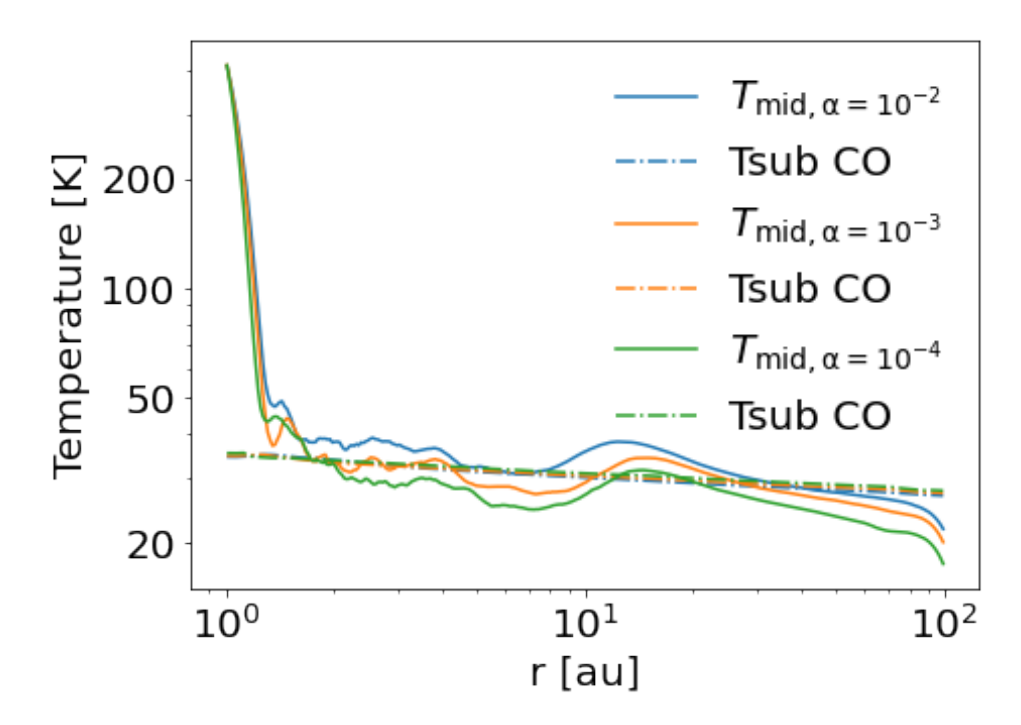


**Figure 3.8:** Radial midplane temperature (solid lines) and sublimation temperature (dashed lines) of Model D in non-planet disks with  $\alpha = 10^{-2}, 10^{-3}$  and  $10^{-4}$ , respectively.

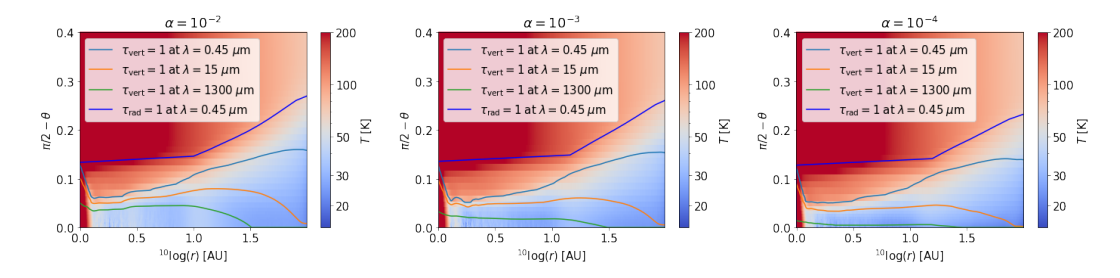


**Figure 3.9:** Similar to Fig. 3.4, but for a planet-free disk setup with different viscosities in Model D. From upper left to bottom right,  $\alpha = 10^{-2}$ ,  $10^{-3}$  and  $10^{-4}$ .

settling, as shown by the lower  $\tau_{\text{vert}} = 1$  surfaces in Fig. 3.9. In lower- $\alpha$  disks, more millimeter-sized dust settles closer to the midplane, which enhances cooling at 1.3 mm and further lowers  $T_{mid}$ .

Note that our radiative transfer simulations do not include viscous heating, we further discuss this effect in Section 3.4.4. Additionally, as shown in Fig. 3.8, the sublimation temperature of a specific volatile is not strongly influenced by variations in viscosity.

As a result, Fig. 3.10 presents the ice distribution in a non-planetary disk with different  $\alpha$  values. The H<sub>2</sub>O and CO<sub>2</sub> icelines are located at approximately 1.15

3.3. Results 117

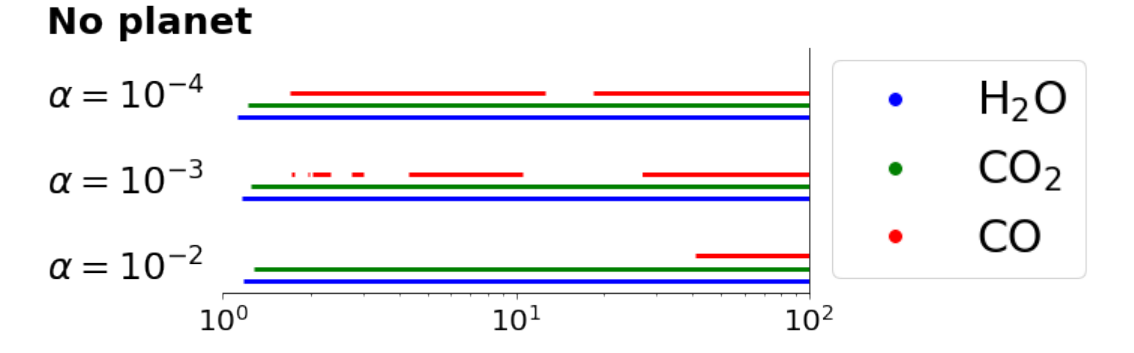


Figure 3.10: Ice plot with no planets in disks with different viscosities.

and 1.3 au, respectively, when  $\alpha = 10^{-2}$ . These icelines shift slightly inward by about 0.05 au for H<sub>2</sub>O and 0.15 au for CO<sub>2</sub> when  $\alpha$  decreases from  $10^{-2}$  to  $10^{-4}$ .

The most significant iceline shift occurs for CO. In the  $\alpha=10^{-2}$  model, the CO iceline is located at  $r\simeq 40$  au. However, for  $\alpha=10^{-3}$ , multiple CO icelines appear at  $r\le 5$  au. This phenomenon arises because, in the shadowed region of the disk (within the first few au), the midplane temperature  $T_{mid}$  for  $\alpha=10^{-3}$  coincidentally approaches the CO sublimation temperature  $T_{sub}$  (as shown in Fig. 3.8). This intriguing scenario suggests that, under specific disk conditions related to density and turbulence levels, a non-planetary disk could host multiple icelines for one specific volatile within its self-shadowed region. For  $\alpha=10^{-4}$ , the inner CO iceline is located at  $r\simeq 2$  au. Additionally, we identify a region devoid of CO ice between 10-30 au for  $\alpha=10^{-3}$  and between 10-20 au for  $\alpha=10^{-4}$ . This occurs because these regions lie just outside the disk's self-shadowed area, allowing CO ice to sublimate before freezing out again at larger disk radii.

## 3.3.2.2 Disks with a 100 $M_{\oplus}$ planet

In our simulations,  $M_p \geq 100 M_{\oplus}$  can open deep gas gaps ( $\Sigma_{\rm g}/\Sigma_{\rm gas,0} < 0.1$ ) in all cases except when  $r_{\rm p} = 10,30$  au at  $\alpha = 10^{-2}$  and  $r_{\rm p} = 30$  au at  $\alpha = 10^{-3}$ . Figure 3.11 shows the normalized radial surface density profiles of gas and dust across the disks at different  $\alpha$  viscosities for a 100  $M_{\oplus}$  planet at 10 au. Two representative dust sizes, 0.1  $\mu$ m and 1 mm, are shown. Overall, as viscosity decreases, the gas and dust in the disks become more structured. The locations of gaps and rings in the dust generally coincide with those in the gas, though larger dust grains produce

3.3. Results 118

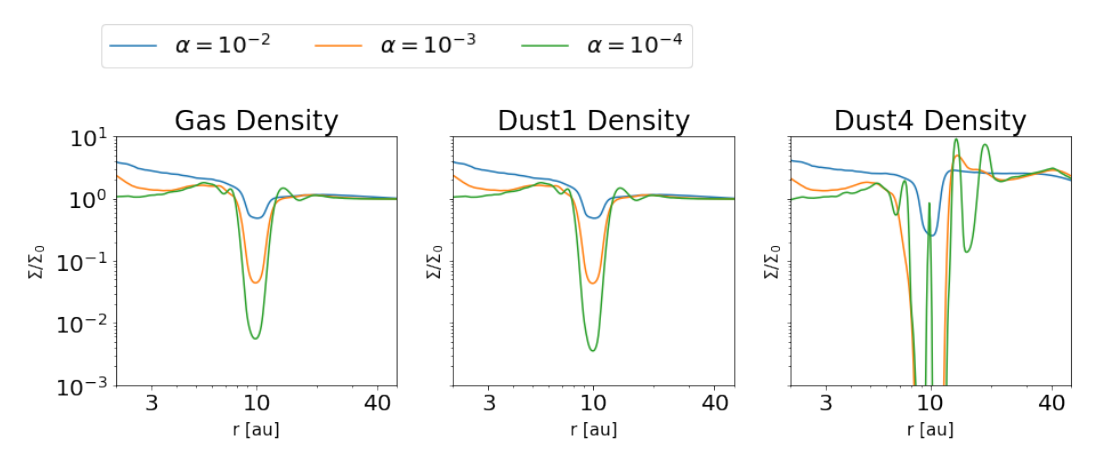


Figure 3.11: The surface density of gas,  $0.1 \ \mu m$  and 1mm dust (left to right) as a function of disk radius of  $100M_{\oplus}$  at 10au at different viscosities. The surface density is normalized by the initial value.

higher contrast features.

Regarding the gaps in Fig. 3.11, in general, for gas,  $\Sigma_{\rm gap}/\Sigma_0$  at  $\alpha=10^{-4}$  and  $\alpha=10^{-3}$  is approximately 2 and 1 orders of magnitude deeper, respectively, than at  $\alpha=10^{-2}$ . For dust, small grains couple well with the gas, while larger dust grains exhibit more pronounced structuring. Specifically, at high viscosity ( $\alpha=10^{-2}$ ), the mm dust gap is about 80% depleted. In the  $\alpha=10^{-3}$  case, a wide mm dust gap opens between 7 and 13 au, with the gap being nearly empty ( $\Sigma_{\rm gap}/\Sigma_0<10^{-3}$ ). At  $\alpha=10^{-4}$ , multiple gas and dust gaps appear, which can be attributed to the secondary spiral arms excited by the planet (Zhu et al., 2014; Bae, 2017; Dong et al., 2017). The main gap forms around  $r_{\rm p}$ , while a shallow secondary gap appears at 7 au (0.7  $r_{\rm p}$ ), and a deep (90% depleted) secondary dust gap is located 5 au beyond  $r_{\rm p}$ . The positions of these secondary gaps align with the findings of Zhang et al. (2018).

In terms of ring structure, three mm dust density rings are present at  $\alpha=10^{-4}$ . The ring at the outer gap edge is the strongest dust trap, showing an order-of-magnitude density enhancement. Additionally, a density peak is visible at the middle of the gap, likely caused by mm dust remaining in the horseshoe orbit. This could be a transient feature, as 2000 orbits may not be sufficient for the system to reach a steady state at  $\alpha=10^{-4}$ .

We present the results of the ice distribution for a  $100 M_{\oplus}$  planet in Figure 3.12.

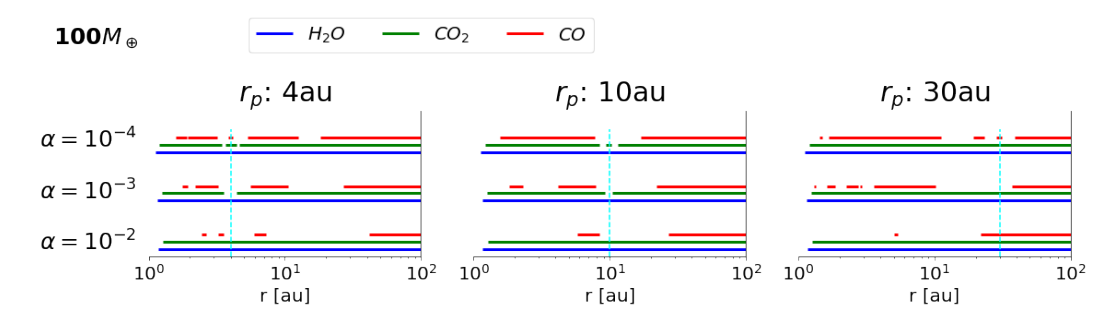


**Figure 3.12:** Iceline locations obtained from models with  $M_p = 100 M_{\oplus}$  and viscosity of  $\alpha = 10^{-2}$  (bottom),  $10^{-3}$  (middle) and  $\alpha = 10^{-4}$  (top). The vertical cyan lines mark  $r_p$ .

First, outside the gap region, we observe the same effects as in Figure 3.10. Lower viscosity predicts a lower  $T_{mid}$ , causing the CO ice region to start closer to the star. Second, within the gap region, there is no simple correlation between viscosity values and the widths of the CO sublimation regions due to gap opening. On one hand, lower  $\alpha$  viscosity results in a wider and deeper gap, which increases  $T_{mid}$ . On the other hand, in a disk without a planet, lower viscosity leads to a decrease in  $T_{mid}$ . As a result, the combined effect also weakens the correlation between  $\alpha$  viscosity and iceline locations and numbers. Notably, in cases with  $\alpha = 10^{-4}$ , some very short bars representing CO<sub>2</sub> or CO ice appear within the gap region. This occurs due to mm-sized dust remaining in horseshoe orbits or forming dust clumps at the L4 and L5 points. These mm dust overdensities at  $r_p$  cause a local drop in  $T_{mid}$ , leading to the freeze-out of CO or CO<sub>2</sub>.

## 3.4 Discussion

We discuss the implications of our results on the disk temperature structure and the observability of gap temperature changes. Also, we discuss the limits of our model.

# 3.4.1 Rings/gaps in hydro simulations vs molecule line observations

A deep gas gap identified in hydrodynamical (HD) simulations may not necessarily appear as a gap in molecular line observations. This discrepancy arises because HD simulations primarily model gas as H<sub>2</sub>, which is not directly observable. Ob-

servations, such as those conducted with ALMA, trace specific molecular species. For example, CO can freeze out or be photodissociated in certain disk regions and exhibit depletion levels different from those of  $H_2$  (e.g., Schwarz et al., 2018, 2019; Krijt et al., 2020).

Here we consider the case of CO and ignore photodissociation for simplicity. In a smooth disk, where no planet-induced substructures are present, CO remains in the gas phase at radii smaller than the CO iceline location,  $R_{co,ice}$ . If a deep H<sub>2</sub> gas gap is introduced at this location, the CO depletion follows that of H<sub>2</sub>, resulting in an observable gap in CO emission. Conversely, beyond  $R_{co,ice}$  in a smooth disk, CO is expected to freeze out onto dust grains, appearing as a dark region in observations. However, if a deep gas gap forms at a radial location outside  $R_{co,ice}$  (i.e., beyond where the CO iceline would be in a smooth disk), the reduced gas density and altered thermal structure may lead to the sublimation of CO, allowing it to return to the gas phase and forming a bright molecular ring in observations.

Thus, a deep  $H_2$  gas gap in a structured disk may manifest as a molecular ring if it is located outside the CO iceline of a smooth disk. Conversely, an observed molecular gap at radial location inside  $R_{co,ice}$  of the couterpart smooth disk may be caused either by CO freeze-out, potentially induced by dust rings or shadowing effects, or by a true deep gas gap in the disk. This highlights the importance of carefully interpreting molecular observations in the context of disk substructure and temperature.

# 3.4.2 Observability of planet impact on disk temperature and icelines

Previous observations of CO and CO isotopologue icelines accompanied by  $N_2H^+$  at  $\sim$ 20–30 au in the protoplanetary disk TW Hya have been reported in Qi et al. (2013); Zhang et al. (2017). These studies show a sharp drop in CO intensity at the iceline location.

Our structured disk modeling suggests that deep gaps opened by giant planets can significantly increase the local temperature (Fig. 3.6). If a gap forms outside the iceline of a smooth disk, it can sublimate volatile ices such as CO back into the

gas phase. Consequently, CO abundance will be higher at the gap compared to a disk without a gap, and the CO iceline will shift outward.

The above idea is potentially testable by comparing the CO iceline locations measured by ALMA with our disk model, where we place planets of different masses into the same disk setup. If a planet-induced gap is present, CO emission should extend farther out in intensity maps. For instance, in Fig. 3.7, in the  $3M_{\rm J}$  at 30 au case, the CO iceline moves to 50 au (top third in panel(a2)), whereas in the  $10M_{\oplus}$  at 30 au case (where the planet cannot open a gap), it remains at 20 au (top third in panel(c2)). In this case, a resolution of 30 au is required to resolve the change in the CO emission area. However, if this resolution is not achievable, CO spectral line profiles can still indicate the gap temperature change through an increase in CO intensity flux.

Additionally, CO ice sublimation at the gap could leave kinematic signatures in channel maps. Simply speaking, some velocity channels should show stronger CO emission in gap regions compared to gap-free regions. However, as shown in Chen & Dong (2024), both the inner and outer gap edges can exhibit strong gas velocity perturbations (on the order of  $\sim$ 0.1 of the local Keplerian velocity). Meanwhile, spirals near the planet can also induce velocity perturbations at similar levels as those at the gap edges. These perturbations can affect the intensity of CO emission in channel maps, potentially overlapping with the effects of gap temperature changes. Therefore, accurate modeling requires 3D hydrodynamical and radiative transfer simulations to predict the kinematic signatures in the future.

# 3.4.3 "Flickering" icelines

We have noted that complex, small-scale ice rings usually develop in the inner disk ( $\lesssim 5$  to 10 au, e.g., see Fig. 3.7 and the case of  $\alpha = 10^{-3}$  in Fig. 3.10) in our simulations. This is because the disk midplane conditions end up close to the local CO sublimation temperature, which makes the presence or lack of CO ice highly sensitive to fluctuations in the hydrodynamical models.

We propose that, while this makes it hard to pin down one specific iceline location, the phenomenon may be real. This would manifest as "flickering" icelines,

where large regions of the inner disk may irregularly fluctuate between CO freeze-out and sublimation, depending on small variations in the local disk conditions. Such a cycling of ice and gas phases in regions spanning anywhere from a small fraction of an au to  $\sim$  1 au in extent may have implications for the ice and gas chemistry, as well as in the ice composition inherited by pebbles or planetesimals in these disk regions.

#### 3.4.4 Limits of our model

First, our models neglect the effects of dust growth processes, including fragmentation, coagulation, and cratering. The timescales of dust growth may be comparable to those of dust drift, settling, and diffusion (Birnstiel, 2023). Dust growth alters grain sizes, which in turn affects dust opacities, influencing heating and cooling processes and ultimately modifying the disk temperature and iceline locations. Despite this, Savvidou et al. (2020) finds the temperature comparisons between the simple power-lawer grain size model (Mathis et al., 1977) is still similar (difference less than 10 K) to the more complex dust growth model Birnstiel et al. (2011) in regions outside the first few au in an equilibrium disk.

Second, in our iterative process, we assume that the surface-area-averaged dust temperature is equal to the gas temperature. However, this assumption is not always valid. For example, Facchini et al. (2018) show that in gap regions, gas and dust temperatures can decouple due to the reduced dust surface area. Specifically, they find that in the midplane of a deep gap,  $T_{gas}/T_{dust} < 1$ . Such lower  $T_{gas}$  can lead to deeper gas and dust gaps in hydrodynamical simulations.

Third, in our MCRT temperature calculations, we consider only stellar radiation. However, disk temperature can also be influenced by other factors, such as viscous heating and external radiation. Viscous heating primarily affects the disk midplane within the innermost few au. For a fixed viscosity, without gap formation, viscous heating increases  $T_{mid}$  in this region. However, if a gap forms at a few au, although more stellar photons can penetrate into the gap, even more viscous heat is lost. For example, Broome et al. (2023) shows  $T_{mid}$  within the gap (at around 3 au) form by a Jovian planet can decreases 20% to 30% from that of gap-free model.

For different  $\alpha$  viscosities, the temperature would generally increase with higher viscosity (Savvidou et al., 2020). Therefore, it would enhance the temperature difference that we show in Fig. 3.8. Additionally, external radiation sources, such as cosmic rays and external photoevaporation, can heat the outer disk regions.

Fourth, as the shifting, multiplication, and "flickering" (see Section 3.4.3) of icelines is dependent on general properties of the spatial temperature profile and its potential closeness to the sublimation temperature of specific volatile species, we do not expect those findings to fundamentally change with further improvements to the simulations (e.g., using a higher number of photon packages in MCRT). However, properties such as the absolute location or number of icelines for a given volatile chemical species may change somewhat.

#### 3.5 Conclusions

We iterate the hydrodynamical and radiative transfer simulations to study the planet-induced gas and dust substructures in disks and how these structures can affect the disk temperature structure. We compare our new models, including gas and multiple dust (Model D), with our old models with gas only (Model G). In addition, we investigate how different turbulent viscosities can influence our Model D. Here are our main findings:

- (1) Regarding density structure, compared to Model G, Model D predicts shallower gas gaps due to higher temperatures in the gap region. For instance, a  $100M_{\oplus}$  planet at 10 au in Model D opens a gas  $(\Sigma_{\rm gap}/\Sigma_0 \simeq 5 \times 10^{-2}$  and dust  $(\Sigma_{\rm gap}/\Sigma_0 < 10^{-6})$  gap, while the gas gap in Model G is about 1.5 times deeper (Fig. 3.3).
- (2) For the temperature at substructures, gaps or dust rings, like Model G, Model D also finds that a giant planet can increase the midplane temperature by a few tens of K in the gap region (Fig. 3.6). In Model D, a  $3M_J$  planet at 30 au forms a mm dust ring next to the outer gap edge, cooling  $T_{mid}$  by several K and creating a potential freeze-out zone (Figs. 3.5).
  - (3) Across the whole disk radius, the midplane temperature difference is not

significant between Model G and Model D. Combining the sublimation temperature of volatiles, we find that the ice distribution of  $H_2O$ ,  $CO_2$ , and CO is similar between these two models (Fig. 3.7).

- (4) In non-planet disks in Model D, decreasing  $\alpha$  viscosity (from  $10^{-2}$  to  $10^{-4}$ ) enhances dust settling, cooling the midplane by  $\sim 10$  K. This shifts the CO iceline (outside the self-shadowing region) inward, from 40 au ( $\alpha = 10^{-2}$ ) to 20 au (Fig. 3.8).
- (5) With a planet in Model D, low viscosity allows deeper gaps and stronger heating, complicating the relation between viscosity and gap temperature. This complexity is reflected in the width of CO sublimation regions (Fig. 3.12).
- (6) Planet-induced gaps can heat the disk locally, sublimating CO ice and pushing the CO iceline outward. This may be detectable with ALMA via CO intensity maps or spectral lines. However, for channel maps, velocity perturbations at gap edges and spirals may mimic thermal effects, requiring detailed 3D modeling to disentangle them.

# **Chapter 4**

Mind the kinematics simulation of planet-disk interactions: time evolution and numerical resolution

# **Abstract**

Planet-disk interactions can produce kinematic signatures in protoplanetary disks. While recent observations have detected non-Keplerian gas motions in disks, their origins are still being debated. To explore this, we conduct 3D hydrodynamic simulations using the code FARGO3D to study non-axisymmetric kinematic perturbations at 2 scale heights induced by Jovian planets in protoplanetary disks, followed by examinations of detectable signals in synthetic CO emission line observations at millimeter wavelengths. We advocate for using residual velocity or channel maps, generated by subtracting an azimuthally averaged background of the disk, to identify planet-induced kinematic perturbations. We investigate the effects of two basic simulation parameters, simulation duration and numerical resolution, on the simulation results. Our findings suggest that a short simulation (e.g., 100 orbits) is insufficient to establish a steady velocity pattern given our chosen viscosity ( $\alpha = 10^{-3}$ ), and displays plenty of fluctuations on orbital timescale. Such transient features could be detected in observations. By contrast, a long simulation (e.g., 1,000 orbits) is required to reach steady state in kinematic structures. At 1,000 orbits, the strongest and detectable velocity structures are found in the spiral wakes close to the planet. Through numerical convergence tests, we find hydrodynamics results converge in spiral regions at a resolution of 14 cells per disk scale height (CPH) or higher. Meanwhile, synthetic observations produced from hydrodynamic simulations at different resolutions are indistinguishable with 0.1 arcsec angular resolution and 10 hours of integration time on ALMA.

#### 4.1 Introduction

When planets form in protoplanetary disks, they can perturb the gas motion (Goodman & Rafikov, 2001), and produce kinematic signatures in line emission observations (Perez et al., 2015, 2018). By searching for and characterising such signatures, forming planets in disks can be identified, and their properties, such as masses and locations, can be constrained (Pinte et al., 2018; Casassus & Pérez, 2019; Teague et al., 2019b). This mechanism has become increasingly important in the search for planets in disks, which are challenging to find using more conventional planet detection methods such as radial velocity and transit surveys.

Among the various types of planet-induced kinematic signatures, a zigzag structure in the isovelocity curve in channel maps of gas emission, a.k.a. a "kink", has resulted in the most planet detections. Over a dozen planet candidates have been found in this way (Pinte et al., 2018, 2019, 2020). Bollati et al. (2021) have developed analytical models to quantify expected signals, while Izquierdo et al. (2021b) have proposed a statistical framework to quantify their detections in observations. Some of the planets discovered through the kink signature have been incorporated into the NASA's Exoplanet Database (e.g., HD 97048 b from Pinte et al. (2019)). Related observational signatures and planet detection techniques, such as "Doppler flip", have been developed and successfully applied to real systems as well (Casassus & Pérez, 2019).

Despite the successes, a number of issues exist and prevent establishing more robust and definitive connections between observed kinematic signals and planets, as highlighted in the recent review by Pinte et al. (2022). One of the most important questions is the exact origin of the "kink", which has not been fully determined. Also, it is unclear what the best strategy is to quantify the statistical significance of detected kink signals. Finally, in some systems the expected spirals in millimeter dust emission associated with the kink planets were not detected (Speedie & Dong, 2022), raising questions about our understanding of the observed kinematic signatures.

To address these issues, numerical simulations of disk-planet interactions are

needed to reproduce and analyze planet-induced kinematic signatures (Collaboration et al., 2020). This is necessary as most planets inferred from their kinematic signatures are above the disk thermal mass (Speedie & Dong, 2022), a regime where quantitative analytical theories on disk-planet interactions lack. A number of works have investigated planet-induced kinematic signatures in simulations. Perez et al. (2015) and Pinte et al. (2018, 2019, 2023) employed smooth particle hydrodynamic (SPH) simulations; with the exception of Pinte et al. (2019) these simulations are up to 100 planetary orbits. Perez et al. (2018) used a grid-based code, FARGO3D, and focused on velocity perturbations at the midplane and their observational signatures. Rabago & Zhu (2021) also used a grid-based hydro code (Athena++), coupled with a high  $\alpha$  viscosity (0.01). They focused on velocity perturbations in hydro calculations at different vertical layers instead of observational signatures.

Previous simulations provide insights into the kinematic signals induced by planets. However, the effects of two basic parameters, numerical resolution and system evolution time, have not been thoroughly investigated. The goal of this work is to study how planet-induced signatures in simulations depend on the two parameters. Meanwhile, we focus on non-axisymmetric features because they are expected to be more helpful in locating embedded planets than axisymmetric features, and because most reported planet detections so far are based on such features.

The paper is organized as follows. In §4.2, we lay out the setup for 3D hydro simulations. §4.3 presents the results of planet-induced velocity perturbations. We study the time evolution of simulation and carry out numerical resolution convergence tests. In §4.4, we make synthetic observations to further explore how the simulation time and numerical resolution can affect the planet-induced kinematics signatures. We summarize the results in §4.5.

# 4.2 Hydrodynamic simulation setup

We conduct 3D gas-only hydrodynamic (HD) simulations in spherical coordinates  $(r, \phi, \theta)$  = (radial, azimuthal, colatitude) using the grid-based code FARGO3D (Benítez-Llambay & Masset, 2016). A planet is fixed at a circular orbit at  $r_p$ . The

simulation domain spans from  $0.36r_{\rm p}$  to  $2.75r_{\rm p}$  in r, 0 to  $2\pi$  in  $\phi$ , and  $0.5\pi-0.35$  to  $0.5\pi$  in  $\theta$  (upper half-disk). Mesh grids are linearly distributed in  $\phi$  and  $\theta$ , and logarithmically distributed in r.

For boundary conditions, density and azimuthal velocities are extrapolated at the radial boundaries, while reflecting boundary conditions are applied in the colatitude direction to prevent mass inflow or outflow. Damping zones are applied near the radial boundaries of the mesh (de Val-Borro et al., 2006).

Following the approach of Perez et al. (2018), we assume an initial radial gas surface density profile of  $\Sigma_g = \Sigma_0 (r/r_{\rm p})^{-1}$ , where  $r_{\rm p} = 100$  au and  $\Sigma_0 = 0.09$  g/cm<sup>-2</sup>, resulting in a total disk mass of  $1.5 \times 10^{-3} M_{\odot}$  within the simulation domain. We model a flared disk with an aspect ratio h/r of 0.08 at  $r_{\rm p}$  and a flaring index of 0.15. The equation of state is assumed to be isothermal. We adopt an  $\alpha$  viscosity of  $10^{-3}$ , consistent with observations (Flaherty et al., 2015, 2017, 2018). The planet mass is chosen as  $5 \times$  the disk thermal mass  $M_{\rm th} = (h/r)_{\rm p}^3 M_{\star}$  (Rafikov 2002), which is  $\sim 2.5 M_{\rm J}$  around a solar-mass star given our chosen  $(h/r)_{\rm p}$ . The planet mass is typical among those in real systems with kinematic signature-based planet detections (Table A1 in Speedie & Dong, 2022). The simulations include the indirect term in the stellar gravity.

Four physical quantities are calculated in FARGO3D simulations: density  $(\rho)$ , radial velocity  $(V_r)$ , azimuthal velocity  $(V_{\phi})$ , and colatitude velocity  $(V_{\theta})$ . In visualization, we define the positive directions in velocities as moving away from the star for  $V_r$ , counter-clockwise rotation for  $V_{\phi}$  (same as the Keplerian flow), and toward the midplane for  $V_{\theta}$ .

# 4.3 Planet-induced perturbations in velocities

We run the simulations for 1,000 orbits and study how the non-axisymmetric velocity perturbations induced by a planet evolve with time in §4.3.1. We then carry out convergence tests to examine how the perturbations depend on numerical resolution in §4.3.2. Our cells are cubic and we produce simulations with an effective resolution of 7, 10, 14, or 20 grid cells per scale height (CPH) in the region around

the planet. As a reference, the simulation with a resolution of CPH= 20, the default setting in §4.3.1, has a grid of  $500 \times 1500 \times 90$  in  $(r, \phi, \theta)$ .

Most planet-induced kinematic signatures have been found in observations of CO line emission (Pinte et al. 2022), usually optically thick and from an emission surface at optical depth  $\tau=1$ . We locate the  $\tau=1$  surface of CO J=2-1 emission at  $\sim 2h$  (Fig. 4.12; Appendix 4.6.1), and focus on velocity perturbations at this surface.

Fig. 4.1 shows the surface density of the simulation with CPH= 20 at 100 and 1,000 orbits. The planet launches spiral density waves in both the inner and outer disks, and gradually opens a gap. We note that although a super-thermal mass planet can excite multiple prominent spiral arms, in particular in the inner disk (Fung & Dong, 2015; Bae & Zhu, 2018a,b), we focus on the primary arm as it dominates the velocity perturbations in regions close to the planet. The gap approaches its asymptotic depth at  $\sim 1,000$  orbits at the given viscosity (Fung & Chiang, 2016). At earlier stages, e.g., 100 orbits, accumulation of gas at the Lagrange points L4 and L5 are visible, with the latter being more prominent.

# **4.3.1** Temporal variations in planet-induced velocity perturbations

In our simulations, we have observed variabilities on both short (orbital) and long timescales (across 1,000 orbits) in planet-induced velocity perturbations. We separately discuss them in §4.3.1.1 and §4.3.1.2.

#### 4.3.1.1 Local variabilities in $V_r$ on orbital timescale

We focus on  $V_r$  in this part, a quantity close to zero everywhere in a smooth disk if the planet is not present. Figure 4.2 shows  $V_r$  in the  $r-\phi$  plane at 2h (i.e.,  $\theta = \pi/2 - 2(h/r)_p$ ) at 100 orbits (left) and 100.35 orbits (middle). The midplane density panel (c) shows the locations of the gap and spirals. 100 orbits has been the chosen epoch in previous studies of planet-induced kinematic signatures using SPH simulations (e.g., Pinte et al., 2018; Terry et al., 2022). The dashed circle highlights a region in the inner disk in between the primary and secondary spirals.

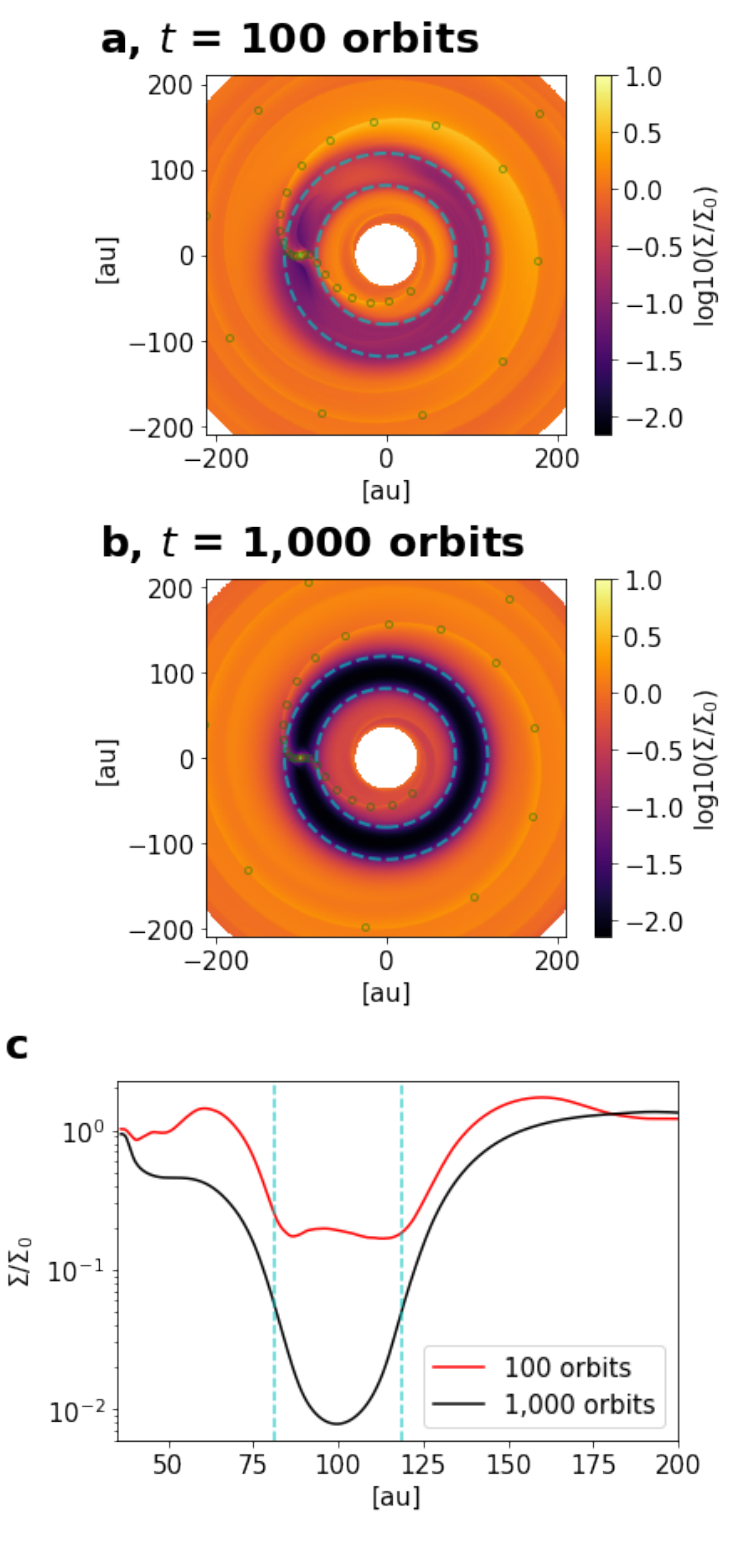


**Figure 4.1:** Surface density at 100 (upper) and 1,000 orbits (middle), and the corresponding azimuthal average (excluding azimuth within  $\arcsin\left(3R_{\rm H}/r_{\rm p}\right)$  to the planet) surface density profiles (lower). Cyan lines mark gap edges of  $r_{\rm p} \pm 2R_{\rm H}$  ( $r_{\rm p} = 100$  au and  $R_{\rm H} \sim 9.4$  au) in all panels. The surface density peak along the primary inner and outer spirals is traced out by green open circles.

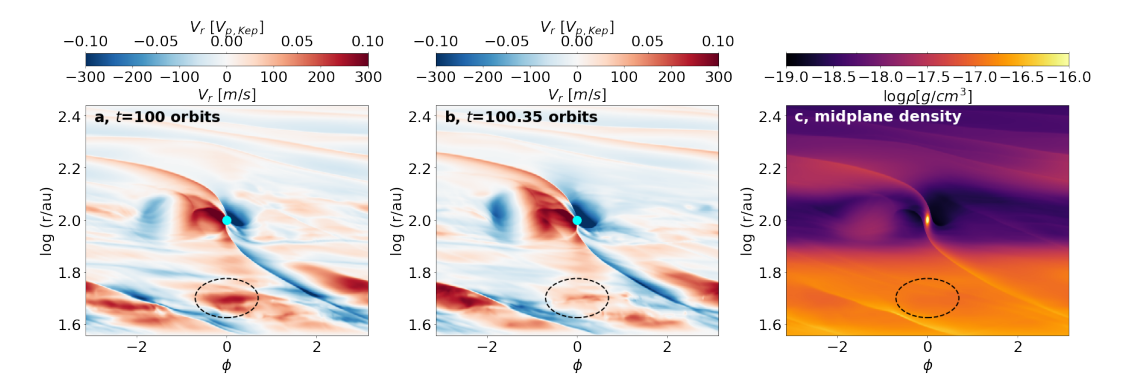


**Figure 4.2:**  $V_r$  at 2h from the midplane in a simulation with a planet mass of  $5M_{\rm th}$  and a numerical resolution of CPH= 20 at 100 (left) and 100.35 (middle) planetary orbits. The right panel shows the midplane density. The planet location is marked with a cyan dot in the first two panels. The dashed circle marks a region in between primary and secondary spiral arms in the inner disk. Colorbars are in units of m/s and planetary Keplerian velocity  $V_{\rm p,Kep}$ . See §4.3.1.1 and §4.3.1.2 for discussions.

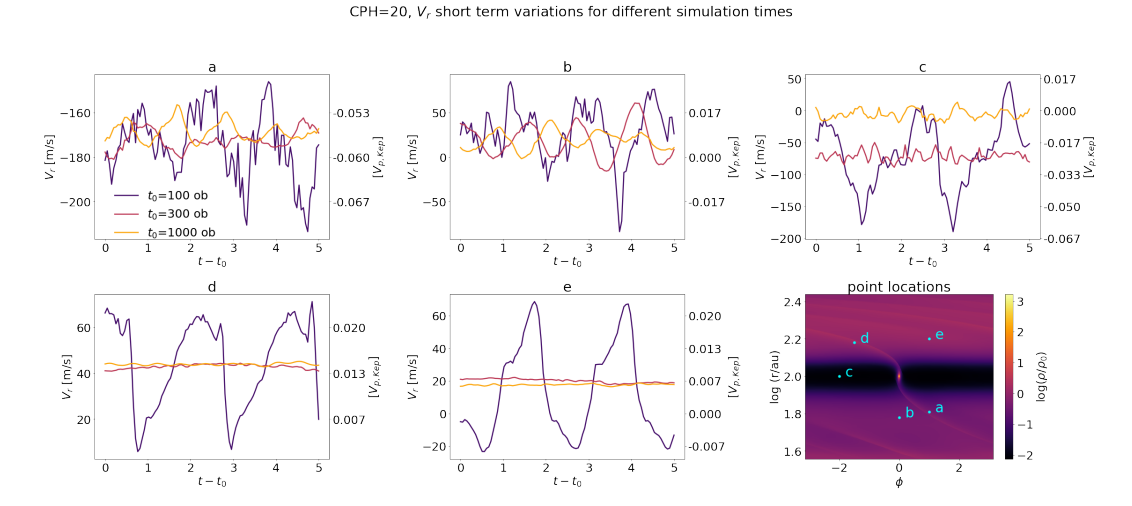


**Figure 4.3:** Short term variations in  $V_r$  within 5 orbits at 5 locations at 2h above the midplane from point a to e in the disk and at  $t_0 = 100$ , 300, and 1,000 orbits. The locations of points a, b, c, d, and e are shown in the midplane density map at 1,000 orbits in the lower right panel. See §4.3.1.1 for details.

At 100 orbits, this region exhibits  $|V_r| = 200 \text{ m/s} = 0.07 V_{p,\text{Kep}}$  ( $V_{p,\text{Kep}}$  is the planetary Keplerian velocity), higher than those along the spirals (about 150 m/s). However, at 100.35 orbits,  $|V_r|$  in this region falls below 100 m/s (0.03  $V_{p,\text{Kep}}$ ), indicating that velocity perturbations have not reached a steady state. In addition, this shows that planet-induced spiral density waves do not always dominate in  $V_r$  perturbations at this time.

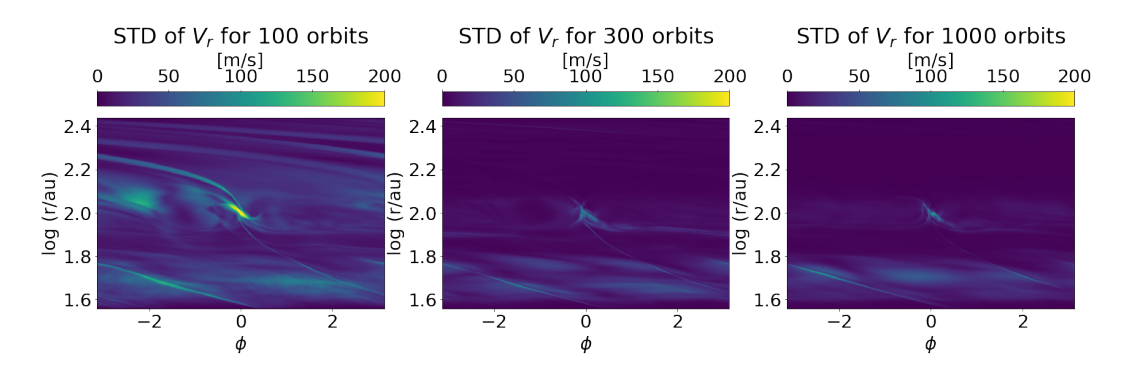


**Figure 4.4:** 2D standard deviation map of  $V_r$  at 100, 300 and 1,000 orbits (left to right). The standard deviations are obtained within 5 orbits (see details in §4.3.1.1).

The short term variability illustrated in Fig. 4.2 varies over the timescale of 1,000 orbits as well. Fig. 4.3 shows  $V_r$  at 2h (solid lines) as a function of time within 5 orbits at 5 representative points a, b, c, d, and e in the disk at t = 100, 300, and 1,000 orbits. These points are located at an inner spiral (a), in between the primary and secondary spirals in the inner disk (b), inside the gap (c), at an outer spiral (d), and in between the spirals in the outer disk (e). The temporal standard deviations (STD) at 100, 300, and 1,000 orbits are presented in Table 4.1. We use outputs every 0.05 orbits in the plot and STD calculations. A straight line from panel (a) to panel (e) and an STD close to 0 indicate the flow is steady on the orbital timescale at the epoch.

Overall, at 100 orbits,  $V_r$  exhibits significant short term variabilities, which tends to damp at 300 and 1,000 orbits. For example, at point b (in between spirals in the inner disk),  $V_r$  varies between -80 and 70 m/s within 5 orbits at 100 orbits (0.03  $V_{\rm p,Kep}$ ), with an STD of 30 m/s (0.01  $V_{\rm p,Kep}$ ). In contrast,  $V_r$  varies between 0 and  $\sim$  50 m/s at 300 orbits, with an STD of 19 m/s (about 0.01  $V_{\rm p,Kep}$ ), which drops further to 9 m/s at 1,000 orbits.

We also provide a 2D temporal STD map of  $V_r$  at 100, 300 and 1,000 orbits in Figure 4.4 to show the variability in other regions. Overall, we can see the fluctuation damps with time. At 100 orbits, regions near the planet, the gap, and the spiral arms exhibit significant variability, with STDs topping 100 m/s. However, as the system evolves over 300 and 1,000 orbits, the  $V_r$  field becomes nearly steady across most regions.

**Table 4.1:** Temporal standard deviations (STD) of  $V_r$  shown in Fig. 4.3 ( $V_r$  within 5 orbits at 5 different locations at t = 100, 300, and 1,000 orbits).

STD (m/s)	point a	b	С	d	e
t=100 (orbits)	15	30	51	18	28
t=300	4	19	7	< 1	1
t=1,000	4	9	7	< 1	< 1

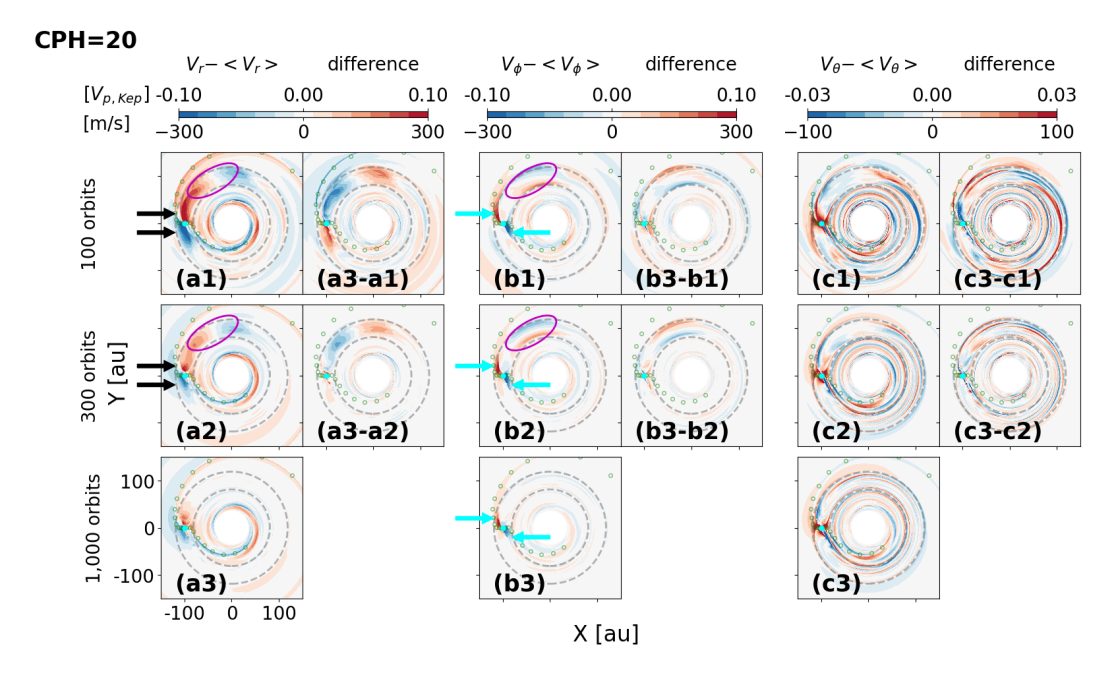


**Figure 4.5:** Group (a) panels: The non-axisymmetric components in  $V_r$  at 2h at 100, 300, and 1,000 orbits (left column), and their differences (right column). Group (b) and (c) panels: similar to group (a) panels, but for  $V_{\phi}$  (b) and  $V_{\theta}$  (c). The location of the planet is indicated by the cyan marker, and its size is set to  $0.4R_{\rm H}$ , the expected size of the circumplanetary disk. The trajectories of the spirals in the surface density are indicated by the small green circles ((also shown in Fig. 4.1). Gap edges at  $r = r_{\rm p} - 2R_{\rm H}$  and  $r_{\rm p} + 2R_{\rm H}$  are marked with grey dashed circles. The magenta ellipse indicates the gas structure at L5. The two ends of the horseshoe flow inside the gap are indicated by black arrows and the strong converging flows are indicated by cyan arrows. The colorbars are in linear scale. See §4.3.1.2 for details.

In addition, we show the short term variability of  $V_{\phi} - V_{\text{Kep}}$  and  $V_{\theta}$  in Appendix 4.6.2. The trend in both quantities is similar to that observed in  $V_r$ .

#### 4.3.1.2 Global signatures and their long term trend

We examine the perturbations in all three velocities at 2h from the midplane at 100, 300 and 1,000 orbits in Fig. 4.5. To eliminate the strong axisymmetric velocity perturbations caused by the gap and to highlight the non-axisymmetric features,

such as spirals, we subtract the azimuthally averaged velocities (denoted using <>>) from their native values to create residual maps. We prefer to use the azimuthal averages instead of the Keplerian flow as the background because subtracting the latter results in prominent super- and sub-Keplerian structures in  $V_{\phi}$  at the gap edges (Appendix 4.6.3).

To further compare how planet-induced velocity perturbations vary on 1,000 orbits timescale, we generate difference maps in the right column in each of the three groups in Fig. 4.5. For example, the radial velocity perturbation difference between 1,000 and 100 orbits panel (a3-a1) is made by subtracting panel (a1) from panel (a3).

In the radial direction, strong and stable non-axisymmetric velocity structures are present both on and off the spirals (panel group a). At 1,000 orbits (panel (a3)), the former have magnitudes about 170 m/s  $(0.06 \times V_{\rm p,Kep})$ , or  $0.7 \times c_{\rm s}$ , the local sound speed) at r=85 au at the inner spirals and 180 m/s at 110 au at the outer spirals. Both remain relatively unchanged throughout the 1,000 orbits, varying by less than 20%.

In contrast,  $V_r - \langle V_r \rangle$  in the off-spiral regions significantly weaken with time. At 100 orbits (panel (a1)), two structures stand out — the revolution around L5 inside the gap (magenta ellipse), and the turn of the flow at the two ends of the horseshoe (black arrows). The former has a magnitude of 250 m/s (0.08  $V_{\rm p,Kep}$ ) at 100 orbits, stronger than that of the spirals, before dropping to 200 m/s (0.07  $V_{\rm p,Kep}$ ) at 300 orbits (panel (a2)) and to below 25 m/s at 1,000 orbits (panel (a3)). The horseshoe turn has a magnitude of higher than 300 m/s at 100 orbits, much stronger than that of the spirals, before dropping to 200 m/s around the planet at 1,000 orbits.

In the non-axisymmetric component of the azimuthal velocity, the counterparts of the revolutionary motion around L5 are also prominent at 100 and 300 orbits (panels b1 and b2, magenta ellipses), before damping to below 50 m/s at 1,000 orbits. On the leading and trailing sides of the planet, strong converging flows up to 300 m/s (0.1  $V_{\rm p,Kep}$ , indicated by the cyan arrows) are visible at 100 orbits, and their magnitudes remain nearly constant throughout 1,000 orbits (panel (b3-b1) and

(b3-b2)). Their origin is not entirely clear, as the features are slightly offset from the spiral waves. The non-axisymmetric components at the spirals in the outer disk is below 100 m/s (0.03  $V_{\rm p,Kep}$ ) throughout the simulation, weaker than that in the inner disk.

In the polar direction, the gas motion with the highest velocity (>100 m/s, 0.03  $V_{\rm p,Kep}$ ) is in the infalling flow towards the planet at its vicinity. The area of this flow shrinks and its velocity becomes weaker from 100 to 1,000 orbits (panel (c3-c1)) as the gap get deeper, while its velocity and area remain roughly unchanged between 300 and 1,000 orbits (panel (c3-c2)). Turbulent motions at the level of 100 m/s both inside the gap and at its edges sustained over 1,000 orbits are also prominent, consistent with previous studies (e.g., Dong et al., 2019). In comparison, the vertical gas motions at the spiral locations are not the dominant signals.

The right column in each of the three groups in Fig. 4.5 shows the differences in the velocity perturbations at two simulation times. Overall, the main differences occur in the non-spiral regions. Comparing panel (a3-a1) with panel (a3-a2), we find that as time increases, the size of the gas structure at L5 shrinks and the signals at the horseshoe ends become weaker. Specifically, differences in the radial velocity  $V_r - \langle V_r \rangle$  at the horseshoe ends between 100 and 1,000 orbits (panel (a3-a1)) reach  $\sim 250$  m/s (0.08  $V_{\rm p,Kep}$ ), while the differences in  $V_r - \langle V_r \rangle$  (and  $V_\phi - \langle V_\phi \rangle$ ) around L5 between 300 and 1,000 orbits (panel (a3-a2)) reach 150 m/s (0.05  $V_{\rm p,Kep}$ ). Meanwhile, all three velocities in the spirals vary negligibly between 300 and 1,000 orbits. The strongest variation of  $V_r - \langle V_r \rangle$  at spirals between 100 and 1,000 orbits appears at r = 120-150 au with a magnitude of 150 m/s (0.05  $V_{\rm p,Kep}$ ).

## **4.3.2** Numerical convergence tests

We present numerical convergence tests in Fig. 4.6. Following the discussions in §4.3.1.2, we focus on 3D non-axisymmetric velocity perturbations at 2h at 1,000 orbits. We compare the simulations with different resolutions by showing their differences; for instance, panel (a1) shows the differences in  $V_r - \langle V_r \rangle$  between two runs with CPH= 10 and 7. When creating the difference maps, we interpolate the outputs from all lower resolution runs to the highest resolution run, 20 CPH. While

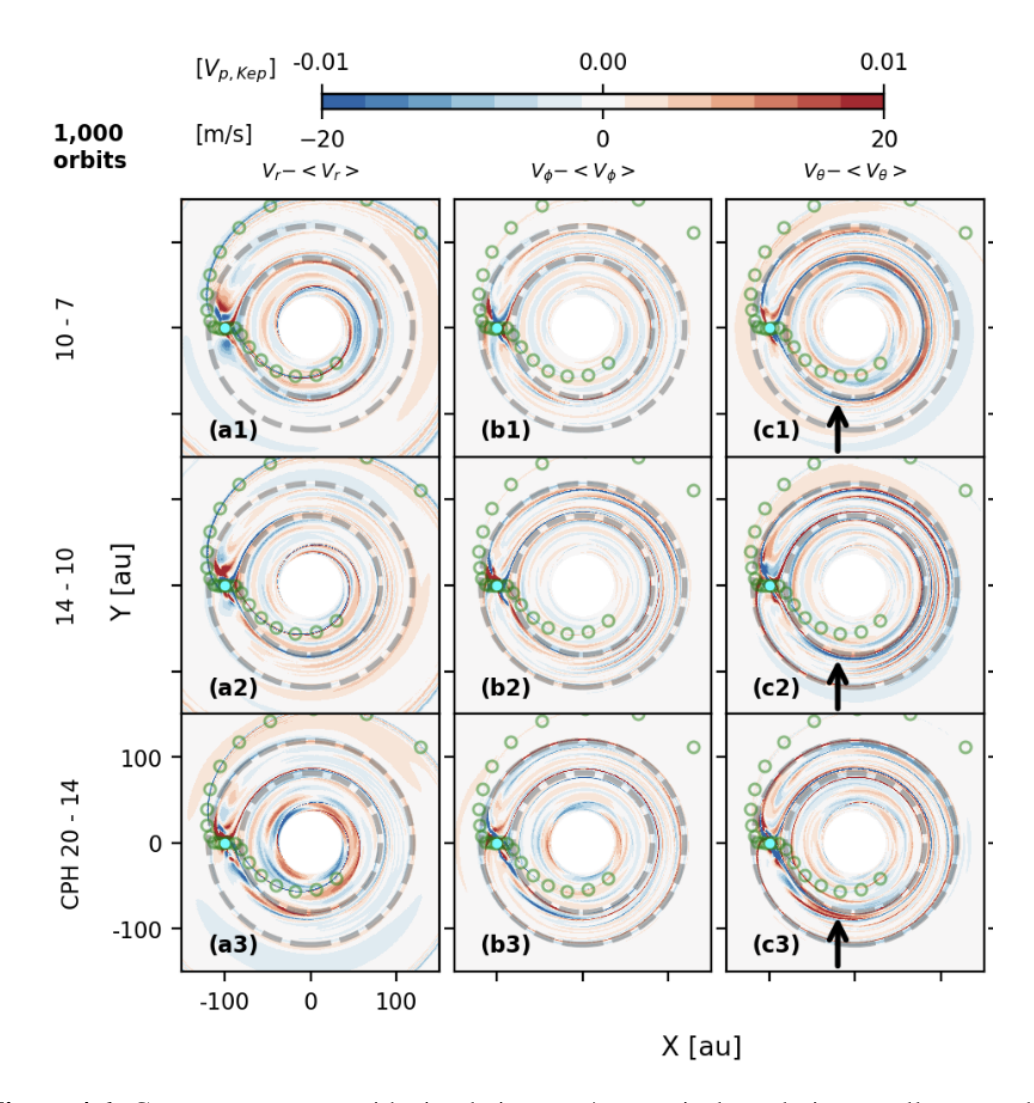


**Figure 4.6:** Convergence tests with simulations at 4 numerical resolutions: cells per scale height (CPH) around the planet of 7, 10, 14, and 20. The top row shows the differences between two runs with CPH=7 and 10 in non-axisymmetric velocity perturbations at 2h away from the midplane at 1,000 orbits for the three velocities. The middle and bottom rows show the differences between the simulations with CPH=10 and 14, and the simulations with CPH=14 and 20, respectively. The primary inner and outer spiral density waves are marked by open green circles. Grey dashed lines indicate the inner and outer gap edges. The location of the planet is indicated by the cyan marker, and its size is set to 0.4*R*<sub>H</sub>, the expected size of the circumplanetary disk. The colorbar is in a linear scale. See §4.3.2 for discussions.

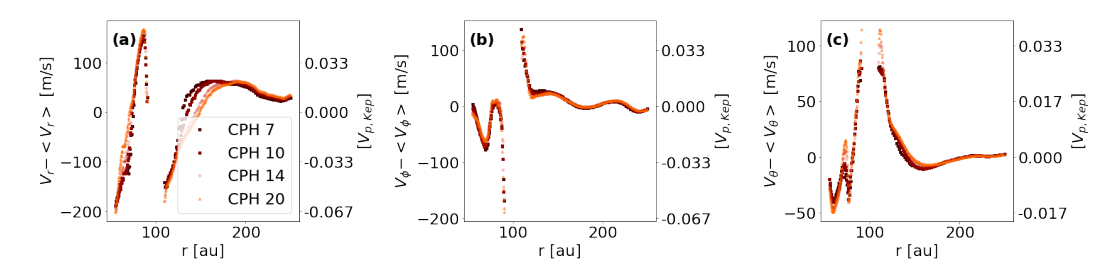


**Figure 4.7:** The three components in non-axisymmetric velocity perturbations along the primary spiral density waves (traced out by the green circles in Figs. 4.1 and 4.6) at 2h away from the midplane at 1,000 orbits for 4 simulations with different numerical resolutions: cells per scale height (CPH) of 7, 10, 14, and 20. We exclude the region within  $R_{\rm H}$  from the planet at 100 au due to insufficient resolution in the circumplanetary region. The velocity field along the spirals is converging with resolution. See §4.3.2 for further discussions.

the variations are smaller than 20 m/s (0.01  $V_{p,Kep}$ ) in most regions, whether any of the three velocity components has converged at our highest resolution (CPH = 20) depends on the region in the disk.

Along the primary spirals (green open circles in Fig. 4.6), velocity perturbations are converging with resolution. This can be more quantitatively seen in Fig. 4.7, where we show  $V_r - \langle V_r \rangle$ ,  $V_\phi - \langle V_\phi \rangle$ , and  $V_\theta - \langle V_\theta \rangle$  along the primary spirals in panels (a), (b), and (c), respectively. In contrast, the non-spiral regions have not shown signs of convergence yet at our highest resolution (CPH=20). For example, the inner gap edge, indicated by an arrow in Fig. 4.6, exhibits a larger difference in  $V_\theta - \langle V_\theta \rangle$  between CPH=20 and CPH=14 (c3), compared with that between CPH=14 and CPH=10 (c2).

# 4.4 Signatures in synthetic CO observations

To explore how the effects of simulation time and resolution manifest in searching for planet-induced kinematic signatures, we post-process the FARGO3D outputs using RADMC3D (Dullemond et al., 2012) to generate synthetic observations of CO J=2-1 line emission. We describe the procedure in §4.4.1, and introduce the results in §4.4.2 and §4.4.3.

#### 4.4.1 Synthetic observation generation

We produce synthetic CO observations by sending the FARGO3D output density and velocity structures into RADMC3D to generate channel maps at our specified spectral resolution. They are then convolved by a point spread function to achieve the desired angular resolution. An example channel map is shown in Fig. 4.8 (panel a).

To set up RADMC3D, we assume that the entire disk extends from 1 to 275 au, with a disk mass of  $1.7 \times 10^{-3} M_{\odot}$ . For the extrapolation from 36.5 au, the inner boundary of the hydro simulations, to 1 au, we assume  $\Sigma(r) \propto r^{-1}$ . For the stellar parameters, we adopt  $M_{\star} = 1 M_{\odot}$ ,  $R_{\star} = 1.7 R_{\odot}$ , and  $T_{\star} = 4,700 K$ , suitable for a pre-main-sequence star. Stellar radiation serves as the sole heating source.  $N_{\rm photon} = 10^8$  photon packages are used. We assume silicate dust particles with an intrinsic density of 3.71 g/cm<sup>3</sup>. We include grains with sizes ranging from 0.1 to  $10 \mu m$  in the calculation. Due to the effective coupling of such small dust grains with the gas, the dust and gas are assumed to be well-mixed. We also assume the grain size distribution follows a power law with an index of -3.5 and a maximum grain size of 1mm (grains with sizes between  $10 \mu m$  and 1 mm are not included in the simulations), and the total dust to gas mass ratio is 1%. Therefore, the dust mass within 0.1 to  $10 \mu m$  is about 10% of the total dust mass, or 0.1% of the total disk mass. We calculate the corresponding dust opacity using the optool package (Dominik et al., 2021).

To make synthetic channel maps, we assume the gas temperature is the same as the dust temperature from radiative transfer. We assume a CO to  $H_2$  ratio of  $10^{-4}$ , and a viewing angle of disk inclination =  $45^{\circ}$  (similar to that of disk HD 163296; Pinte et al. 2018), position angle (PA) =  $90^{\circ}$ , and the southern side being the near side. The images are convolved with a 0.1 arcsec Gaussian beam, typical in observations of kinematic signatures (Speedie & Dong, 2022, Table A2). The synthetic cubes have a channel width of 0.2 km/s.

Negative (positive) velocities denote gas moving towards (away from) the observer along the line of sight (LOS). A planet is placed at a position angle of

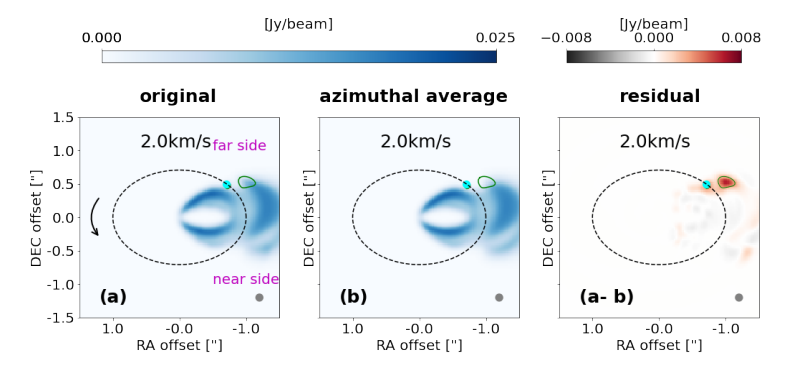


**Figure 4.8:** Example products from RADMC3D radiative transfer simulations. Panel (a) is a channel map at  $V_{\rm ch} = 2.0$ km/s directly produced from a FARGO3D simulation output. Panel (b) is a channel map produced from the same FARGO3D simulation, but with density and all three velocities azimuthally averaged. Panel (a-b) is the difference between the two. Contours in panel (a-b) are at  $3\sigma = 3$  mJy/beam level (both positive and negative), and they are overplotted in panels (a) and (b). The planet's orbit is indicated by the black dashed ellipse and the arrow indicates the direction of Keplerian rotation. The planet's location is indicated by the cyan marker, and its size is set to  $0.4R_{\rm H}$ , the expected size of the circumplanetary disk. The disk near side and far side are annotated. We put the disk at a distance of 100 pc. The synthesized beam is depicted in the bottom right of each panel. The colorbars are in linear scale.

 $\phi_{\rm p}=315^{\circ}$  in the disk frame, in between the disk major and minor axes. The planet orbits the star in the counter-clockwise direction at  $r_{\rm p}=100$  au with a LOS velocity  $V_{\rm p,LoS}=1.5$  km/s.

To highlight and quantify the non-axisymmetric features in gas emission caused by the planet, we create residual channel maps, illustrated in Fig. 4.8 (panel c). Similar to the residual velocity maps (§4.3.1.2; Fig. 4.5), residual channel maps are also produced by subtracting the azimuthally averaged background (we azimuthally average the hydro quantities before conducting the radiative transfer) instead of the Keplerian background from the original channel maps. In real observations, the azimuthal average background may be found by fitting the observational data with models using public tools such as eddy (Teague, 2019). Green contours in the residual panel mark  $3\sigma$  regions that are larger than a beam size, and are overlaid in the other panels. We adopt  $\sigma = 1$  mJy/beam, corresponding to 10 hours of integration time with our observing parameters<sup>1</sup>. In the residual channel map at a specific velocity  $V_{\rm ch}$ , a positive region (red) has more emission at this velocity in the

https://almascience.eso.org/proposing/sensitivity-calculator

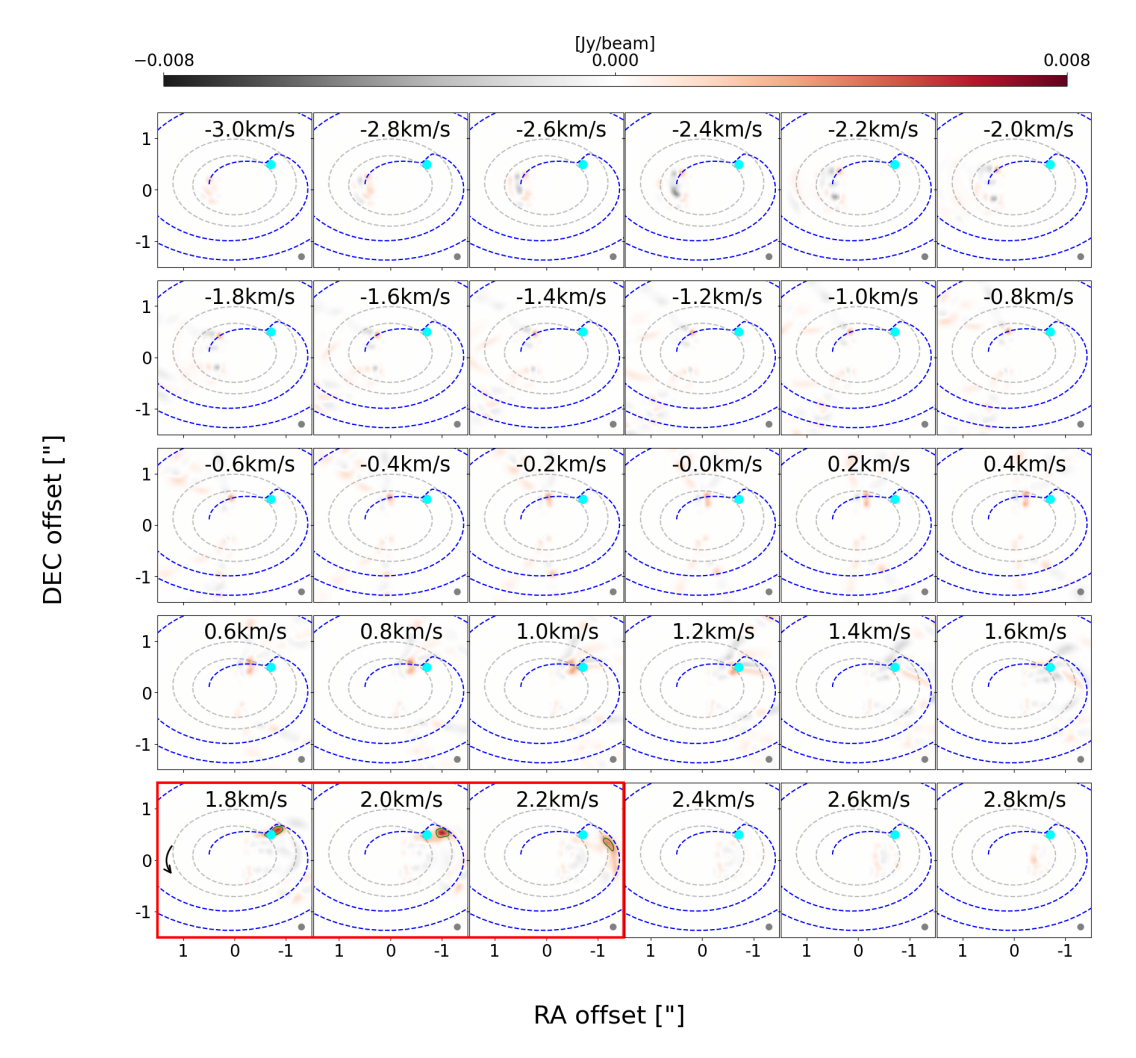


**Figure 4.9:** Successive residual channel maps of the same kind as panel (a-b) in Fig. 4.8 of the simulation with CPH= 20 at 1,000 orbits. Signals in the maps highlight non-axisymmetric velocity perturbations induced by the planet. Potentially detectable residuals are highlighted by  $3\sigma$  contours (green). We only mark  $3\sigma$  signals with a size bigger than a beam. Such signals are most prominently present in channels at  $V_{\rm ch}=1.8$  to 2.2 km/s (highlighted with a red frame). Grey and blue dashed lines denote gap edges and the primary spirals, respectively. The location of the planet is indicated by the cyan marker. The disk rotation direction is marked in the lower left panel. The colorbar is in a linear scale. See §4.4.1 for further discussions.

planet-perturbed disk than that in the azimuthally-averaged disk, and vice versa.

We present successive residual channel maps of the same type as Fig. 4.8c from the simulation with CPH=20 at 1,000 orbits in Fig. 4.9. The corresponding original channel maps are shown in Appendix 4.6.4. Potentially detectable ( $> 3\sigma$ ) non-axisymmetric signals are present in some channels ( $3\sigma$  contours marked in green),

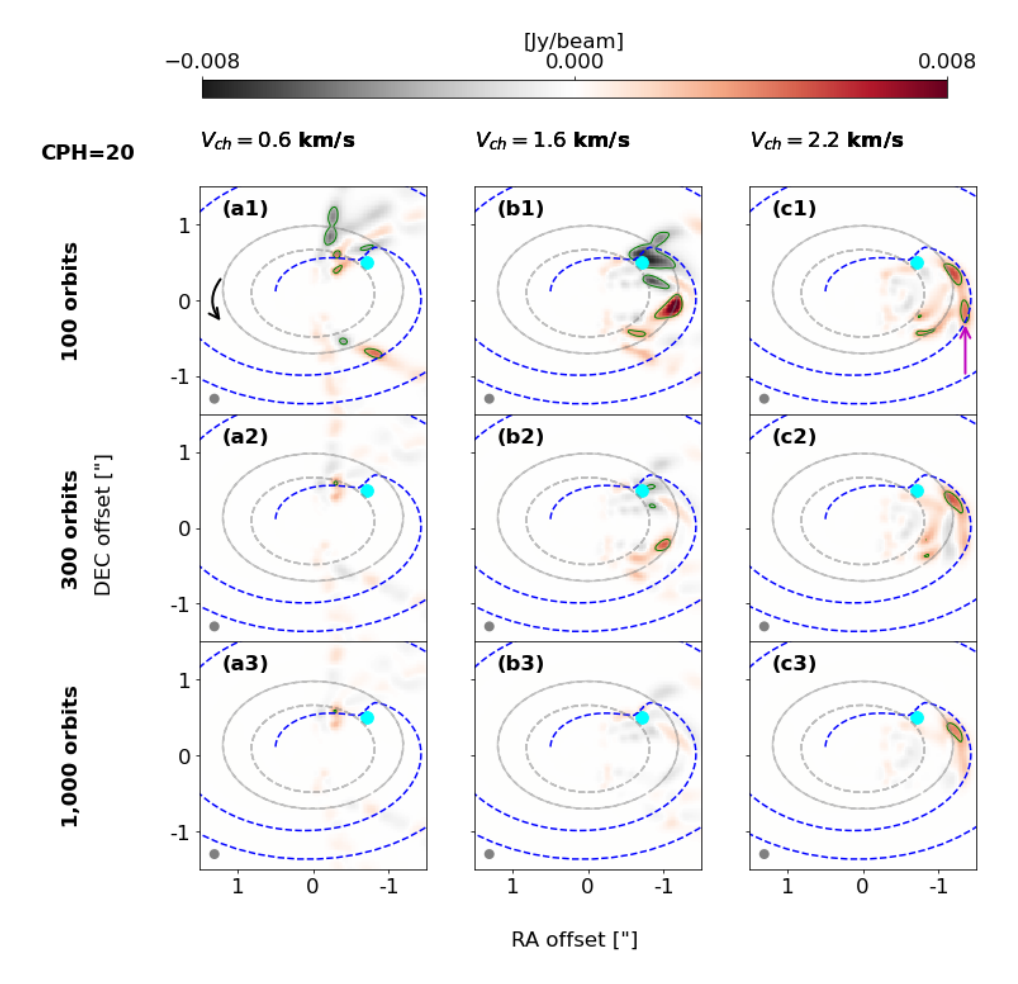


**Figure 4.10:** Residual channel maps (the same kind as panel (a-b) in Fig. 4.8) of the simulation with CPH= 20 at  $V_{\rm ch}=0.6$  (the (a) panels), 1.6 (b), and 2.2 km/s (c). Results at 100, 300, and 1,000 orbits are shown from top to bottom. Planetinduced non-axisymmetric kinematic signatures evolve with time. The planet is positioned at the position angle  $\phi_p=315^\circ$  in the disk frame. Residual emissions stronger than  $3\sigma=\pm3.0$  mJy/beam are marked with green contours. In each panel, the blue dashed curve represents the primary spirals at 2h away from the midplane, and grey lines mark the inner and outer gap edge. The beam size is displayed at the bottom left. The disk rotation direction is marked in panel (a1). The colorbar is in a linear scale. See §4.4.2 for discussions.

specifically in the velocity range  $V_{\rm ch} = 1.8$  to 2.2 km/s (the panels enclosed in a red frame). The  $3\sigma$  features at  $V_{\rm ch} = 1.8$  and 2.0 km/s coincide with the planet. The  $3\sigma$  feature at 2.2 km/s is extended, and slightly offset from the outer primary spiral and partly overlapping with the outer gap edge.

#### 4.4.2 Effect of simulation time

Fig. 4.10 illustrates how planet-induced non-axisymmetric kinematic signatures, manifesting as features in residual channel maps, evolve with time over 1,000 orbits. We focus on 3 channels,  $V_{\rm ch} = 0.6$ , 1.6, and 2.2 km/s.

Overall, regions with  $3\sigma$  residuals shrink with time. At  $V_{\rm ch}=0.6$  km/s (the (a) panels), a channel far away from  $V_{\rm p,LoS}=1.5$  km/s,  $3\sigma$  signals appear at the outer gap edge at PA  $\sim 0$  and near the outer primary spiral at 100 orbits (panel a1). However, such signals disappear at 300 and 1,000 orbits. At  $V_{\rm ch}=1.6$  km/s,  $3\sigma$  residuals at L5 at PA $\sim 270$  ° are present at both 100 (b1) and 300 (b2) orbits, so do residuals at horseshoe turns at 100 orbits. In contrast, there is no  $3\sigma$  residual signal at 1,000 orbits.

In addition, the morphology of the robust (long-lasting)  $3\sigma$  residuals also evolves with time. At  $V_{\rm ch}=2.2$  km/s (the (c) panels), although the features crossing the outer gap edge are visible at all three epochs, their sizes slightly decrease with time. At 100 orbits (c1), the  $3\sigma$  signal along the outer primary spiral splits into two regions. One of the two regions in panel (c1), indicated by a magenta arrow, drops below  $3\sigma$  at 300 and 1,000 orbits (c2 and c3).

#### 4.4.3 Effects of numerical resolution

Fig. 4.11 shows the residual and difference channel maps at  $V_{\rm ch} = 1.8 - 2.2$  km/s at 1,000 orbits for simulations with resolutions of CPH=10, 14 and 20. Difference channel maps are obtained by subtracting residual channel maps at different resolutions. The results exhibit good convergence. No  $3\sigma$  features are found in the difference maps, both at the three velocities and at all other velocities (not shown here). Therefore, given the chosen sensitivity, angular resolution, and channel width, the differences due to different numerical resolutions ranging from 10 to 20 CPH cannot be discerned in synthetic observations.

#### 4.5 conclusions

We use grid-based hydrodynamic and radiative transfer simulations to investigate how planet-induced kinematic signatures depend on simulation time and numerical

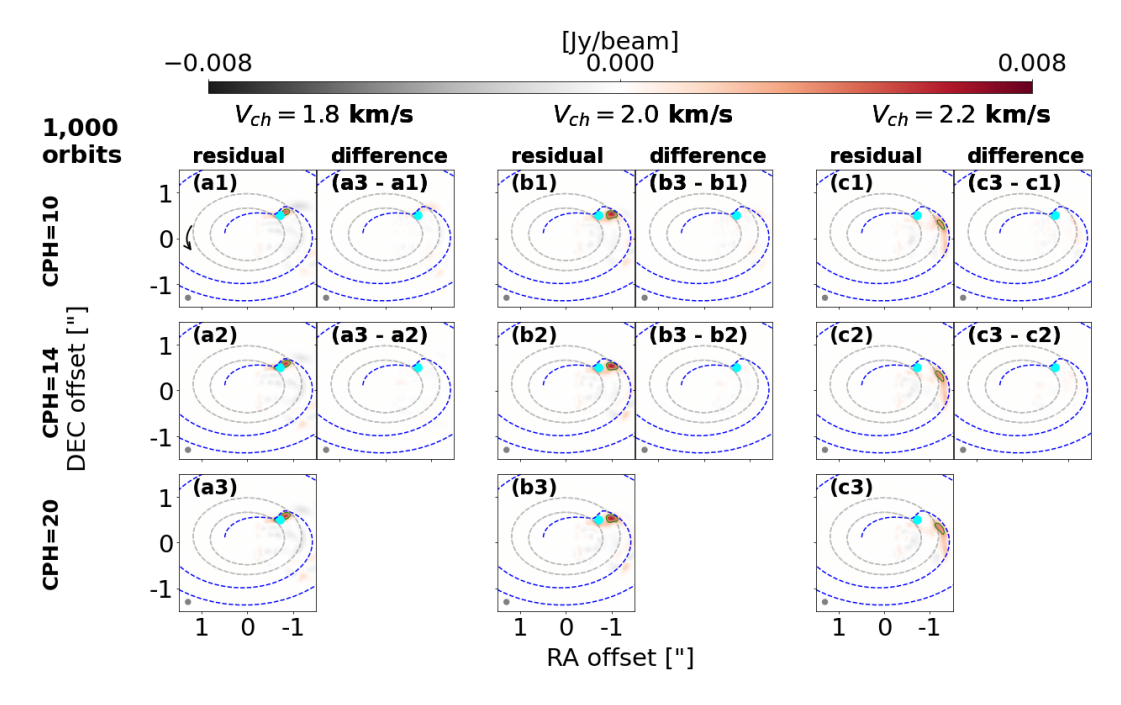


**Figure 4.11:** Resolution convergence test of synthetic channel maps. For each  $V_{\rm ch}$ , the left and right columns present residuals (similar to Fig. 4.8(a-b)) and differences, respectively. Difference channel maps are obtained by subtracting residual channel maps at different resolutions. Residual or difference emission stronger than  $3\sigma=\pm 3.0$  mJy/beam are marked with green contours. The disk rotation direction is marked in the top left panel. The colorbar is in a linear scale. See §4.4.3 for discussions.

resolution in both velocity space and synthetic CO line emission. We focus on non-axisymmetric signals that are more easily localized in observations. We choose a planet with  $2.5\,M_{\rm J}$  (5 disk thermal masses) at 100 au, typical for planets detected via local kinematic signatures (e.g., "kinks"; Pinte et al. 2018, 2019, 2020). We focus on signatures at 2 disk scale heights, close to the CO emission surface. We propose to identify and quantify planet-induced kinematic signals in residual channel maps, the difference between the original channel map and the one produced from the same disk-planet model with density and velocities azimuthally averaged (panel (a-b) in Fig. 4.8). Our main findings are:

1. Simulations of short timescales, e.g., 100 orbits, are insufficient for establishing steady planet-induced velocity perturbations in grid-based simulations with viscosity  $\alpha = 10^{-3}$ . We find strong velocity structures at non-spiral regions, including the Lagrange points, horseshoe, and gap edges, at 100 orbits

- (Figs. 4.2). Their strengths can be comparable to, or even bigger than, the more robust and steady signatures along the spirals. In addition, such signatures vary significantly on dynamical timescale (e.g. exceeding 250 m/s or  $0.08 V_{\rm p,Kep}$  as shown in Fig. 4.3). They are potentially detectable in ALMA CO observations with 10 hours of integrations (Fig. 4.10). However, these features are damped over 1,000 orbits.
- 2. A sufficiently long simulation time, such as 1,000 orbits, can establish a steady velocity field. Based on results at 1,000 orbits shown in Fig. 4.5, the strongest velocity deviations from the azimuthal average background can reach up to  $\pm 300$  m/s  $(0.1 \ V_{\rm p,Kep})$  in the azimuthal direction near the planet and slightly offset from the density spiral.
- 3. Robust non-axisymmetric velocity perturbations at 1,000 orbits can be present in several velocity channels in residual channel maps. In our setup with median disk inclination and planet position angle in between the disk major and minor axes (similar to the case in Pinte et al. (2018)), such perturbation signal appears around the line-of-sight velocity of the planet. They are potentially detectable in ALMA programs with reasonable parameters (an angular resolution of 0.1", a channel width of 200 m/s, and a sensitivity of 1 mJy/beam; Fig. 4.9).
- 4. At 1,000 orbits, planet-induced velocity perturbation along the spirals converges in hydro simulations at a numerical resolution of 20 cells per scale height (CPH). The results obtained from the runs with CPH= 14 and CPH= 20 differ by less than 10 m/s in all three velocities (Figs. 4.6 and 4.7). However, convergence is not achieved in off-spiral regions even at our highest resolution (CPH= 20). Nevertheless, the effect may not be detectable in ALMA observations with our observing setup (Fig. 4.11).

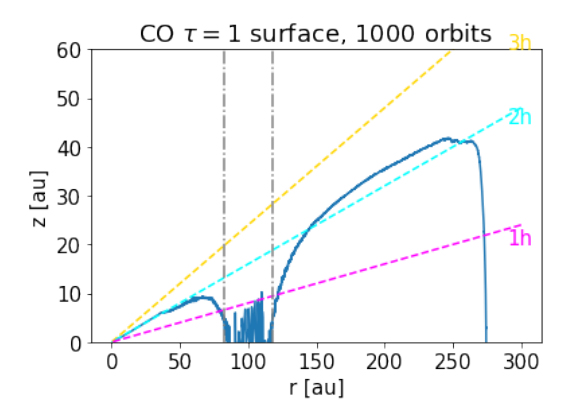


**Figure 4.12:** Azimuthally averaged  $\tau = 1$  surface of synthetic CO J = 2 - 1 emission (blue line) of the simulation with CPH= 20 at 1,000 orbits. Dashed lines in magenta, cyan, and yellow represent 1, 2, and 3 scale heights, respectively. The grey dashed-dotted lines mark the inner and outer gap edge. The planet is at r = 100 au.

## 4.6 Appendix

#### **4.6.1** $\tau = 1$ surface

In Fig. 4.12, we show the azimuthal average  $\tau=1$  surface of CO J=2-1 emission of the simulation with CPH= 20 at 1,000 orbits. The  $\tau=1$  surface is determined under the assumption that the disk inclination is 0. Except for the deep gap region (marked by grey dashed-dotted lines), with the  $\tau=1$  surface is roughly located at 2 scale heights.

## **4.6.2** Local variabilities in $V_{\phi} - V_{\text{Kep}}$ and $V_{\theta}$ on orbital timescale

Fig. 4.13 and 4.14 show the short term variabilities within 5 orbits of  $V_{\phi} - V_{\text{Kep}}$  and  $V_{\theta}$  at 2h at 100, 300. and 1,000 orbits at the same 5 representative locations as in §4.3.1.1 and Fig. 4.3. Similar to  $V_r$  (§4.3.1.1), both  $V_{\phi} - V_{\text{Kep}}$  and  $V_{\theta}$  display significant short term variations at 100 orbits (e.g. point c, they vary more than 0.05  $V_{\text{p,Kep}}$ ) while the variability drops at 300 and further at 1,000 orbits (5-orbit temporal STDs less than 20 m/s for all 5 points).

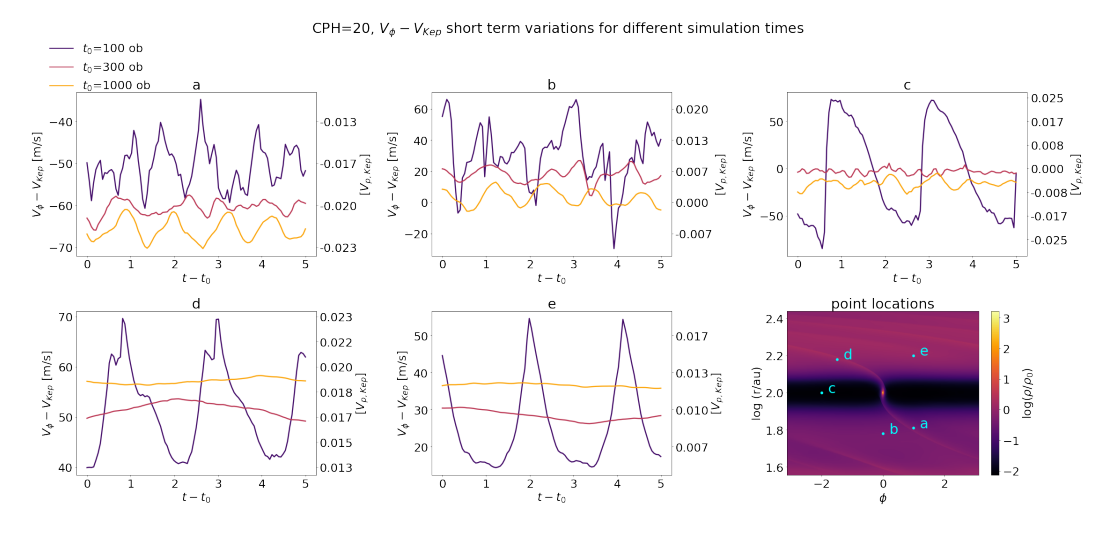


**Figure 4.13:** Similar to Fig. 4.3 but for  $V_{\phi} - V_{\text{Kep}}$ .

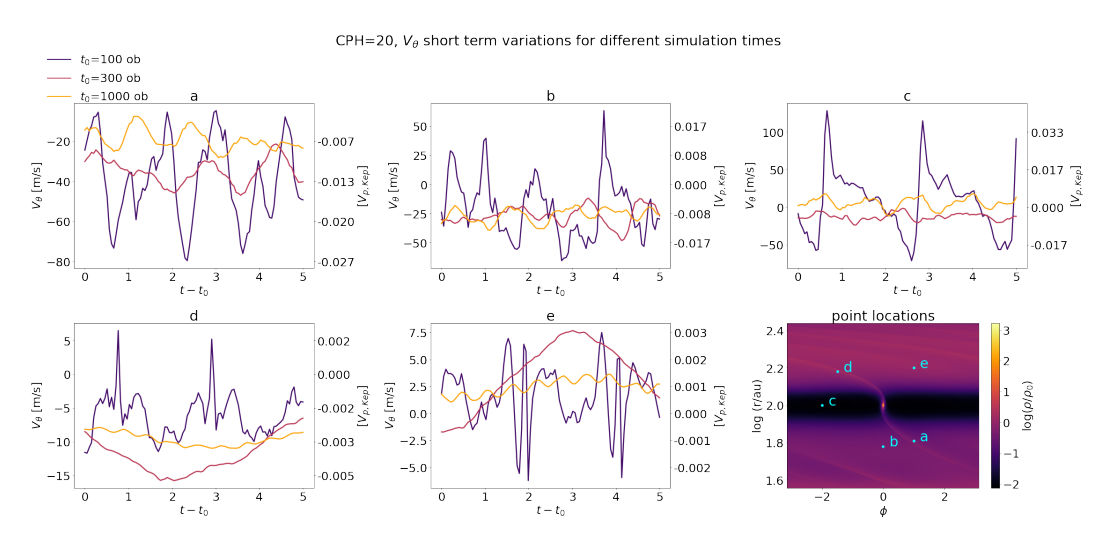


**Figure 4.14:** Similar to Fig. 4.3 but for  $V_{\theta}$ .

# 4.6.3 Azimuthal average background versus Keplerian background

Fig. 4.15 compares the  $V_{\phi}$  perturbations when subtracting the azimuthally averaged (left) and Keplerian background (right) from original FARGO3D results. Note that we do not show radial and colatitude velocity perturbations here since they are similar in both cases. With the Keplerian background subtracted, stronger  $V_{\phi} - V_{\text{Kep}}$  signals emerge as simulation time increases, attributed to the steeper pressure gradients at the gap edges at later time. Both inner and outer gap edges (gray dashed lines) exhibit perturbations with an amplitude of  $\sim$ 250 m/s (0.08  $V_{\text{p,Kep}}$ ) at 1,000

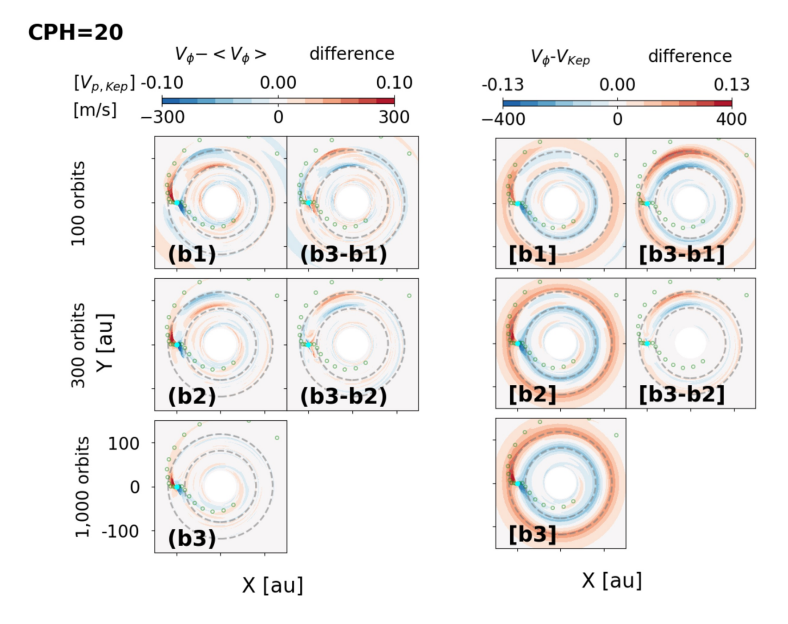


**Figure 4.15:** Comparison of  $V_{\phi}$  perturbations obtained by subtracting azimuthal average background (left) and Keplerian background (right) from original FARGO3D simulation results. Note that the colorbars are in linear scale and the ranges differ between these two groups of panels.

orbits, complicating the quantification of the contribution from spirals. Given our focus on non-axisymmetric kinematic signals, subtracting the azimuthally averaged background is more suitable.

#### 4.6.4 Channel maps

Successive channel maps (counterparts of Fig. 4.9) of our disk model at 1,000 orbits and with CPH=20 are shown in Fig. 4.16.

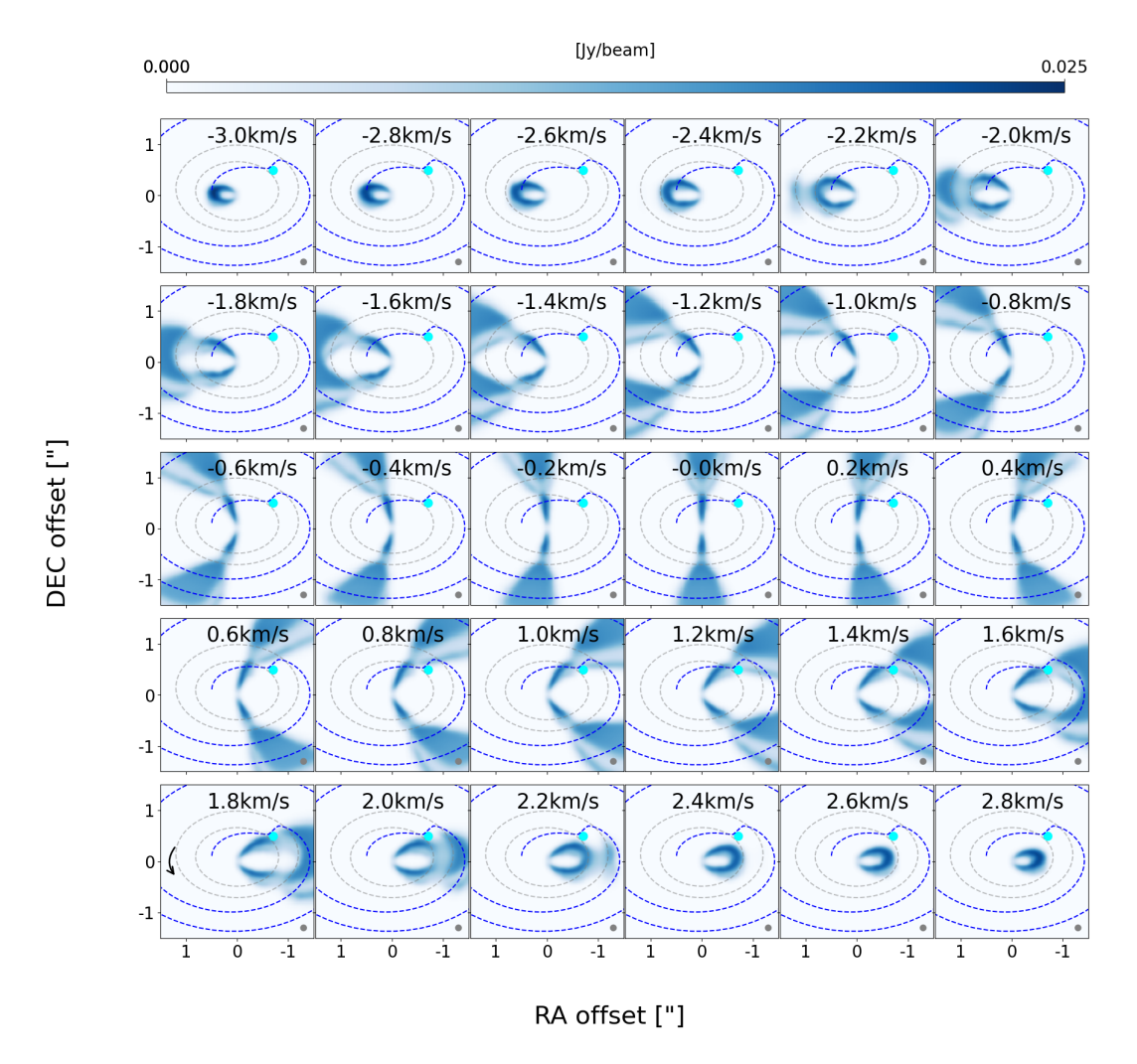


**Figure 4.16:** Successive channel maps of our disk model at 1,000 orbit and with CPH=20. Grey and blue dashed lines denote gap edges and the primary spirals, respectively. The location of the planet is indicated by the cyan marker. The disk rotation direction is marked in the lower left panel. The colorbar is in a linear scale.

## **Chapter 5**

# **Conclusions**

The research in this thesis aims to improve our understanding of planet-disk interactions and how the presents of planets can feedback on the disk thermal sturcture and leave kinematic fingerprints in the disk. Through the development of novel modelling techniques, new insights have been gained regarding the density and kinematic substructure formation and the impact of disk chemical composition.

Gaps observed in protoplanetary disks are widely interpreted as signatures of planet formation, particularly by massive planets carving structures in the disk. However, the thermal consequences of this gap-opening process have not been fully explored. In Chapter 2, we developed a novel iterative framework that couples hydrodynamical and radiative transfer simulations to study how giant planets influence the disk temperature and volatile distribution. Our results show that giant planet-induced gaps cause significant deviations in midplane temperature, leading to shifts in iceline locations and redistribution of volatiles. Compared to conventional single-pass methods, our iterative model predicts wider, deeper gaps and more pronounced thermal gradients, revealing that planet-disk interactions can strongly reshape the thermal and compositional structure of the disk.

The thermal structure of protoplanetary disks is also strongly affected by dust, which plays a key role in both radiative heating and cooling. While many models simplify the disk by focusing on the gas component alone, we incorporated multifluid dust dynamics and opacity into our iterative models to better capture the impact on disk thermal structure in Chapter 3. We find that gaps induced by forming Jo-

vian planets can change the midplane temperature by tens of Kelvin compared to smooth disks. Temperature increases in gaps can shift icelines due to volatile sublimation, while dust rings formed at pressure maxima can cool slightly and act as freeze-out zones. Multi-dust models yield shallower gaps and slightly higher temperatures than gas-only models, and we also find that varying viscosity can alter gap properties and thermal profiles, though without a simple relationship to iceline shifts.

Beyond thermal and chemical structure, planet-disk interactions can also generate distinct kinematic signatures in the gas velocity field. With recent high-resolution observations detecting deviations from Keplerian rotation, understanding the origin of these signals is crucial for identifying embedded planets. In Chapter 4, we performed 3D hydrodynamical simulations with post-processed radiative transfer to investigate these velocity perturbations. For the first time, we introduced residual velocity and channel maps—constructed by subtracting an azimuthally averaged background—as a diagnostic to highlight planet-induced motion. We showed that detecting stable kinematic patterns requires long simulation durations (on the order of 1000 planetary orbits) and high resolution (at least 14 cells per scale height) for accurate modeling, particularly in spiral regions. These benchmarks provide practical criteria for future studies of disk kinematics.

Future work can extend these studies by connecting structural and thermal disk properties to chemical observations. In particular, ALMA surveys such as The Disk Exoplanet C/Onnection (DECO) offer a promising path to test whether disk substructures influence the spatial distribution of volatiles, as predicted by our thermal models. Similarly, the kinematic features studied here can be directly applied to ALMA observational surveys like exoALMA, which aims to trace the origin of non-Keplerian gas motions and hunt forming planets within disks. Together, these efforts will help bridge the gap between simulations and observations in understanding how planets form and shape their environments.

# **Bibliography**

- Adams, F. C., Lada, C. J., & Shu, F. H. 1987, The Astrophysical Journal, 312, 788, doi: 10.1086/164924
- Alarcón, F., Bergin, E., & Teague, R. 2022, A localized kinematic structure detected in atomic carbon emission spatially coincident with a proposed protoplanet in the HD 163296 disk, arXiv. http://arxiv.org/abs/2211.16531
- Alarcón, F., Teague, R., Zhang, K., Bergin, E. A., & Barraza-Alfaro, M. 2020, The Astrophysical Journal, 905, 68, doi: 10.3847/1538-4357/abc1d6
- ALMA Partnership, Brogan, C. L., Pérez, L. M., et al. 2015, The Astrophysical Journal, 808, L3, doi: 10.1088/2041-8205/808/1/L3
- Andrews, S. M., Rosenfeld, K. A., Kraus, A. L., & Wilner, D. J. 2013, The Astrophysical Journal, 771, 129, doi: 10.1088/0004-637X/771/2/129
- Andrews, S. M., Terrell, M., Tripathi, A., et al. 2018a, The Astrophysical Journal, 865, 157, doi: 10.3847/1538-4357/aadd9f
- Andrews, S. M., Wilner, D. J., Espaillat, C., et al. 2011, The Astrophysical Journal, 732, 42, doi: 10.1088/0004-637X/732/1/42
- Andrews, S. M., Huang, J., Pérez, L. M., et al. 2018b, The Astrophysical Journal, 869, L41, doi: 10.3847/2041-8213/aaf741
- Ansdell, M., Williams, J. P., Manara, C. F., et al. 2017, The Astronomical Journal, 153, 240, doi: 10.3847/1538-3881/aa69c0

- Ansdell, M., Williams, J. P., van der Marel, N., et al. 2016, The Astrophysical Journal, 828, 46, doi: 10.3847/0004-637x/828/1/46
- Ansdell, M., Williams, J. P., Trapman, L., et al. 2018, The Astrophysical Journal, 859, 21, doi: 10.3847/1538-4357/aab890
- Auddy, S., Dey, R., Lin, M.-K., & Hall, C. 2021, arXiv:2107.09086 [astro-ph]. http://arxiv.org/abs/2107.09086
- Auddy, S., & Lin, M.-K. 2020, The Astrophysical Journal, 900, 62, doi: 10.3847/ 1538-4357/aba95d
- Bae, J. 2017, The Astrophysical Journal, 10, doi: https://doi.org/10.3847/1538-4357/aa9705
- Bae, J., Isella, A., Zhu, Z., et al. 2022, Structured Distributions of Gas and Solids in Protoplanetary Disks, arXiv. http://arxiv.org/abs/2210.13314
- Bae, J., & Zhu, Z. 2018a, The Astrophysical Journal, 859, 119, doi: 10.3847/ 1538-4357/aabf93
- —. 2018b, The Astrophysical Journal, 859, 118, doi: 10.3847/1538-4357/ aabf8c
- Bae, J., Zhu, Z., Baruteau, C., et al. 2019, The Astrophysical Journal, 884, L41, doi: 10.3847/2041-8213/ab46b0
- Bai, X.-N. 2017, The Astrophysical Journal, 845, 75, doi: 10.3847/1538-4357/aa7dda
- Balbus, S., & Hawley, J. 1991, \$\backslash\$apj, 376, 214, doi: 10.1086/170270
- Barenfeld, S. A., Carpenter, J. M., Ricci, L., & Isella, A. 2016, The Astrophysical Journal, 827, 142, doi: 10.3847/0004-637X/827/2/142
- Barenfeld, S. A., Carpenter, J. M., Sargent, A. I., Isella, A., & Ricci, L. 2017, The Astrophysical Journal, 851, 85, doi: 10.3847/1538-4357/aa989d

- Benisty, M., Bae, J., Facchini, S., et al. 2021, The Astrophysical Journal Letters, 916, L2, doi: 10.3847/2041-8213/ac0f83
- Benítez-Llambay, P., & Masset, F. S. 2016, The Astrophysical Journal Supplement Series, 223, 11, doi: 10.3847/0067-0049/223/1/11
- Bergin, E. A., Cleeves, L. I., Gorti, U., et al. 2013, Nature, 493, 644, doi: 10. 1038/nature11805
- Bi, J., van der Marel, N., Dong, R., et al. 2020, The Astrophysical Journal, 895, L18, doi: 10.3847/2041-8213/ab8eb4
- Birnstiel, T. 2023, Dust growth and evolution in protoplanetary disks, arXiv. http://arxiv.org/abs/2312.13287
- Birnstiel, T., Andrews, S. M., Pinilla, P., & Kama, M. 2015, The Astrophysical Journal, 813, L14, doi: 10.1088/2041-8205/813/1/L14
- Birnstiel, T., Dullemond, C. P., & Brauer, F. 2010, Astronomy & Astrophysics, 513, A79, doi: 10.1051/0004-6361/200913731
- Birnstiel, T., Klahr, H., & Ercolano, B. 2012, Astronomy & Astrophysics, 539, A148, doi: 10.1051/0004-6361/201118136
- Birnstiel, T., Ormel, C. W., & Dullemond, C. P. 2011, Astronomy & Astrophysics, 525, A11, doi: 10.1051/0004-6361/201015228
- Bitsch, B., Morbidelli, A., Lega, E., Kretke, K., & Crida, A. 2014, Astronomy & Astrophysics, 570, A75, doi: 10.1051/0004-6361/201424015
- Bohn, A. J., Benisty, M., Perraut, K., et al. 2021, arXiv:2112.00123 [astro-ph]. http://arxiv.org/abs/2112.00123
- Bollati, F., Lodato, G., Price, D. J., & Pinte, C. 2021, Monthly Notices of the Royal Astronomical Society, 504, 5444, doi: 10.1093/mnras/stab1145
- Booth, A. S., Tabone, B., Ilee, J. D., et al. 2021, arXiv:2109.06586 [astro-ph]. http://arxiv.org/abs/2109.06586

- Bosman, A. D., Alarcón, F., Bergin, E. A., et al. 2021, arXiv:2109.06221 [astro-ph]. http://arxiv.org/abs/2109.06221
- Brauer, F., Henning, T., & Dullemond, C. P. 2008, Astronomy & Astrophysics, 487, L1, doi: 10.1051/0004-6361:200809780
- Broome, M., Kama, M., Booth, R., & Shorttle, O. 2023, Monthly Notices of the Royal Astronomical Society, 522, 3378, doi: 10.1093/mnras/stad1159
- Cadman, J., Hall, C., Rice, K., Harries, T. J., & Klaassen, P. D. 2020, Monthly Notices of the Royal Astronomical Society, 498, 4256, doi: 10.1093/mnras/staa2596
- Calahan, J. K., Bergin, E., Zhang, K., et al. 2021, The Astrophysical Journal, 908, 8, doi: 10.3847/1538-4357/abd255
- Calcino, J., Hilder, T., Price, D. J., et al. 2022, The Astrophysical Journal Letters, 929, L25, doi: 10.3847/2041-8213/ac64a7
- Casassus, S., & Pérez, S. 2019, The Astrophysical Journal, 883, L41, doi: 10. 3847/2041-8213/ab4425
- Chen, K., & Dong, R. 2024, The Astrophysical Journal, 976, 49, doi: 10.3847/ 1538-4357/ad83d0
- Chen, K., Kama, M., Pinilla, P., & Keyte, L. 2023, Monthly Notices of the Royal Astronomical Society, 527, 2049, doi: 10.1093/mnras/stad3247
- Chen, X., & Szulágyi, J. 2021, arXiv:2112.12821 [astro-ph]. http://arxiv.org/abs/2112.12821
- Chiang, E. I., & Goldreich, P. 1997, The Astrophysical Journal, 490, 368, doi: 10. 1086/304869
- Christiaens, V., Samland, M., Henning, T., et al. 2024, Astronomy & Astrophysics, 685, L1, doi: 10.1051/0004-6361/202349089

- Clarke, C. J., Tazzari, M., Juhász, A., et al. 2018, The Astrophysical Journal, 866, L6, doi: 10.3847/2041-8213/aae36b
- Cleeves, I., Loomis, R., Teague, R., Zhang, K., & Bergin, E. 2020, 7
- Cleeves, L. I. 2016, The Astrophysical Journal, 816, L21, doi: 10.3847/ 2041-8205/816/2/L21
- Cleeves, L. I., Bergin, E. A., & Harries, T. J. 2015, The Astrophysical Journal, 807, 2, doi: 10.1088/0004-637X/807/1/2
- Cleeves, L. I., Öberg, K. I., Wilner, D. J., et al. 2018, The Astrophysical Journal, 865, 155, doi: 10.3847/1538-4357/aade96
- Collaboration, D. D., Armitage, P. J., Bae, J., et al. 2020, arXiv:2009.04345 [astro-ph]. http://arxiv.org/abs/2009.04345
- Crida, A., Morbidelli, A., & Masset, F. 2006, Icarus, 181, 587, doi: 10.1016/j.icarus.2005.10.007
- Currie, T., Lawson, K., Schneider, G., et al. 2022, Nature Astronomy, doi: 10. 1038/s41550-022-01634-x
- de Val-Borro, M., Edgar, R. G., Artymowicz, P., et al. 2006, Monthly Notices of the Royal Astronomical Society, 370, 529, doi: 10.1111/j.1365-2966. 2006.10488.x
- Dipierro, G., Lodato, G., Testi, L., & de Gregorio Monsalvo, I. 2014, Monthly Notices of the Royal Astronomical Society, 444, 1919, doi: 10.1093/mnras/stu1584
- Dipierro, G., Pinilla, P., Lodato, G., & Testi, L. 2015, Monthly Notices of the Royal Astronomical Society, 451, 974, doi: 10.1093/mnras/stv970
- Dominik, C., Min, M., & Tazaki, R. 2021, Astrophysics Source Code Library, ascl:2104.010. https://ui.adsabs.harvard.edu/abs/2021ascl.soft04010D

- Dong, R., Li, S., Chiang, E., & Li, H. 2017, The Astrophysical Journal, 843, 127, doi: 10.3847/1538-4357/aa72f2
- Dong, R., Liu, S.-Y., & Fung, J. 2019, The Astrophysical Journal, 870, 72, doi: 10. 3847/1538-4357/aaf38e
- Dong, R., Zhu, Z., & Whitney, B. 2015, The Astrophysical Journal, 809, 93, doi: 10.1088/0004-637X/809/1/93
- Drążkowska, J., & Alibert, Y. 2017, Astronomy & Astrophysics, 608, A92, doi: 10.1051/0004-6361/201731491
- Drążkowska, J., & Dullemond, C. P. 2014, Astronomy & Astrophysics, 572, A78, doi: 10.1051/0004-6361/201424809
- Duffell, P. C. 2020, The Astrophysical Journal, 889, 16, doi: 10.3847/1538-4357/ab5b0f
- Dullemond, C. P., Dominik, C., & Natta, A. 2001, The Astrophysical Journal, 560, 957, doi: 10.1086/323057
- Dullemond, C. P., Juhasz, A., Pohl, A., et al. 2012, Astrophysics Source Code Library, ascl:1202.015. https://ui.adsabs.harvard.edu/abs/2012ascl.soft02015D
- Dullemond, C. P., Birnstiel, T., Huang, J., et al. 2018, The Astrophysical Journal, 869, L46, doi: 10.3847/2041-8213/aaf742
- Facchini, S., Birnstiel, T., Bruderer, S., & van Dishoeck, E. F. 2017, Astronomy & Astrophysics, 605, A16, doi: 10.1051/0004-6361/201630329
- Facchini, S., Pinilla, P., van Dishoeck, E. F., & de Juan Ovelar, M. 2018, Astronomy & Astrophysics, 612, A104, doi: 10.1051/0004-6361/201731390
- Fang, M., Wang, L., Herczeg, G. J., et al. 2023, Nature Astronomy, doi: 10.1038/ s41550-023-02004-x

- Fedele, D., Van Dishoeck, E. F., Kama, M., Bruderer, S., & Hogerheijde, M. R. 2016, Astronomy & Astrophysics, 591, A95, doi: 10.1051/0004-6361/201526948
- Flaherty, K., Hughes, A., Teague, R., et al. 2018, The Astrophysical Journal, 856, 117, doi: 10.3847/1538-4357/aab615
- Flaherty, K., Hughes, A. M., Simon, J. B., et al. 2020, The Astrophysical Journal, 895, 109, doi: 10.3847/1538-4357/ab8cc5
- Flaherty, K. M., Hughes, A. M., Rosenfeld, K. A., et al. 2015, The Astrophysical Journal, 813, 99, doi: 10.1088/0004-637X/813/2/99
- Flaherty, K. M., Hughes, A. M., Rose, S. C., et al. 2017, The Astrophysical Journal, 843, 150, doi: 10.3847/1538-4357/aa79f9
- Flock, M., Ruge, J. P., Dzyurkevich, N., et al. 2015, Astronomy & Astrophysics, 574, A68, doi: 10.1051/0004-6361/201424693
- Fromang, S., & Nelson, R. P. 2009, Astronomy & Astrophysics, 496, 597, doi: 10. 1051/0004-6361/200811220
- Fung, J., & Chiang, E. 2016, The Astrophysical Journal, 832, 105, doi: 10.3847/0004-637X/832/2/105
- Fung, J., & Dong, R. 2015, The Astrophysical Journal, 815, L21, doi: 10.1088/ 2041-8205/815/2/L21
- Fung, J., Shi, J.-M., & Chiang, E. 2014, The Astrophysical Journal, 782, 88, doi: 10.1088/0004-637X/782/2/88
- Ginski, C., Facchini, S., Huang, J., et al. 2021, The Astrophysical Journal, 908, L25, doi: 10.3847/2041-8213/abdf57
- Goodman, J., & Rafikov, R. R. 2001, The Astrophysical Journal, 552, 793, doi: 10. 1086/320572

- Guidi, G., Tazzari, M., Testi, L., et al. 2016, Astronomy & Astrophysics, 588, A112, doi: 10.1051/0004-6361/201527516
- Haffert, S. Y., Bohn, A. J., de Boer, J., et al. 2019, Nature Astronomy, 3, 749, doi: 10.1038/s41550-019-0780-5
- Hammond, I., Christiaens, V., Price, D. J., et al. 2023, Monthly Notices of the Royal Astronomical Society: Letters, 522, L51, doi: 10.1093/mnrasl/slad027
- Hartmann, L., Calvet, N., Gullbring, E., & D'Alessio, P. 1998, The Astrophysical Journal, 495, 385, doi: 10.1086/305277
- Hashimoto, J., Muto, T., Dong, R., et al. 2020, arXiv:2009.09912 [astro-ph]. http://arxiv.org/abs/2009.09912
- Hayashi, C. 1981, Progress of Theoretical Physics Supplement, 70, 35, doi: 10. 1143/PTPS.70.35
- Hollenbach, D., Kaufman, M. J., Bergin, E. A., & Melnick, G. J. 2009, The Astrophysical Journal, 690, 1497, doi: 10.1088/0004-637X/690/2/1497
- Huang, J., Andrews, S. M., Dullemond, C. P., et al. 2018, The Astrophysical Journal, 869, L42, doi: 10.3847/2041-8213/aaf740
- Hyodo, R., Ida, S., & Charnoz, S. 2019, Astronomy & Astrophysics, 629, A90, doi: 10.1051/0004-6361/201935935
- Ilee, J. D., Walsh, C., Jennings, J., et al. 2022, arXiv:2205.01396 [astro-ph]. http://arxiv.org/abs/2205.01396
- Isella, A. 2020, Astro2020 Science White Paper Observing Planetary Systems in the Making
- Isella, A., & Turner, N. J. 2018, The Astrophysical Journal, 860, 27, doi: 10. 3847/1538-4357/aabb07
- Izquierdo, A. F., Facchini, S., Rosotti, G. P., van Dishoeck, E. F., & Testi, L. 2021a, arXiv:2111.06367 [astro-ph]. http://arxiv.org/abs/2111.06367

- Izquierdo, A. F., Testi, L., Facchini, S., Rosotti, G. P., & van Dishoeck, E. F. 2021b, arXiv:2104.09596 [astro-ph]. http://arxiv.org/abs/2104.09596
- Jang-Condell, H., & Turner, N. J. 2012, The Astrophysical Journal, 749, 153, doi: 10.1088/0004-637X/749/2/153
- —. 2013, The Astrophysical Journal, 772, 34, doi: 10.1088/0004-637X/772/
- Jennings, J., Booth, R. A., Tazzari, M., Rosotti, G. P., & Clarke, C. J. 2020, Monthly Notices of the Royal Astronomical Society, 495, 3209, doi: 10.1093/mnras/staa1365
- Ju, W., Stone, J. M., & Zhu, Z. 2016, The Astrophysical Journal, 823, 81, doi: 10. 3847/0004-637X/823/2/81
- Kama, M., Trapman, L., Fedele, D., et al. 2020, Astronomy & Astrophysics, 634, A88, doi: 10.1051/0004-6361/201937124
- Kanagawa, K. D., Muto, T., Tanaka, H., et al. 2015, The Astrophysical Journal, 806, L15, doi: 10.1088/2041-8205/806/1/L15
- —. 2016, Publications of the Astronomical Society of Japan, 68, 43, doi: 10. 1093/pasj/psw037
- Keppler, M., Benisty, M., Müller, A., et al. 2018, Astronomy & Astrophysics, 617, A44, doi: 10.1051/0004-6361/201832957
- Keppler, M., Teague, R., Bae, J., et al. 2019, Astronomy & Astrophysics, 625, A118, doi: 10.1051/0004-6361/201935034
- Keyte, L. 2024, PhD thesis
- Keyte, L., Kama, M., Booth, A. S., et al. 2023, Azimuthal C/O Variations in a Planet-Forming Disk, arXiv, doi: https://doi.org/10.48550/arXiv. 2303.08927

- Kley, W., & Dirksen, G. 2006, Astronomy & Astrophysics, 447, 369, doi: 10. 1051/0004-6361:20053914
- Krieger, A., & Wolf, S. 2022, arXiv:2203.01891 [astro-ph], doi: 10.1051/0004-6361/202142652
- Krijt, S., Bosman, A. D., Zhang, K., et al. 2020, The Astrophysical Journal, 899, 134, doi: 10.3847/1538-4357/aba75d
- Latter, H. N., & Kunz, M. W. 2022, arXiv:2201.04431 [astro-ph]. http://arxiv.org/abs/2201.04431
- Law, C. J., Loomis, R. A., Teague, R., et al. 2021, The Astrophysical Journal Supplement Series, 257, 3, doi: 10.3847/1538-4365/ac1434
- Law, C. J., Benisty, M., Facchini, S., et al. 2024, Mapping the Vertical Gas Structure of the Planet-hosting PDS 70 Disk, arXiv. http://arxiv.org/abs/2401.03018
- Leemker, M., Booth, A. S., van Dishoeck, E. F., et al. 2022, arXiv:2204.03666 [astro-ph]. http://arxiv.org/abs/2204.03666
- Lin, D. N. C., & Papaloizou, J. 1986, The Astrophysical Journal, 309, 846, doi: 10. 1086/164653
- Lin, M.-K., & Youdin, A. 2015, The Astrophysical Journal, 811, 17, doi: 10. 1088/0004-637X/811/1/17
- Long, F., Pinilla, P., Herczeg, G. J., et al. 2018, The Astrophysical Journal, 869, 17, doi: 10.3847/1538-4357/aae8e1
- Long, F., Andrews, S. M., Rosotti, G., et al. 2022, The Astrophysical Journal, 931, 6, doi: 10.3847/1538-4357/ac634e
- Longarini, C., Lodato, G., Toci, C., et al. 2021, arXiv:2108.11387 [astro-ph]. http://arxiv.org/abs/2108.11387

- Lynden-Bell, D., & Pringle, J. E. 1974, Monthly Notices of the Royal Astronomical Society, 168, 603, doi: 10.1093/mnras/168.3.603
- Madhusudhan, N., Amin, M. A., & Kennedy, G. M. 2014, The Astrophysical Journal, 794, L12, doi: 10.1088/2041-8205/794/1/L12
- Malygin, M. G., Klahr, H., Semenov, D., Henning, T., & Dullemond, C. P. 2017, Astronomy & Astrophysics, 605, A30, doi: 10.1051/0004-6361/201629933
- Manara, C. F., Ansdell, M., Rosotti, G. P., et al. 2022, arXiv:2203.09930 [astro-ph]. http://arxiv.org/abs/2203.09930
- Manara, C. F., Natta, A., Rosotti, G. P., et al. 2020, Astronomy & Astrophysics, 639, A58, doi: 10.1051/0004-6361/202037949
- Martin, R. G., Lepp, S., Lubow, S. H., et al. 2022, arXiv:2202.06878 [astro-ph]. http://arxiv.org/abs/2202.06878
- Masset, F. 2002, \$\backslash\$aap, 387, 605, doi: 10.1051/0004-6361: 20020240
- Mathis, J. S., Rumpl, W., & Nordsieck, K. H. 1977, The Astrophysical Journal, 217, 425, doi: 10.1086/155591
- Mayor, M., & Queloz, D. 1995, Nature, 378, 355, doi: 10.1038/378355a0
- Miotello, A., Kamp, I., Birnstiel, T., Cleeves, L. I., & Kataoka, A. 2022, arXiv:2203.09818 [astro-ph]. http://arxiv.org/abs/2203.09818
- Miotello, A., Facchini, S., Van Dishoeck, E. F., et al. 2019, Astronomy & Astrophysics, 631, A69, doi: 10.1051/0004-6361/201935441
- Miranda, R., & Rafikov, R. R. 2019, The Astrophysical Journal, 878, L9, doi: 10. 3847/2041-8213/ab22a7
- —. 2020, The Astrophysical Journal, 892, 65, doi: 10.3847/1538-4357/ ab791a

- Morfill, G., & Voelk, H. 1984, \$\backslash\$apj, 287, 371, doi: 10.1086/162697
- Muley, D., Dong, R., & Fung, J. 2021, arXiv:2107.06323 [astro-ph]. http://arxiv.org/abs/2107.06323
- Müller, A., Keppler, M., Henning, T., et al. 2018, Astronomy & Astrophysics, 617, L2, doi: 10.1051/0004-6361/201833584
- Nelson, R. P., Gressel, O., & Umurhan, O. M. 2013, Monthly Notices of the Royal Astronomical Society, 435, 2610, doi: 10.1093/mnras/stt1475
- Norfolk, B. J., Pinte, C., Calcino, J., et al. 2022, The Origin of the Doppler-flip in HD 100546: a large scale spiral arm generated by an inner binary companion, arXiv. http://arxiv.org/abs/2208.02542
- Ohashi, N., Tobin, J. J., Jørgensen, J. K., et al. 2023, Early Planet Formation in Embedded Disks (eDisk). I. Overview of the Program and First Results, arXiv. http://arxiv.org/abs/2306.15406
- Oka, A., Nakamoto, T., & Ida, S. 2011, The Astronomical Journal, 738, 141, doi: 10.1088/0004-637X/738/2/141
- Owen, J. E. 2020, Monthly Notices of the Royal Astronomical Society, 495, 3160, doi: 10.1093/mnras/staa1309
- Pascucci, I., Testi, L., Herczeg, G. J., et al. 2016, The Astrophysical Journal, 831, 125, doi: 10.3847/0004-637X/831/2/125
- Perez, S., Casassus, S., & Benítez-Llambay, P. 2018, Monthly Notices of the Royal Astronomical Society: Letters, 480, L12, doi: 10.1093/mnrasl/sly109
- Perez, S., Dunhill, A., Casassus, S., et al. 2015, The Astrophysical Journal, 811, L5, doi: 10.1088/2041-8205/811/1/L5
- Pfeil, T., & Klahr, H. 2019, The Astrophysical Journal, 871, 150, doi: 10.3847/ 1538-4357/aaf962

- Pineda, J. E., Segura-Cox, D., Caselli, P., et al. 2020, Nature Astronomy, 4, 1158, doi: 10.1038/s41550-020-1150-z
- Pineda, J. E., Arzoumanian, D., André, P., et al. 2023, From Bubbles and Filaments to Cores and Disks: Gas Gathering and Growth of Structure Leading to the Formation of Stellar Systems, arXiv, doi: 10.48550/arXiv.2205.03935
- Pinilla, P., Benisty, M., & Birnstiel, T. 2012a, Astronomy & Astrophysics, 545, A81, doi: 10.1051/0004-6361/201219315
- Pinilla, P., Birnstiel, T., Ricci, L., et al. 2012b, Astronomy & Astrophysics, 538, A114, doi: 10.1051/0004-6361/201118204
- Pinilla, P., Pohl, A., Stammler, S. M., & Birnstiel, T. 2017, The Astrophysical Journal, 845, 68, doi: 10.3847/1538-4357/aa7edb
- Pinte, C., Dent, W. R. F., Ménard, F., et al. 2016, The Astrophysical Journal, 816, 25, doi: 10.3847/0004-637X/816/1/25
- Pinte, C., Teague, R., Flaherty, K., et al. 2022, arXiv:2203.09528 [astro-ph]. http://arxiv.org/abs/2203.09528
- Pinte, C., Price, D. J., Ménard, F., et al. 2018, The Astrophysical Journal, 860, L13, doi: 10.3847/2041-8213/aac6dc
- Pinte, C., van der Plas, G., Ménard, F., et al. 2019, Nature Astronomy, 3, 1109, doi: 10.1038/s41550-019-0852-6
- Pinte, C., Price, D. J., Ménard, F., et al. 2020, The Astrophysical Journal, 890, L9, doi: 10.3847/2041-8213/ab6dda
- Pinte, C., Hammond, I., Price, D. J., et al. 2023, Kinematic and thermal signatures of the directly imaged protoplanet candidate around Elias 2-24, arXiv. http://arxiv.org/abs/2301.08759
- Piso, A.-M. A., Öberg, K. I., Birnstiel, T., & Murray-Clay, R. A. 2015, The Astronomical Journal, 815, 109, doi: 10.1088/0004-637X/815/2/109

- Portilla-Revelo, B., Kamp, I., Rab, C., et al. 2021, arXiv:2111.08648 [astro-ph]. http://arxiv.org/abs/2111.08648
- Pyerin, M. A., Delage, T. N., Kurtovic, N. T., et al. 2021, arXiv:2110.03373 [astro-ph]. http://arxiv.org/abs/2110.03373
- Qi, C., Öberg, K. I., Wilner, D. J., et al. 2013, Science, 341, 630, doi: 10.1126/science.1239560
- Rabago, I., & Zhu, Z. 2021, Monthly Notices of the Royal Astronomical Society, 502, 5325, doi: 10.1093/mnras/stab447
- Rafikov, R. R. 2002, The Astrophysical Journal, 569, 997, doi: 10.1086/339399
- Ros, K., & Johansen, A. 2013, Astronomy & Astrophysics, 552, A137, doi: 10. 1051/0004-6361/201220536
- Rosotti, G. P., Juhasz, A., Booth, R. A., & Clarke, C. J. 2016, Monthly Notices of the Royal Astronomical Society, 459, 2790, doi: 10.1093/mnras/stw691
- Rowther, S., Nealon, R., & Meru, F. 2021, arXiv:2110.06227 [astro-ph]. http://arxiv.org/abs/2110.06227
- Savvidou, S., Bitsch, B., & Lambrechts, M. 2020, Astronomy & Astrophysics, 640, A63, doi: 10.1051/0004-6361/201936576
- Schoonenberg, D., & Ormel, C. W. 2017, Astronomy & Astrophysics, 602, A21, doi: 10.1051/0004-6361/201630013
- Schwarz, K. R., Bergin, E. A., Cleeves, L. I., et al. 2018, The Astrophysical Journal, 856, 85, doi: 10.3847/1538-4357/aaae08
- —. 2019, The Astrophysical Journal, 877, 131, doi: 10.3847/1538-4357/ ab1c5e
- Shakura, N. I., & Sunyaev, R. A. 1973, Astronomy and Astrophysics, 24, 337. https://ui.adsabs.harvard.edu/abs/1973A&A....24..337S

- Siebenmorgen, R., & Heymann, F. 2012, Astronomy & Astrophysics, 539, A20, doi: 10.1051/0004-6361/201118493
- Speedie, J., Booth, R. A., & Dong, R. 2022, The Astrophysical Journal, 930, 40, doi: 10.3847/1538-4357/ac5cc0
- Speedie, J., & Dong, R. 2022, The Astrophysical Journal Letters, 940, L43, doi: 10.3847/2041-8213/aca074
- Speedie, J., Dong, R., Hall, C., et al. 2024, Nature, 633, 58, doi: 10.1038/s41586-024-07877-0
- Speedie, J., Dong, R., Teague, R., et al. 2025, The Astrophysical Journal Letters, 981, L30, doi: 10.3847/2041-8213/adb7d5
- Stevenson, D. J., & Lunine, J. I. 1988, Icarus, 75, 146, doi: 10.1016/0019-1035(88)90133-9
- Tabone, B., Rosotti, G. P., Cridland, A. J., Armitage, P. J., & Lodato, G. 2021a, arXiv:2111.10145 [astro-ph]. http://arxiv.org/abs/2111.10145
- Tabone, B., Rosotti, G. P., Lodato, G., et al. 2021b, arXiv:2111.14473 [astro-ph]. http://arxiv.org/abs/2111.14473
- Takahashi, S., & Inutsuka, S.-i. 2014, The Astrophysical Journal, 794, 55, doi: 10. 1088/0004-637X/794/1/55
- Takasao, S., Aoyama, Y., & Ikoma, M. 2021, arXiv:2106.16113 [astro-ph]. http://arxiv.org/abs/2106.16113
- Takeuchi, T., & Lin, D. 2002, \$\backslash\$api, 581, 1344, doi: 10.1086/344437
- Tazaki, R., Murakawa, K., Muto, T., Honda, M., & Inoue, A. K. 2021, arXiv:2108.08637 [astro-ph]. http://arxiv.org/abs/2108.08637
- Tazzari, M., Clarke, C. J., Testi, L., et al. 2021, Monthly Notices of the Royal Astronomical Society, 506, 2804, doi: 10.1093/mnras/stab1808

- Teague, R. 2019, Journal of Open Source Software, 4, 1220, doi: 10.21105/joss.01220
- Teague, R., Bae, J., Benisty, M., et al. 2022a, arXiv:2204.06691 [astro-ph]. http://arxiv.org/abs/2204.06691
- Teague, R., Bae, J., & Bergin, E. A. 2019a, Nature, 574, 378, doi: 10.1038/s41586-019-1642-0
- Teague, R., Bae, J., Bergin, E. A., Birnstiel, T., & Foreman-Mackey, D. 2018a, The Astrophysical Journal, 860, L12, doi: 10.3847/2041-8213/aac6d7
- Teague, R., Bae, J., Huang, J., & Bergin, E. A. 2019b, The Astrophysical Journal, 884, L56, doi: 10.3847/2041-8213/ab4a83
- Teague, R., Henning, T., Guilloteau, S., et al. 2018b, The Astrophysical Journal, 864, 133, doi: 10.3847/1538-4357/aad80e
- Teague, R., Bae, J., Andrews, S. M., et al. 2022b, Mapping the Complex Kinematic Substructure in the TW Hya Disk, arXiv. http://arxiv.org/abs/2208.04837
- Teague, R., Benisty, M., Facchini, S., et al. 2025, exoALMA I. Science Goals, Project Design and Data Products, arXiv, doi: 10.48550/arXiv.2504. 18688
- Terry, J., Hall, C., Abreau, S., & Gleyzer, S. 2022, Locating Hidden Exoplanets in ALMA Data Using Machine Learning, arXiv. http://arxiv.org/abs/2211.09541
- Terry, J. P., Hall, C., Longarini, C., et al. 2021, arXiv:2108.11282 [astro-ph]. http://arxiv.org/abs/2108.11282
- Toomre, A. 1964, \$\backslash\$apj, 139, 1217, doi: 10.1086/147861
- Trapman, L., Tabone, B., Rosotti, G., & Zhang, K. 2021, arXiv:2112.00645 [astro-ph]. http://arxiv.org/abs/2112.00645

- Trapman, L., Zhang, K., Hoff, M. R. L. v. t., Hogerheijde, M. R., & Bergin, E. A. 2022, arXiv:2201.09900 [astro-ph]. http://arxiv.org/abs/2201.09900
- Turner, N. J., Choukroun, M., Castillo-Rogez, J., & Bryden, G. 2012, The Astrophysical Journal, 748, 92, doi: 10.1088/0004-637X/748/2/92
- Turrini, D., Schisano, E., Fonte, S., et al. 2021, The Astrophysical Journal, 909, 40, doi: 10.3847/1538-4357/abd6e5
- Van Der Marel, N., Dong, R., Di Francesco, J., Williams, J. P., & Tobin, J. 2019, The Astrophysical Journal, 872, 112, doi: 10.3847/1538-4357/aafd31
- van der Marel, N., van Dishoeck, E., Bruderer, S., et al. 2013, Science, 340, 1199, doi: 10.1126/science.1236770
- van 't Hoff, M. L. R., Persson, M. V., Harsono, D., et al. 2018, Astronomy & Astrophysics, 613, A29, doi: 10.1051/0004-6361/201731656
- van 't Hoff, M. L. R., Walsh, C., Kama, M., Facchini, S., & van Dishoeck, E. F. 2017, Astronomy & Astrophysics, 599, A101, doi: 10.1051/0004-6361/201629452
- Veronesi, B., Paneque-Carreno, T., Lodato, G., et al. 2021, arXiv:2104.09530 [astro-ph]. http://arxiv.org/abs/2104.09530
- Verrios, H. J., Price, D. J., Pinte, C., Hilder, T., & Calcino, J. 2022, doi: https://doi.org/10.48550/arXiv.2207.02869
- Villenave, M., Stapelfeldt, K. R., Duchene, G., et al. 2022, arXiv:2204.00640 [astro-ph]. http://arxiv.org/abs/2204.00640
- Vorobyov, E., Skliarevskii, A. M., Molyarova, T., et al. 2021, arXiv:2112.06004 [astro-ph]. http://arxiv.org/abs/2112.06004
- Wang, J. J., Vigan, A., Lacour, S., et al. 2021, The Astronomical Journal, 161, 148, doi: 10.3847/1538-3881/abdb2d

- Weber, P., Pérez, S., Benítez-Llambay, P., et al. 2019, The Astrophysical Journal, 884, 178, doi: 10.3847/1538-4357/ab412f
- Weidenschilling, S. J. 1977, Monthly Notices of the Royal Astronomical Society, 180, 57, doi: 10.1093/mnras/180.2.57
- Whipple, F. 1972, in From Plasma to Planet, ed. A. Elvius, 211
- Wu, Y.-L., Bowler, B. P., Sheehan, P. D., et al. 2022, arXiv:2204.06013 [astro-ph]. http://arxiv.org/abs/2204.06013
- Youdin, A. N. A., & Lithwick, Y. 2007, Icarus, 192, 588, doi: 10.1016/j.icarus.2007.07.012
- Yu, H., Teague, R., Bae, J., & Öberg, K. 2021, arXiv:2109.10822 [astro-ph]. http://arxiv.org/abs/2109.10822
- Zhang, K., Bergin, E. A., Blake, G. A., Cleeves, L. I., & Schwarz, K. R. 2017, Nature Astronomy, 1, 0130, doi: 10.1038/s41550-017-0130
- Zhang, K., Bergin, E. A., Schwarz, K., Krijt, S., & Ciesla, F. 2019, The Astrophysical Journal, 883, 98, doi: 10.3847/1538-4357/ab38b9
- Zhang, K., Blake, G. A., & Bergin, E. A. 2015, The Astrophysical Journal, 806, L7, doi: 10.1088/2041-8205/806/1/L7
- Zhang, M., Huang, P., & Dong, R. 2023, The dependence of the structure of planet-opened gaps in protoplanetary disks on radiative cooling, arXiv. http://arxiv.org/abs/2310.11757
- Zhang, S., Hu, X., Zhu, Z., & Bae, J. 2021a, arXiv:2110.00858 [astro-ph]. http://arxiv.org/abs/2110.00858
- Zhang, S., & Zhu, Z. 2020, Monthly Notices of the Royal Astronomical Society, 493, 2287, doi: 10.1093/mnras/staa404
- Zhang, S., Zhu, Z., & Kang, M. 2021b, arXiv:2111.15196 [astro-ph]. http://arxiv.org/abs/2111.15196

- Zhang, S., Zhu, Z., Huang, J., et al. 2018, The Astrophysical Journal, 869, L47, doi: 10.3847/2041-8213/aaf744
- Zhou, Y., Bowler, B. P., Wagner, K. R., et al. 2021, The Astronomical Journal, 161, 244, doi: 10.3847/1538-3881/abeb7a
- Zhou, Y., Bowler, B. P., Sanghi, A., et al. 2025, The Astrophysical Journal Letters, 980, L39, doi: 10.3847/2041-8213/adb134
- Zhu, Z., Stone, J. M., Rafikov, R. R., & Bai, X.-n. 2014, The Astrophysical Journal, 785, 122, doi: 10.1088/0004-637X/785/2/122
- Zhu, Z., & Zhang, R. M. 2021, arXiv:2112.03311 [astro-ph]. http://arxiv.org/abs/2112.03311
- Öberg, K. I., Murray-Clay, R., & Bergin, E. A. 2011, The Astrophysical Journal, 743, L16, doi: 10.1088/2041-8205/743/1/L16
- Öberg, K. I., Guzmán, V. V., Walsh, C., et al. 2021, The Astrophysical Journal Supplement Series, 257, 1, doi: 10.3847/1538-4365/ac1432